Supplementary Information

Multi-Cavity Discrete Coordination Cages Encapsulating up to Four Units of Pyrazine-*N,N'*-dioxide: Molecular Soybeans

Trilochan Dakua, Srabani Srotoswini Mishra, Ashish Kumar, Shobhana Krishnaswamy and Dillip Kumar Chand*

IoE Center of Molecular Architecture Department of Chemistry, Indian Institute of Technology Madras, Chennai 600036, India.

E-mail: dillip@zmail.iitm.ac.in

Table of Contents

S1. Materials and methods

The metal salts and fine chemicals like $PdCl_2$, $Pd(NO_3)_2 \cdot 2H_2O$, $AgNO_3$, 1-Ethyl-3-(3-dimethylaminopropyl)carbodiimide hydrochloride (EDC·HCl) and 1,3-diaminobenzene were acquired from Sigma Aldrich. Fine chemicals like pyridine-3,5-dicarboxylic acid, nicotinic acid, DMAP, and all common reagents were obtained from Spectrochem, India and were used as received without further purification. The deuterated solvents were obtained from Sigma Aldrich, Cambridge Isotope laboratories and SYNMR, India. Solution state ^{1}H and ^{13}C NMR spectral data were obtained using either a Bruker 400 MHz or a 500 MHz FT NMR spectrometer. The ESI-MS spectra were recorded on an Agilent Q-TOF instrument. The single crystal X-ray diffraction analysis was carried out using a Bruker D8 VENTURE instrument.

The symmetrical ligands **L2** – **L4** are new and these are prepared in this work. The precursors required for the synthesis of ligands i.e. *N*-(3-aminophenyl)nicotinamide, **A** and 5-(ethoxycarbonyl)nicotinic acid, **B** were synthesized following reported procedures.[1-2]

S2. Synthesis and characterisation of ligands

Synthesis of Ligand L2

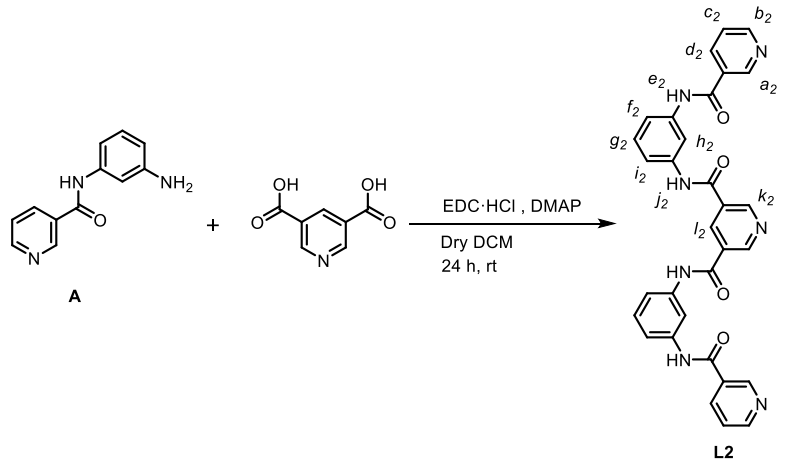

Scheme S1. Synthetic route followed for the synthesis of ligand **L2**.

To a suspension of pyridine-3,5-dicarboxylic acid (170 mg, 1.02 mmol) in 20 ml dry DCM maintained at 0-5 °C, *N*-(3-aminophenyl)nicotinamide (**A**) [1] (434 mg, 2.04 mmol), DMAP (62 mg, 0.51 mmol) were added followed by addition of EDC·HCl (584 mg, 3.06 mmol) under nitrogen atmosphere. The reaction mixture was stirred for 24 h under nitrogen atmosphere. Solvents were evaporated and the crude material was washed with water several times to yield the pure compound **L2** as a light brown solid after evaporation of the solvent and drying under vacuum (Yield: 369 mg, 72%).

^{1}H NMR (500 MHz, DMSO-d_6, 298 K): δ (ppm) 10.69 (s, 2H, H_{j2}), 10.55 (s, 2H, H_{e2}), 9.28 (d, 2H, J = 2.1 Hz, H_{k2}), 9.12 (s, 2H, J = 1.8 Hz, H_{a2}), 8.85 (t, 1H, J = 2.2 Hz, H_{l2}), 8.76 (d, 2H, J = 1.5 Hz, J = 4.8 Hz, H_{b2}), 8.38 (t, 2H, J = 1.9 Hz, H_{h2}), 8.31 (dd, 2H, J = 7.9 Hz, J = 1.8 Hz, H_{d2}), 7.58 (m, 2H, H_{c2}), 7.55 (m, 2H, H_{i2}), 7.54 (m, 2H, H_{f2}), 7.38 (t, 1H, J = 7.9 Hz, H_{g2}).

^{13}C NMR (125 MHz, DMSO-d_6, 298 K): δ (ppm) 164.18, 163.58, 152.13, 151.09, 148.74, 139.19, 139.03, 135.53, 134.81, 130.62, 130.26, 128.91, 123.52, 116.40, 116.26, 112.74.

ESI-MS (*m/z*): calculated for [**L2**+H]$^{+}$, 558.1889. Observed, 558.1827.

Synthesis of Ligand L3

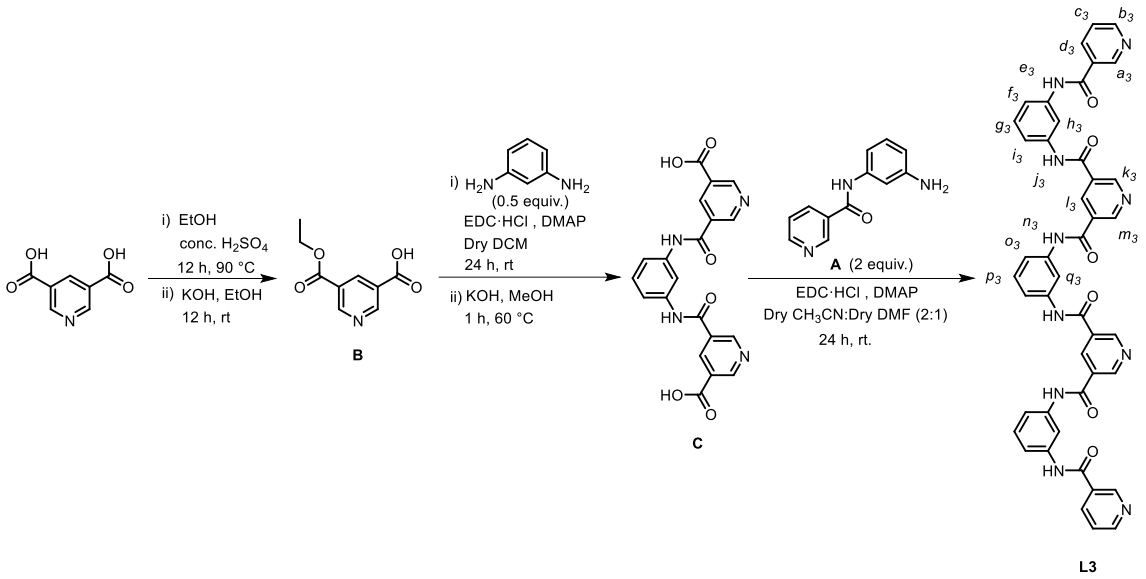

Scheme S2. Synthetic route followed for the synthesis of ligand **L3**.

5,5'-((1,3-phenylenebis(azanediyl))bis(carbonyl))dinicotinic acid (**C**):

5-(ethoxycarbonyl)nicotinic acid (**B**) was synthesized by reported procedure which was condensed with *m*-phenylene diamine.[2]

To a suspension of 5-(ethoxycarbonyl)nicotinic acid (**B**) (500 mg, 2.56 mmol) in 40 ml dry DCM maintained at 0-5 °C, *m*-phenylene diamine (125 mg, 1.28 mmol), DMAP (78 mg, 0.64 mmol) were added followed by addition of EDC·HCl (491 mg, 2.56 mmol) under nitrogen atmosphere. The reaction mixture was stirred for 24 h under nitrogen atmosphere. To the filtrate, saturated $NaHCO_3$ solution was added slowly to neutralize the excess acid until the evolution of CO_2 ceased. The organic layer was washed with distilled water, separated and dried over anhydrous Na_2SO_4. The product was purified by flash column chromatography (2.5 % MeOH/DCM). To this compound (520 mg, 0.54 mmol) suspended in methanol, anhydrous KOH (152 mg, 2.7 mmol) was added. The reaction was refluxed at 60 °C for 1 h. To this reaction mixture, 50 ml of water was added and work up was done with DCM solvent. To the aqueous layer, supersaturated oxalic acid was added dropwise maintaining the pH~3. The precipitate formed was filtered out and dried in vacuo. The compound **C** was obtained as orange solid powder (yield: 220 mg, 93%).

^{1}H NMR (400 MHz, DMSO-d_6, 298 K): δ (ppm) 10.71 (s, 2H, H_d), 9.31 (s, 2H, H_a), 9.23 (s, 2H, H_c), 8.79 (s, 2H, H_b), 8.38 (s, 1H, H_g), 7.55 (d, 2H, J = 8.0 Hz, H_e), 7.38 (t, 1H, J = 8.0 Hz, H_f).

^{13}C NMR (125 MHz, DMSO-d_6, 298 K): δ (ppm) 165.90, 163.34, 152.49, 151.31, 139.04, 136.11, 130.47, 128.93, 134.81, 126.67, 116.57, 113.00.

HRMS (*m/z*): Calculated for $[M+H]^+$ 407.0991, found 407.0990.

N^3, $N^{3'}$-(1,3-phenylene)bis(N^5-(3-(nicotinamido)phenyl)pyridine-3,5-dicarboxamide) (**L3**):

To a suspension of 5,5'-((1,3-phenylenebis(azanediyl))bis(carbonyl))dinicotinic acid (**C**) (250 mg, 0.61 mmol) in 5 ml dry CH_3CN and 5 ml of dry DMF, *N*-(3-aminophenyl)nicotinamide (**A**) (289 mg, 1.35 mmol), DMAP (38 mg, 0.30 mmol) were added followed by addition of EDC·HCl (260 mg, 1.35 mmol) under nitrogen atmosphere. The reaction mixture was stirred for 24 h under nitrogen atmosphere. The precipitate formed was centrifuged and washed with saturated $NaHCO_3$ solution. It was dried in vacuo to obtain the dark green coloured product (266 mg, 54% yield).

^{1}H NMR (500 MHz, DMSO-d_6, 298 K): δ (ppm) 10.74 (s, 2H, H_{j3}), 10.72 (s, 2H, H_{n3}), 10.55 (s, 2H, H_{e3}), 9.28 (s, 4H, H_{k3}, H_{m3}), 9.12 (s, 2H, H_{a3}), 8.86 (s, 2H, H_{l3}), 8.76 (s, 2H, H_{b3}), 8.42 (s, 1H, H_{q3}), 8.38 (s, 2H, H_{i3}), 8.32 (d, 2H, J = 7.31 Hz, H_{d3}), 7.54 (m, 8H, H_{f3}, H_{h3}, H_{o3}, H_{c3}), 7.38 (m, 3H, H_{g3}, H_{p3}).

^{13}C NMR (125 MHz, DMSO-d_6, 298 K): δ (ppm) 164.17, 163.61, 163.57, 152.12, 151.11, 148.74, 139.19, 139.09, 139.03, 135.52, 134.80, 130.61, 130.25, 128.97, 128.89, 125.50, 116.38, 116.24, 112.73.

HRMS (*m/z*): Calculated for [**L3**+Na]$^+$, 819.2404. Observed, 819.2139.

Synthesis of Ligand L4

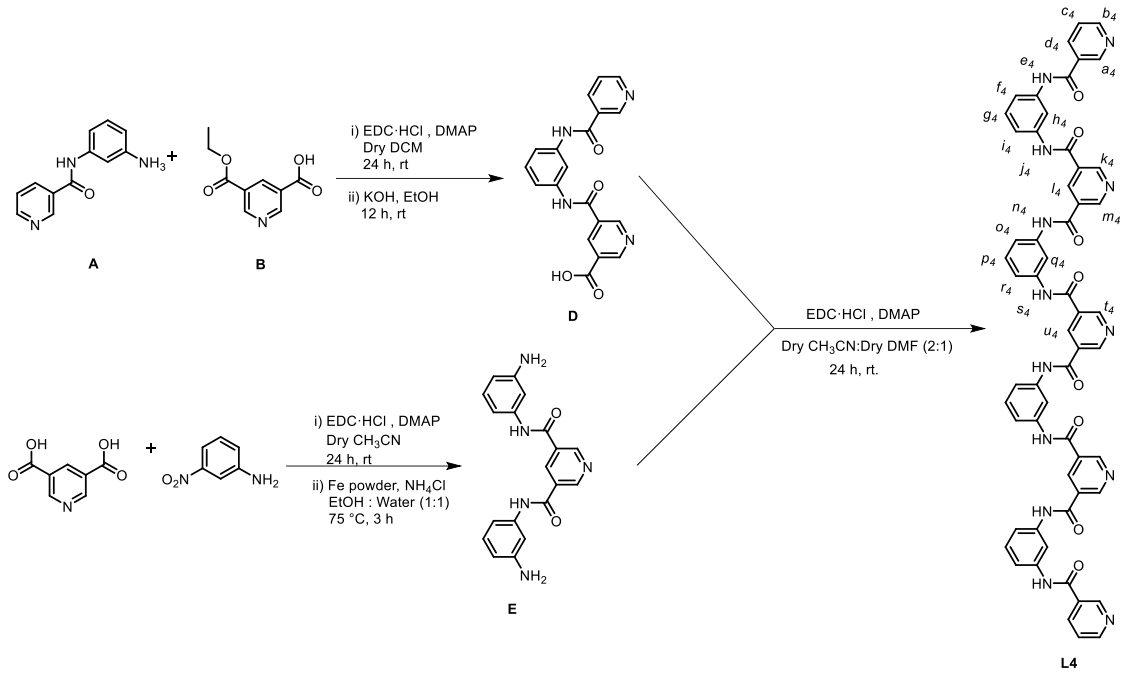

Scheme S3. Synthetic route followed for the synthesis of ligand **L4**.

5-((3-(nicotinamido)phenyl)carbamoyl)nicotinic acid (**D**):

To a suspension of *N*-(3-aminophenyl)nicotinamide (**A**) (500 mg, 2.34 mmol) in 40 ml dry DCM, 5-(ethoxycarbonyl)nicotinic acid (**B**) (503 mg, 2.58 mmol), DMAP (144 mg, 1.17 mmol) were added followed by addition of EDC·HCl (648 mg, 2.58 mmol) under nitrogen atmosphere. The reaction mixture was stirred for 24 h under nitrogen atmosphere. To the filtrate, saturated $NaHCO_3$ solution was added slowly to neutralize the excess acid until the evolution of CO_2 ceased. The organic layer was washed with distilled water, separated and dried over anhydrous Na_2SO_4. The product was purified by flash column chromatography (60 % EtOAc/Hexane). To this compound (500 mg, 1.28 mmol) suspended in methanol, anhydrous KOH (360 mg, 6.40 mmol) was added. The reaction was refluxed at 60 °C for 1 h. To this reaction mixture, 50 ml of water was added and work up was done with DCM solvent. To the aqueous layer, supersaturated oxalic acid was added dropwise maintaining the pH~3. The precipitate formed was filtered out and dried in vacuo. The compound **D** was obtained as orange solid powder (yield: 417 mg, 90%).

^{1}H NMR (500 MHz, DMSO-*d*$_6$, 298 K): δ (ppm) 10.69 (s, 1H, H_i), 10.55 (s, 1H, H_d), 9.28 (s, 1H, H_a), 9.21 (s, 1H, H_j), 9.11 (s, 1H, H_c), 8.78 (s, 1H, H_b), 8.76 (t, 1H, H_m), 8.35 (s, 1H, H_g), 8.31 (d, 1H, *J* = 7.3 Hz, H_k), 7.56 (s, 1H, H_l), 7.54(s, 1H, H_e), 7.52 (s, 1H, H_h), 7.35 (m, 1H, H_f).

^{13}C NMR (125 MHz, DMSO-d_6, 298 K): δ (ppm) 165.90, 163.34, 152.49, 151.31, 139.04, 136.11, 130.47, 128.93, 134.81, 126.67, 116.57, 113.00.

HRMS (*m/z*): Calculated for $[M+H]^+$ 363.1093, found 363.1089.

N^3, N^5-bis(3-aminophenyl)pyridine-3,5-dicarboxamide (**E**):

To a suspension of pyridine-3,5-dicarboxylic acid (1 g, 5.98 mmol) in 40 ml dry CH_3CN, 3-nitroaniline (1.60 g, 12.99 mmol), DMAP (366 mg, 2.99 mmol) were added followed by addition of EDC·HCl (2.29 g, 11.96 mmol) under nitrogen atmosphere. The reaction mixture was stirred for 24 h under nitrogen atmosphere. The reaction mixture was washed with saturated $NaHCO_3$ solution. The precipitate formed was filtered and dried under vacuo. To this product (500 mg, 1.23 mmol) suspended in 20 ml of EtOH and 10 ml of H_2O, iron powder (344 mg, 6.15 mmol) and NH_4Cl (329 mg, 6.15 mmol) were added. The reaction was refluxed at 80 °C for 3 h. The solvent was evaporated and the product was purified by column chromatography (60 % EtOAc/Hexane). The product **E** was obtained as a brown solid powder (yield: 396 mg, 92%) after drying from vacuo.

^{1}H NMR (500 MHz, DMSO-d_6, 298 K): δ (ppm) 10.30 (s, 2H, H_f), 9.20 (s, 2H, H_g), 8.75 (s, 2H, H_h), 7.12 (s, 2H, H_e), 7.00 (m, 2H, H_d), 6.91 (d, 2H, H_b), 6.36 (s, 1H, H_c), 5.19 (bs, 4H, H_a).

^{13}C NMR (125 MHz, DMSO-d_6, 298 K): δ (ppm) 163.25, 150.79, 148.93, 139.33, 134.56, 130.47, 128.95, 110.25, 108.37, 106.08.

HRMS (*m/z*): Calculated for $[M+H]^+$ 348.1460 , found 348.1485.

N^3,$N^{3'}$-(((pyridine-3,5-dicarbonyl)bis(azanediyl))bis(3,1-phenylene))bis(N5-(3-(nicotinamido)phenyl)pyridine-3,5-dicarboxamide) (**L4**):

To a suspension of 5-((3-(nicotinamido)phenyl)carbamoyl)nicotinic acid (**D**) (521 mg, 1.43 mmol) in 5 ml dry CH_3CN and 5 ml of dry DMF, N^3, N^5-bis(3-aminophenyl)pyridine-3,5-dicarboxamide (**E**) (250 mg, 0.71 mmol), DMAP (44 mg, 0.35 mmol) were added followed by addition of EDC·HCl (276 mg, 1.43 mmol) under nitrogen atmosphere. The reaction mixture was stirred for 24 h under nitrogen atmosphere. The precipitate formed was centrifuged and washed with saturated $NaHCO_3$ solution. It was dried in vacuo to obtain the dark green coloured product (375 mg, 51% yield).

^{1}H NMR (500 MHz, DMSO-d_6, 298 K): δ (ppm) 10.68 (m, 8H, H_{j4}, H_{n4}, H_4), 10.52 (s, 6H, H_{e4}), 9.28 (s, 6H, H_{k4}, H_{m4}, H_{t4}), 9.12 (s, 2H, H_{a4}), 8.84 (s, 4H, H_{l4}, H_{u4}), 8.76 (d, 2H, H_{b4}), 8.41 (s, 2H, H_{h4}), 8.37 (s, 2H, H_{q4}), 8.31 (d, 2H, J = 7.72 Hz, H_{d4}), 7.53 (m, 10H, H_{c4}, H_{f4}, H_{i4}, H_{o4}, H_{r4}), 7.38 (m, 4H, H_{g4}, H_{p4}).

^{13}C NMR (125 MHz, DMSO-d_6, 298 K): δ (ppm) 164.15, 163.59, 163.55, 152.11, 151.10, 148.73, 139.18, 139.08, 139.02, 135.51, 134.80, 130.60, 130.24, 128.96, 128.88, 125.48, 116.36, 116.21, 112.69.

HRMS (*m/z*): Calculated for [**L3**+H]$^+$, 1036.3279. Observed, 1036.3285.

Characterisation of Ligands

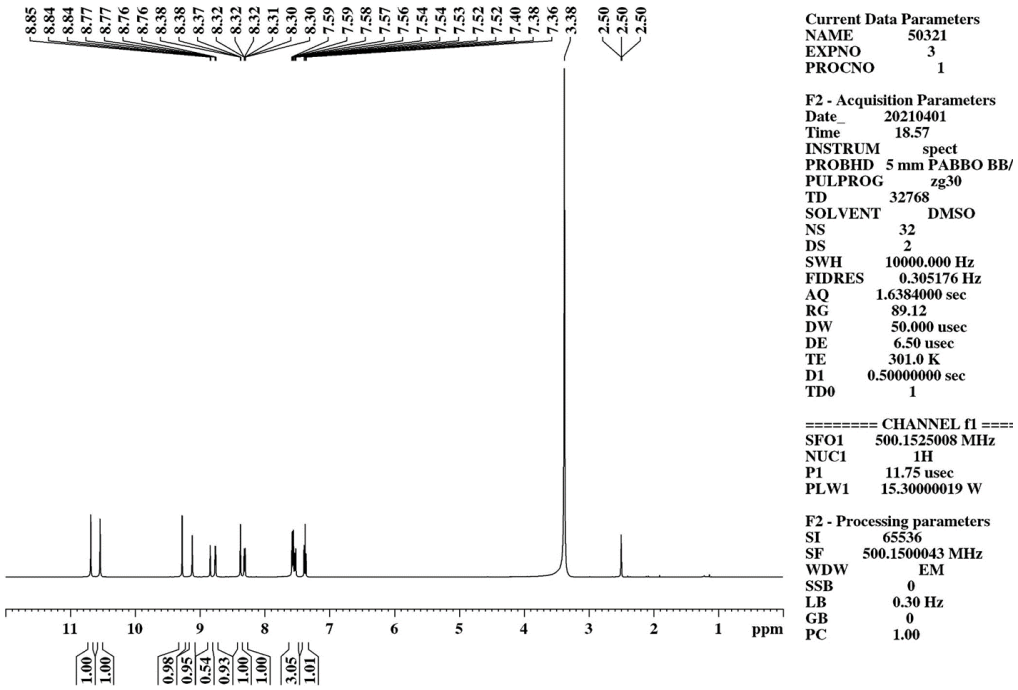

Figure S1. ^{1}H NMR spectrum (500 MHz, DMSO-d_6, 298 K) of ligand **L2**.

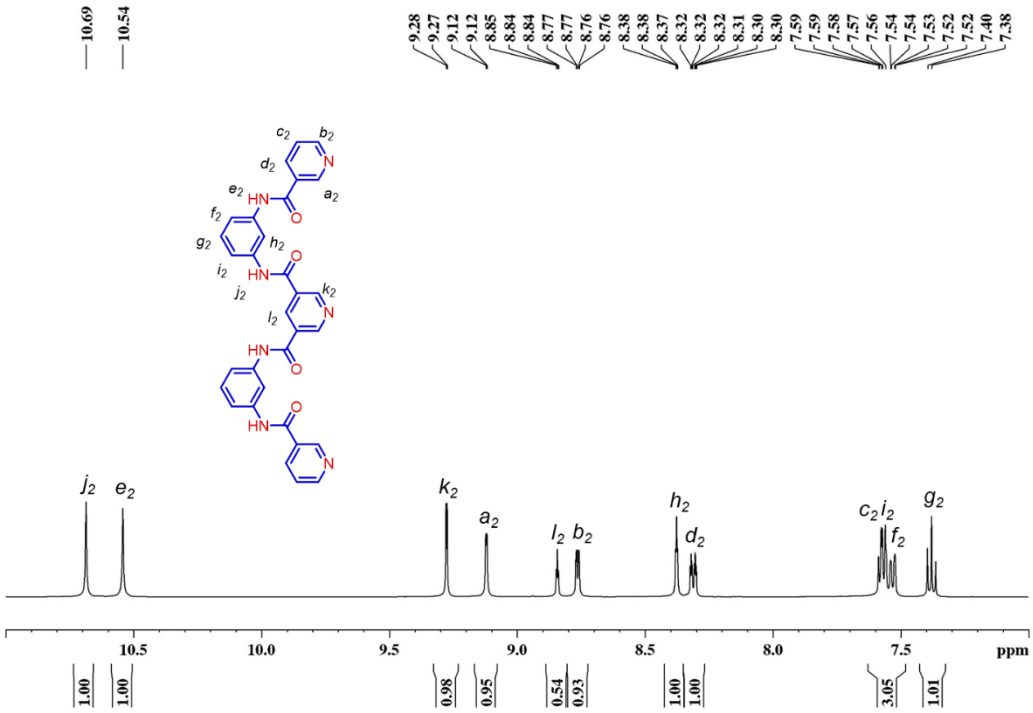

Figure S1a. ^{1}H NMR expansion spectrum (500 MHz, DMSO-d_6, 298 K) of ligand **L2**.

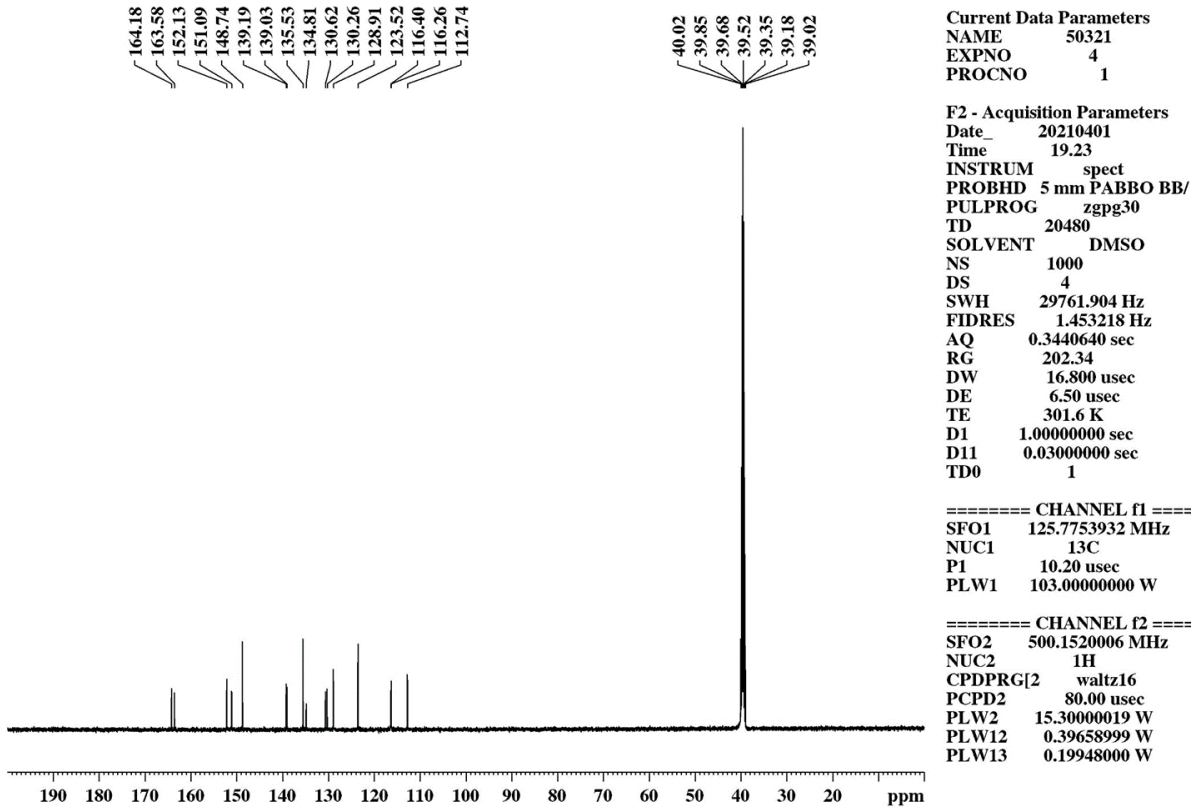

Figure S2. ^{13}C NMR spectrum (125 MHz, DMSO-d_6., 298 K) of ligand **L2**

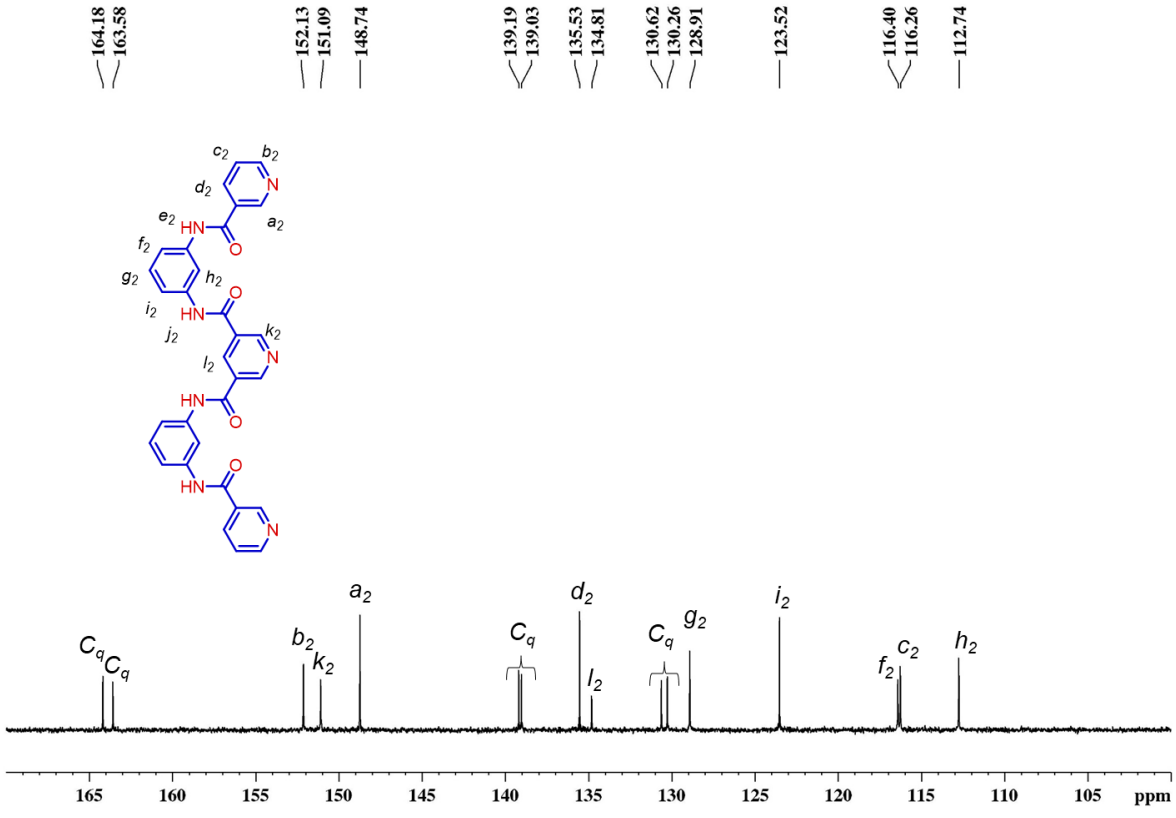

Figure S2a. ^{13}C NMR expansion spectrum (125 MHz, DMSO-d_6, 298 K) of ligand **L2**.

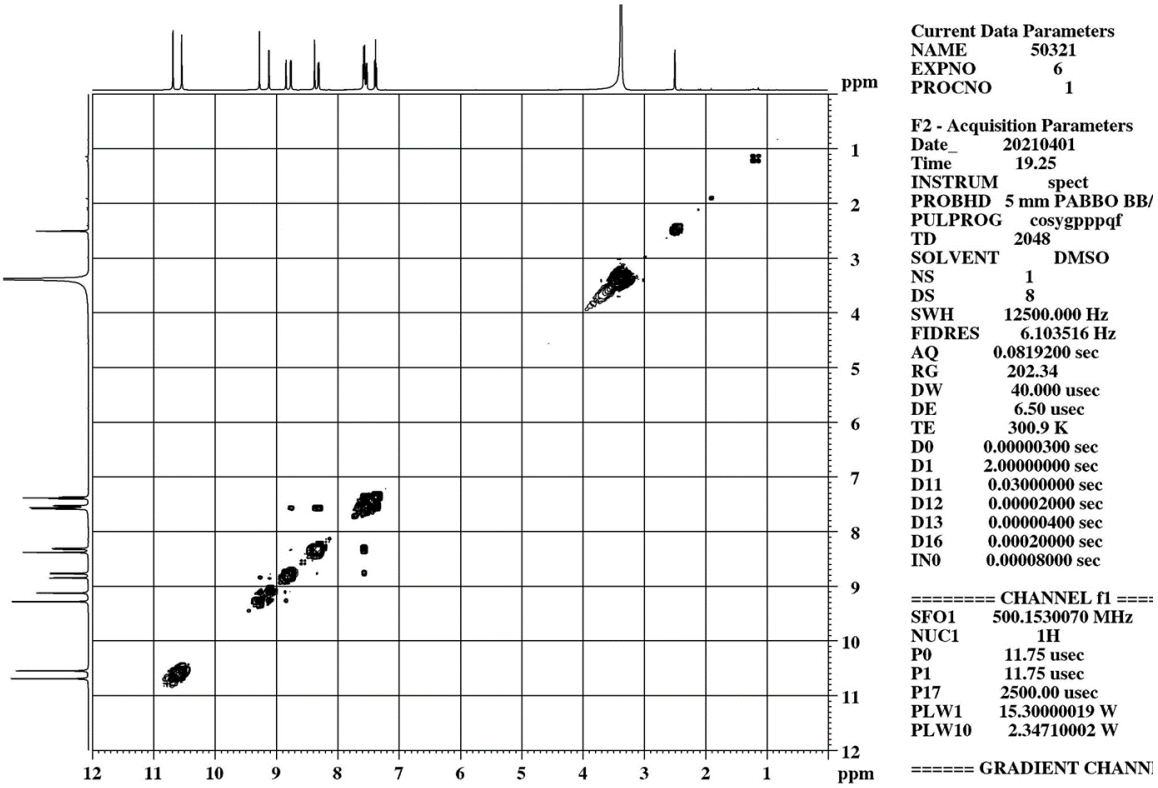

Figure S3. H-H COSY spectrum (500 MHz, DMSO-d_6, 298 K) of ligand **L2**.

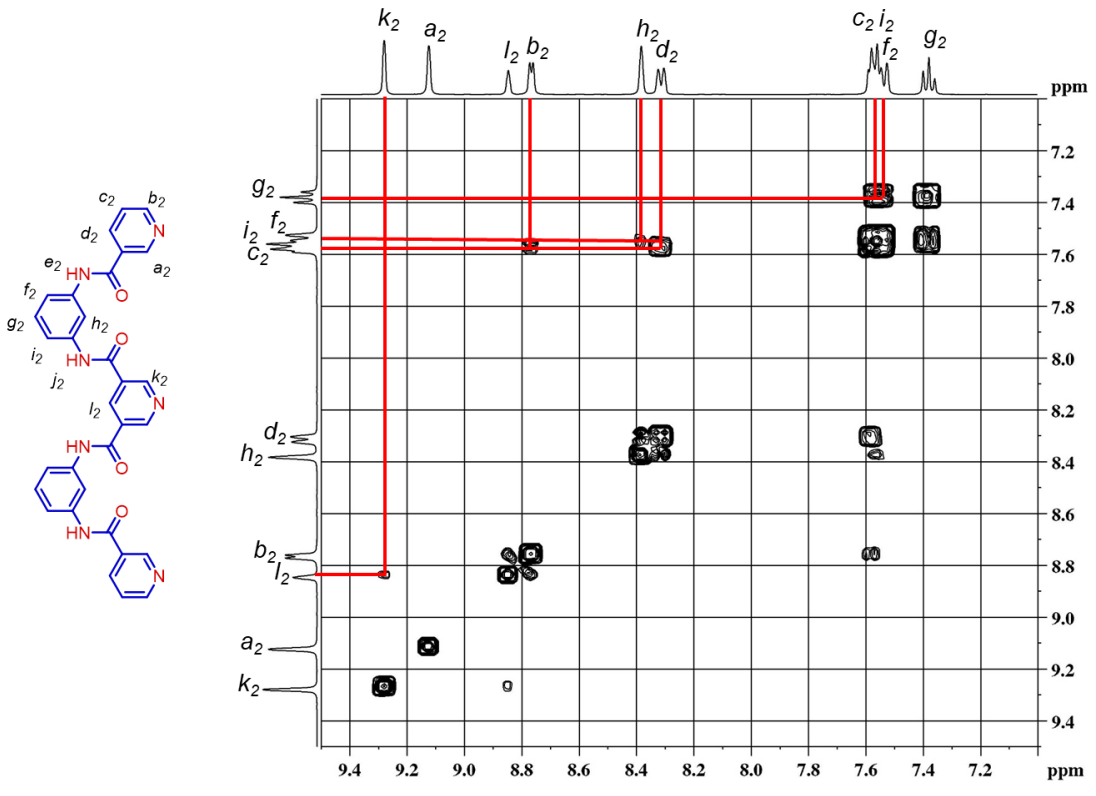

Figure S3a. H-H COSY expansion spectrum (500 MHz, DMSO-d_6, 298 K) of ligand **L2**.

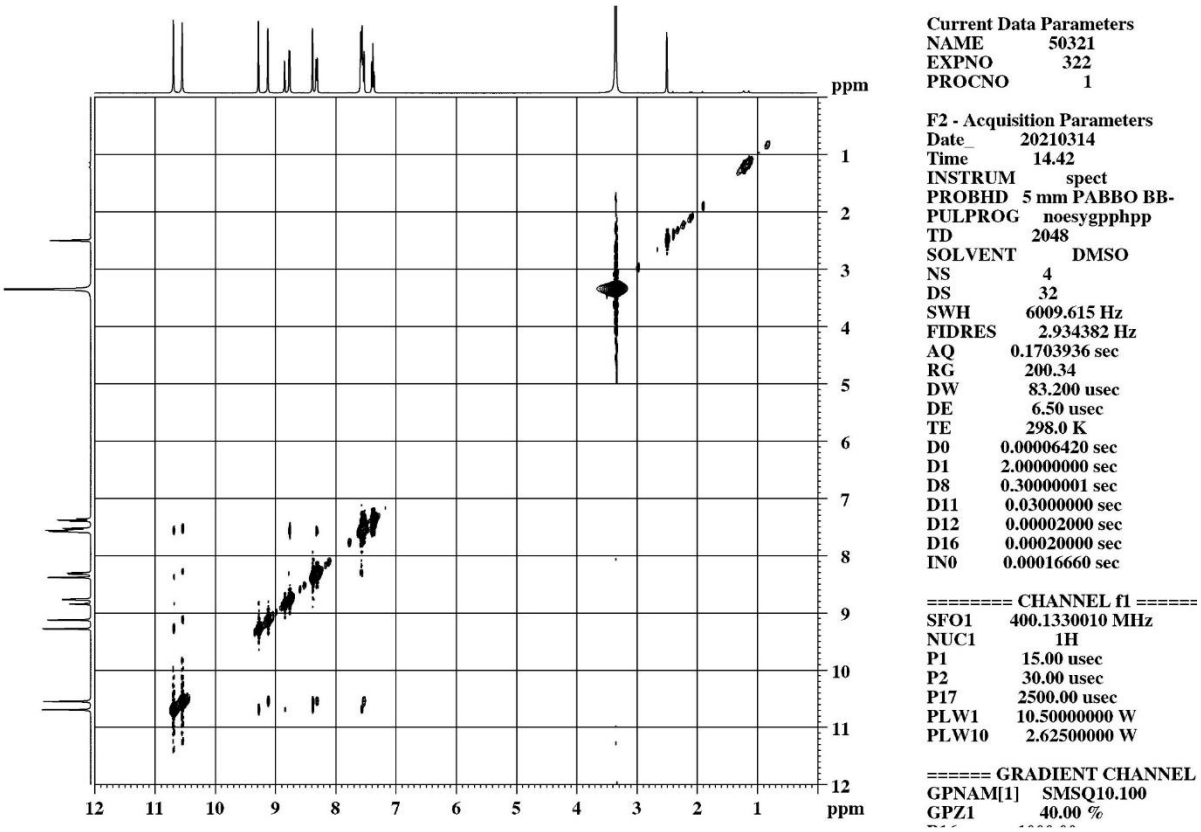

Figure S4. H-H NOESY spectrum (500 MHz, DMSO-d_6, 298 K) of ligand **L2**.

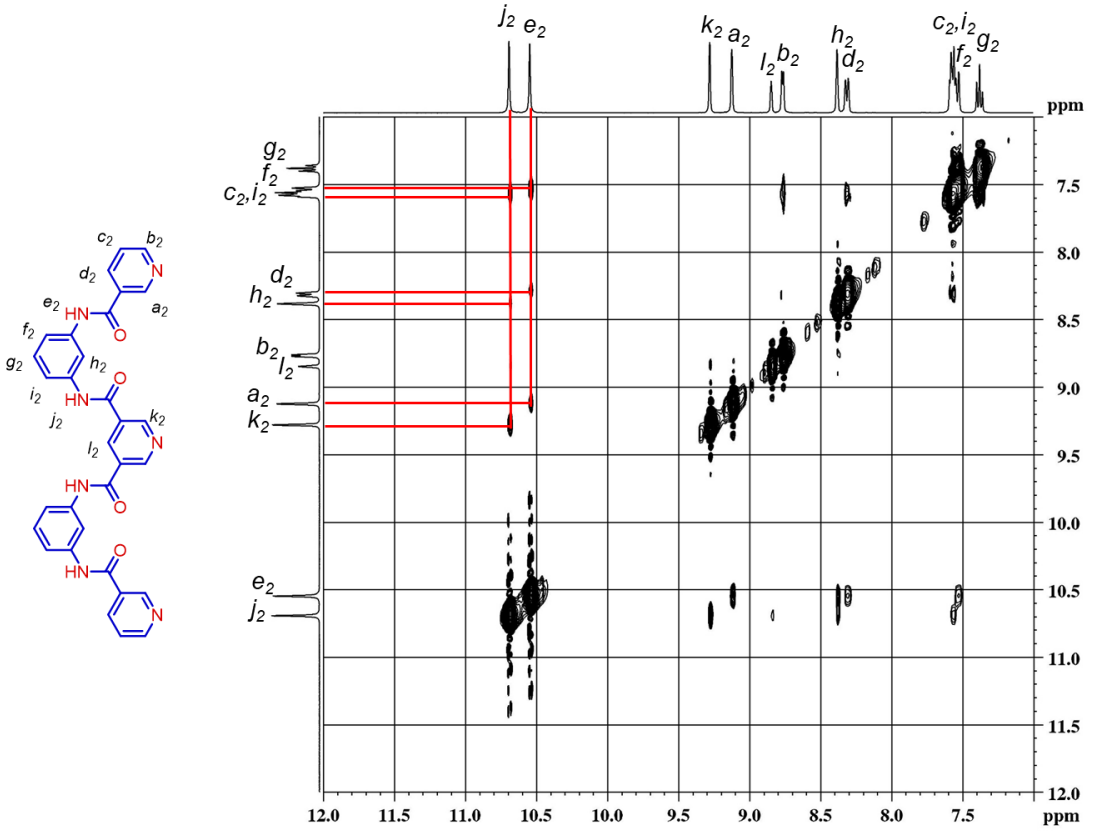

Figure S4a. H-H NOESY expansion spectrum (500 MHz, DMSO-d_6, 298 K) of ligand **L2**.

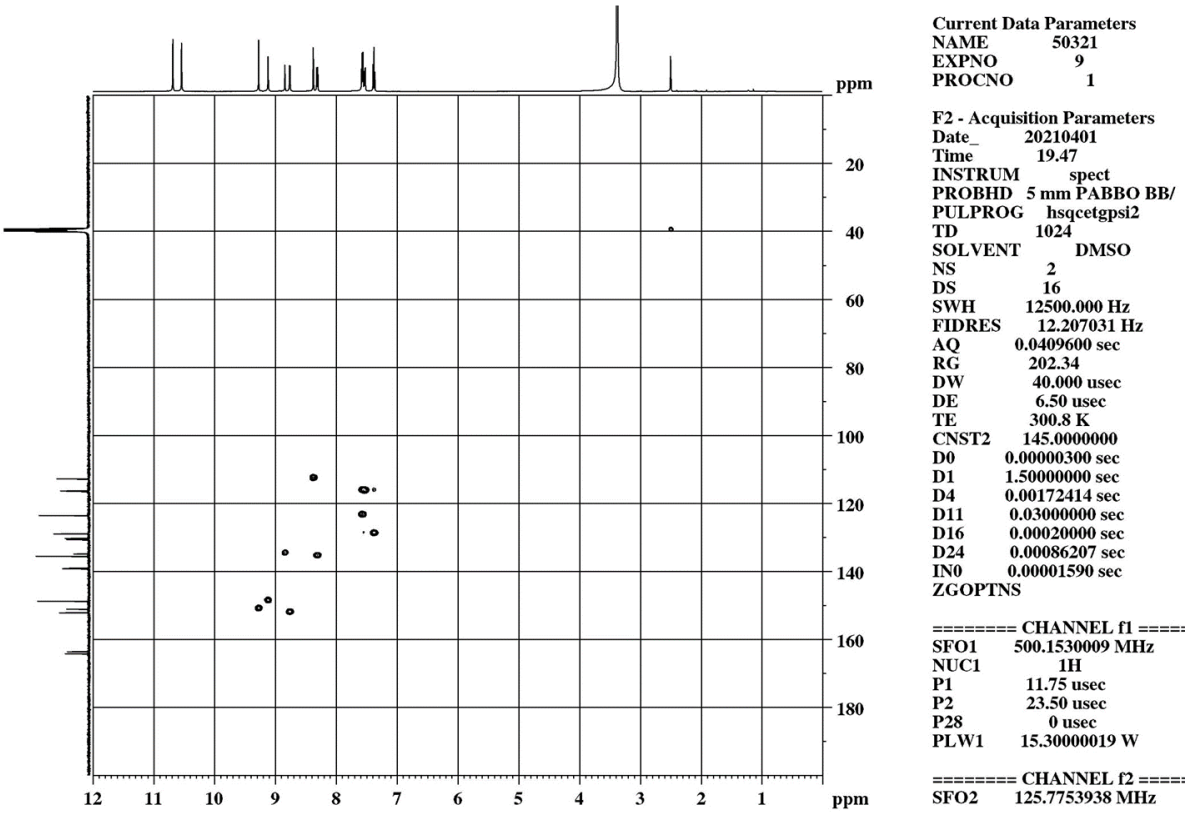

Figure S5. C-H COSY (500/125 MHz, 298 K) spectrum of ligand **L2** in DMSO-d_6.

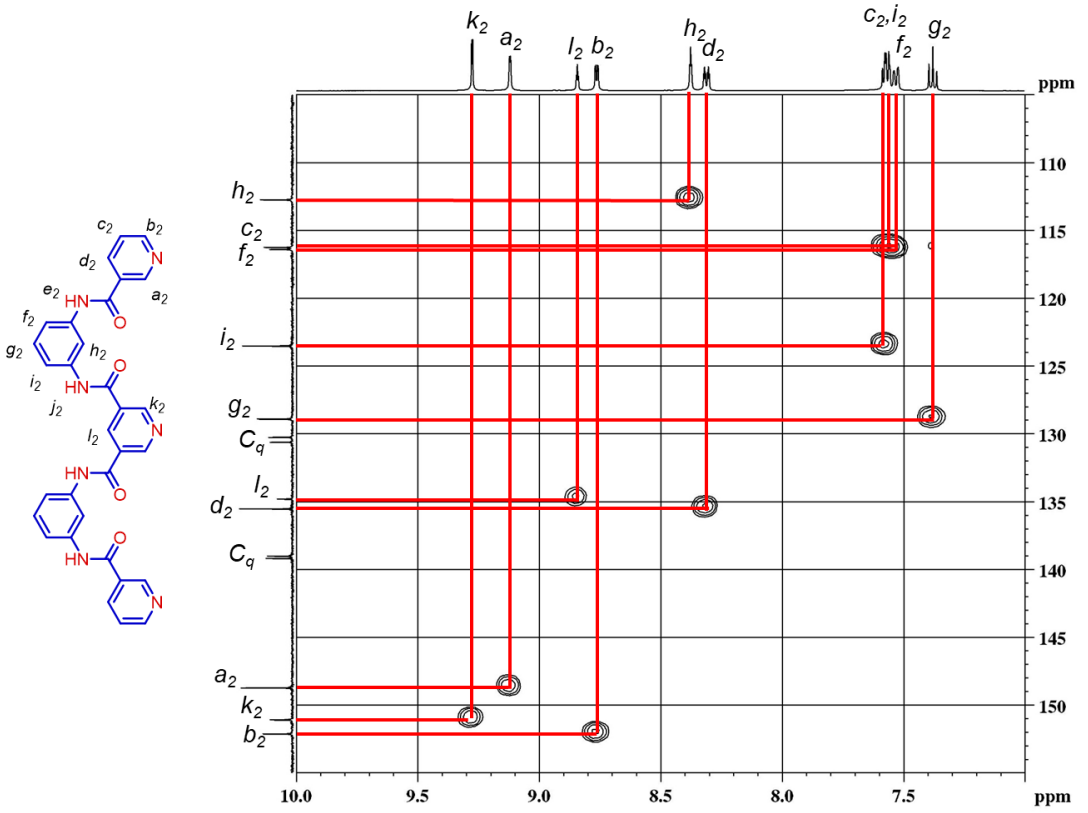

Figure S5a. C-H COSY (500/125 MHz, 298 K) expansion spectrum of ligand **L2** in DMSO-d_6.

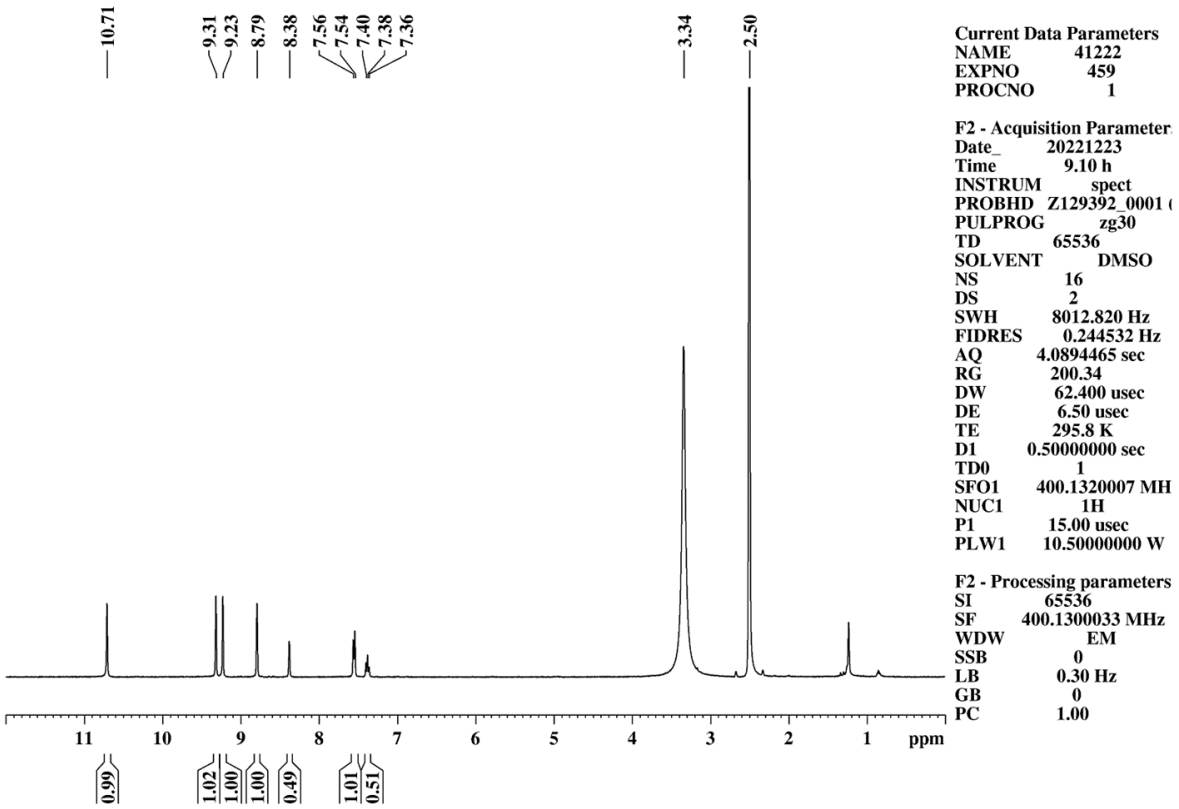

Figure S6. ^{1}H NMR (400 MHz, 298 K) spectrum of fragment **C** in DMSO-d_6.

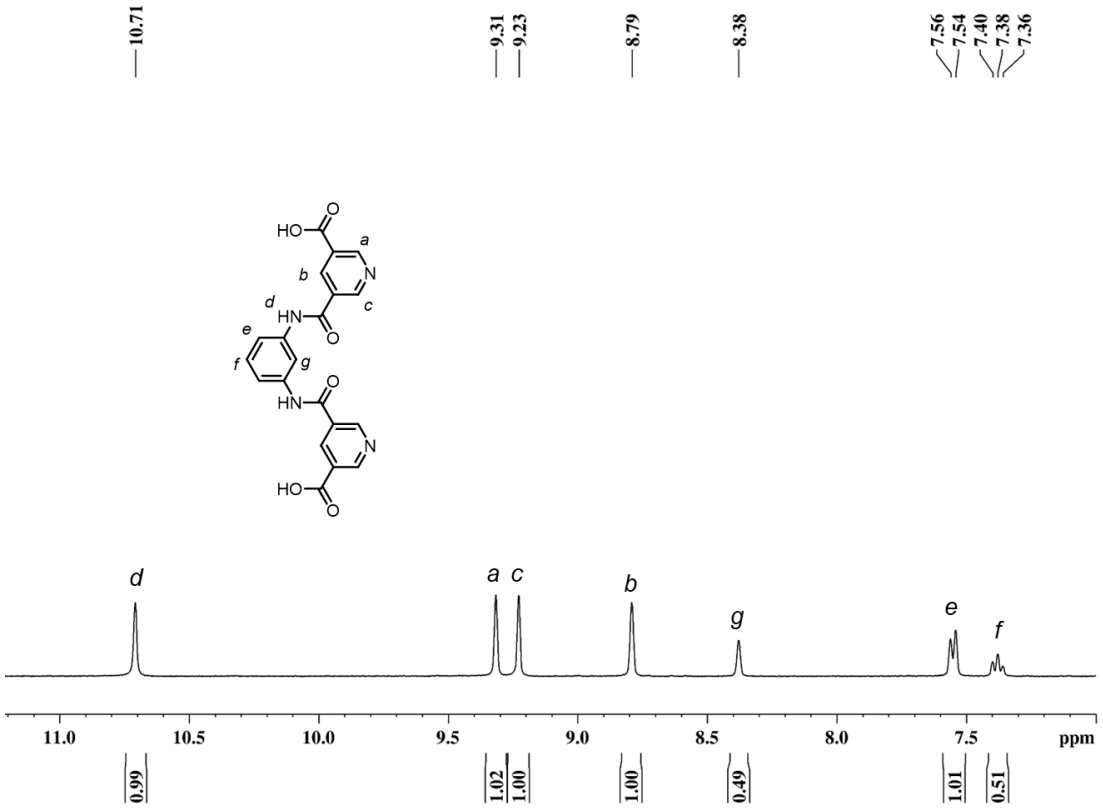

Figure S6a. ^{1}H NMR (400 MHz, 298 K) expansion spectrum of fragment **C** in DMSO-d_6.

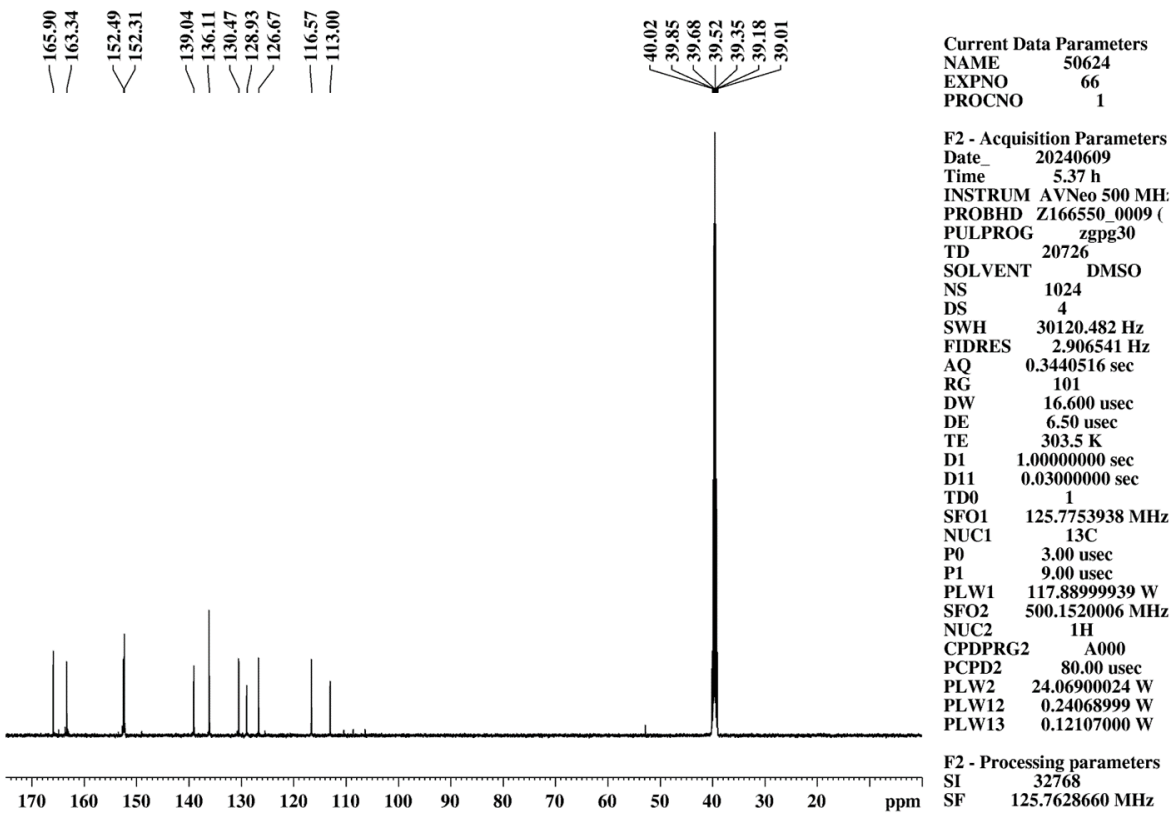

Figure S7. ^{13}C NMR (125 MHz, 298 K) spectrum of fragment **C** in DMSO-d_6.

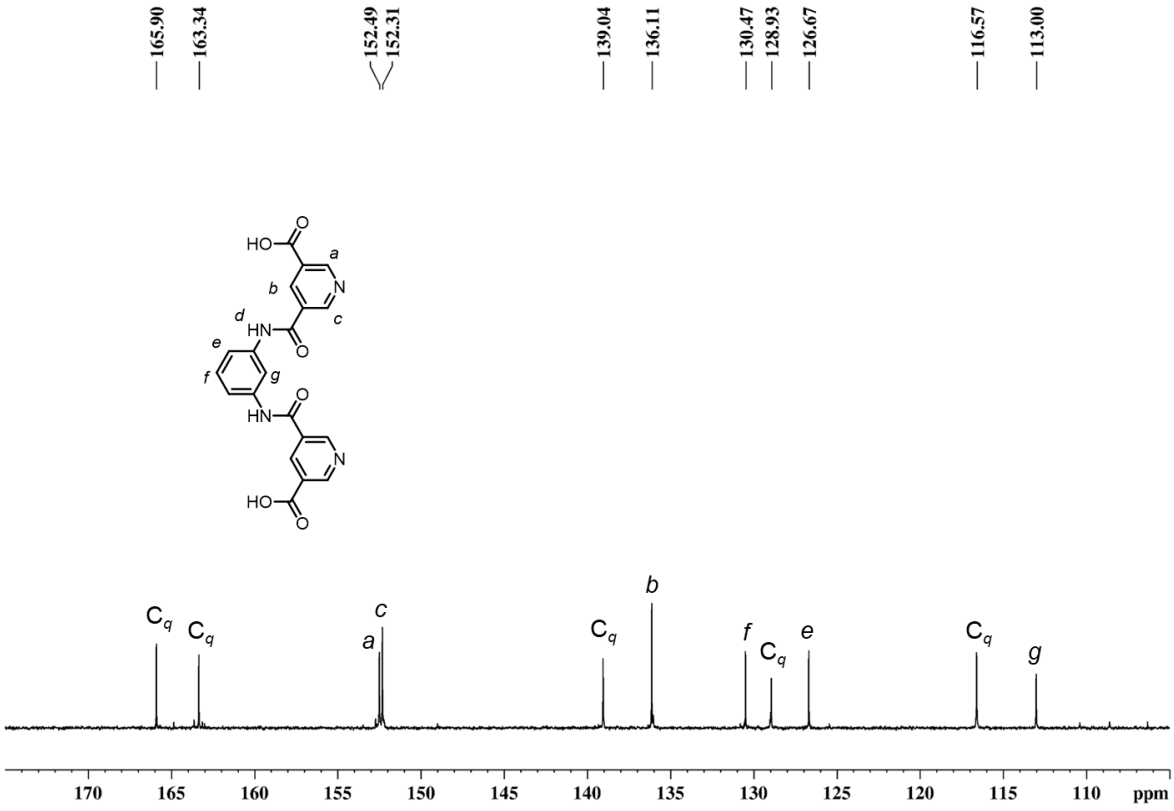

Figure S7a. ^{13}C NMR (125 MHz, 298 K) expansion spectrum of fragment **C** in DMSO-d_6.

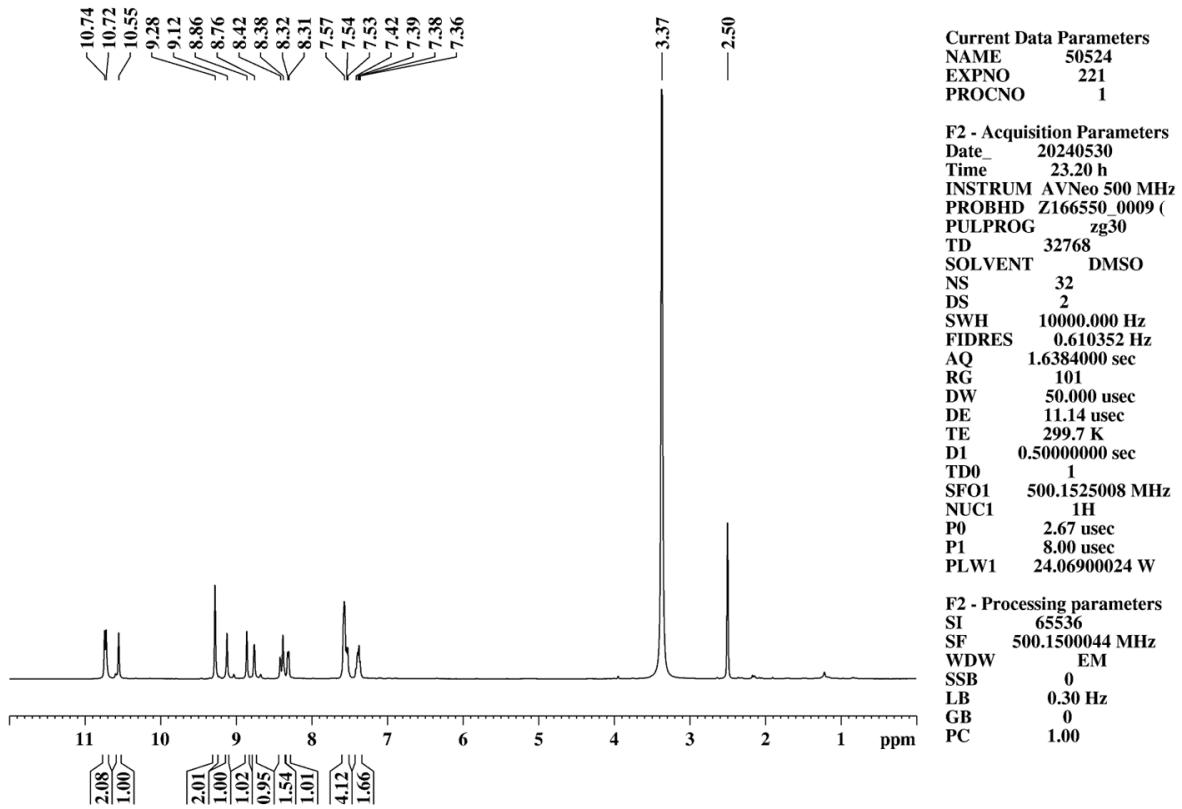

Figure S8. [1]H NMR (500 MHz, 298 K) spectrum of ligand **L3** in DMSO-d_6.

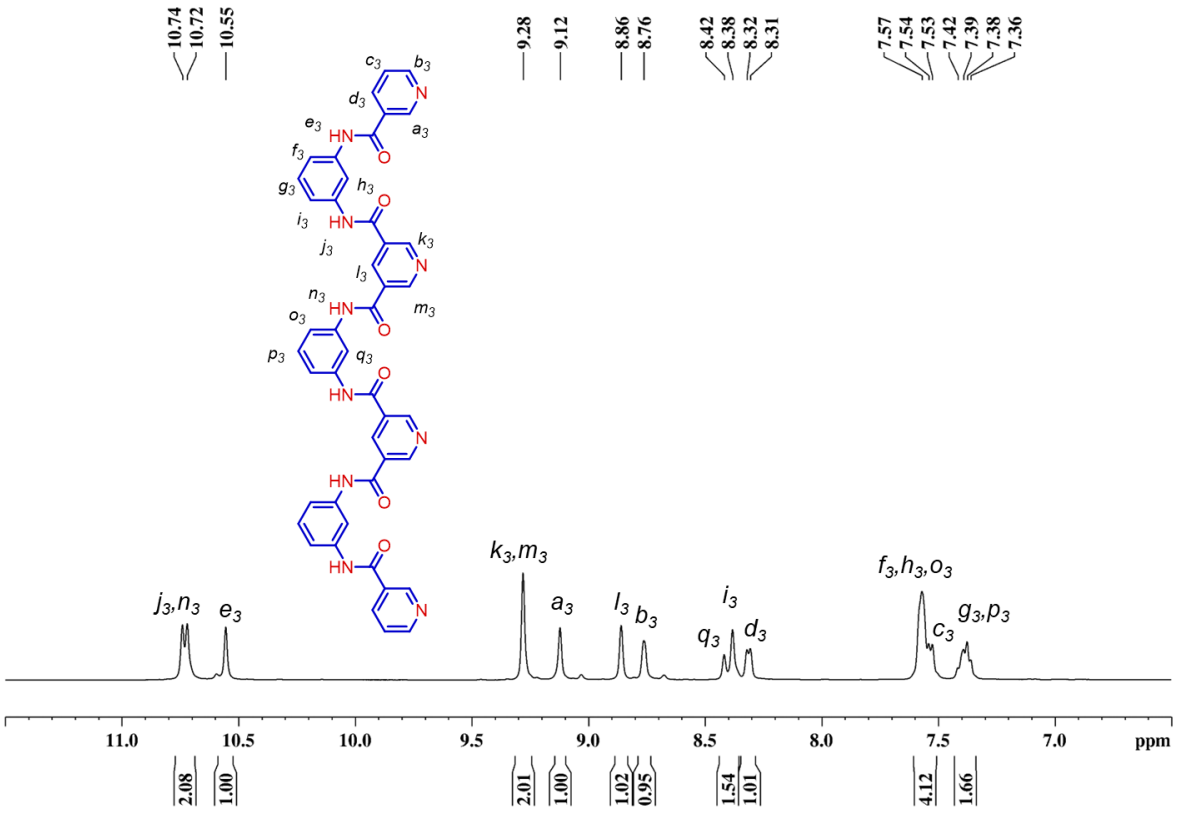

Figure S8a. [1]H NMR (500 MHz, 298 K) expansion spectrum of ligand **L3** in DMSO-d_6.

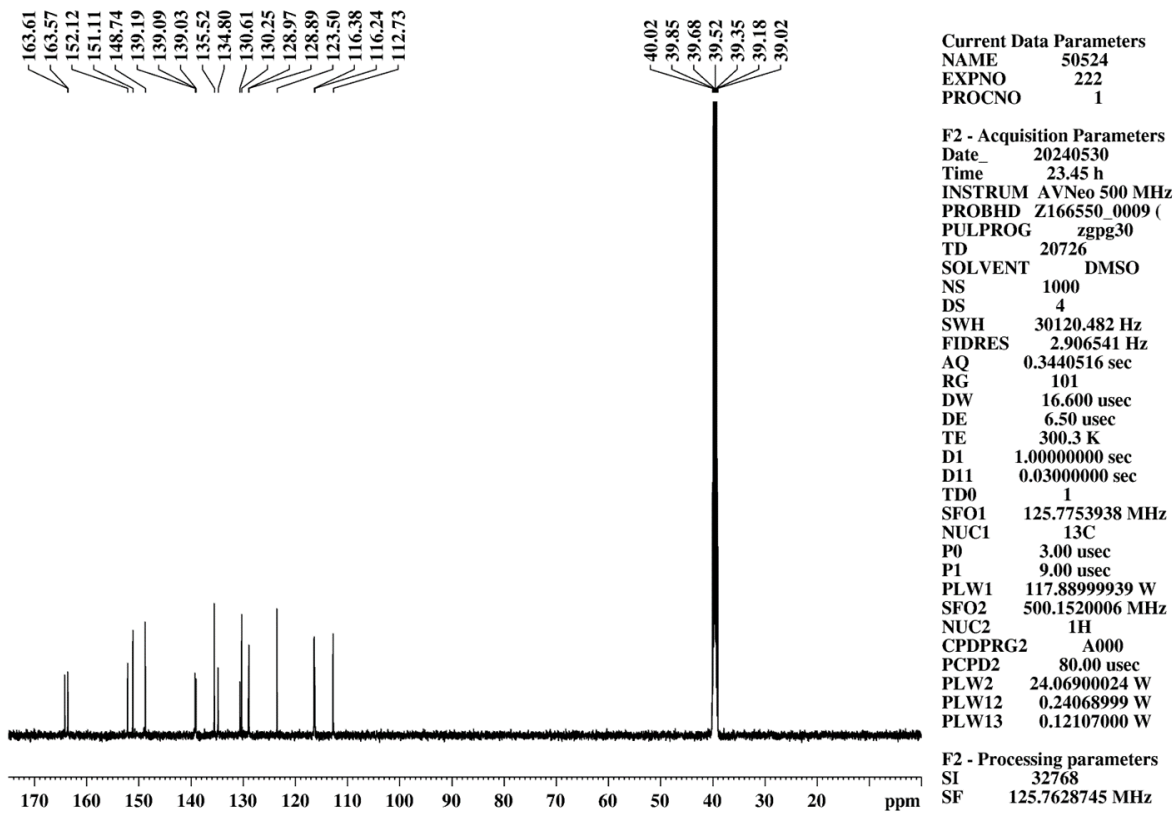

Figure S9. ^{13}C NMR (125 MHz, 298 K) spectrum of ligand **L3** in DMSO-d_6.

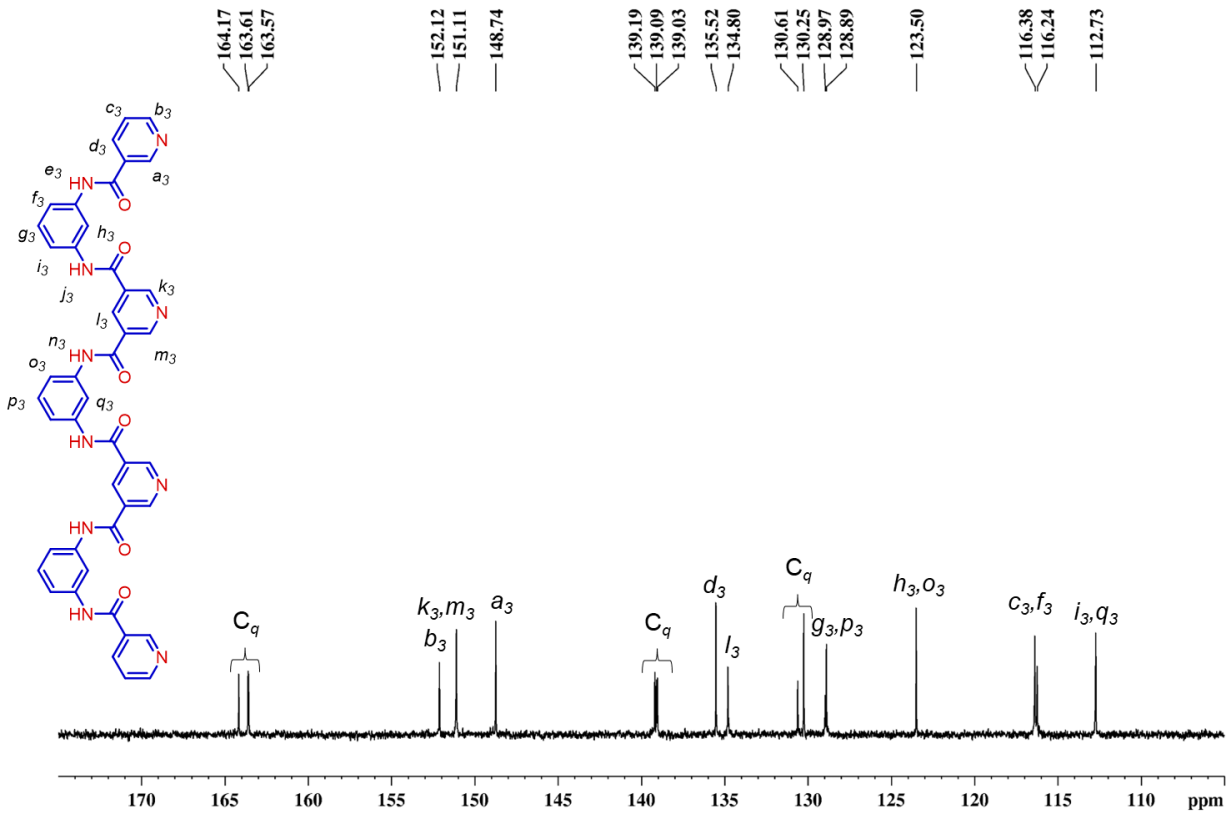

Figure S9a. ^{13}C NMR (125 MHz, 298 K) expansion spectrum of ligand **L3** in DMSO-d_6.

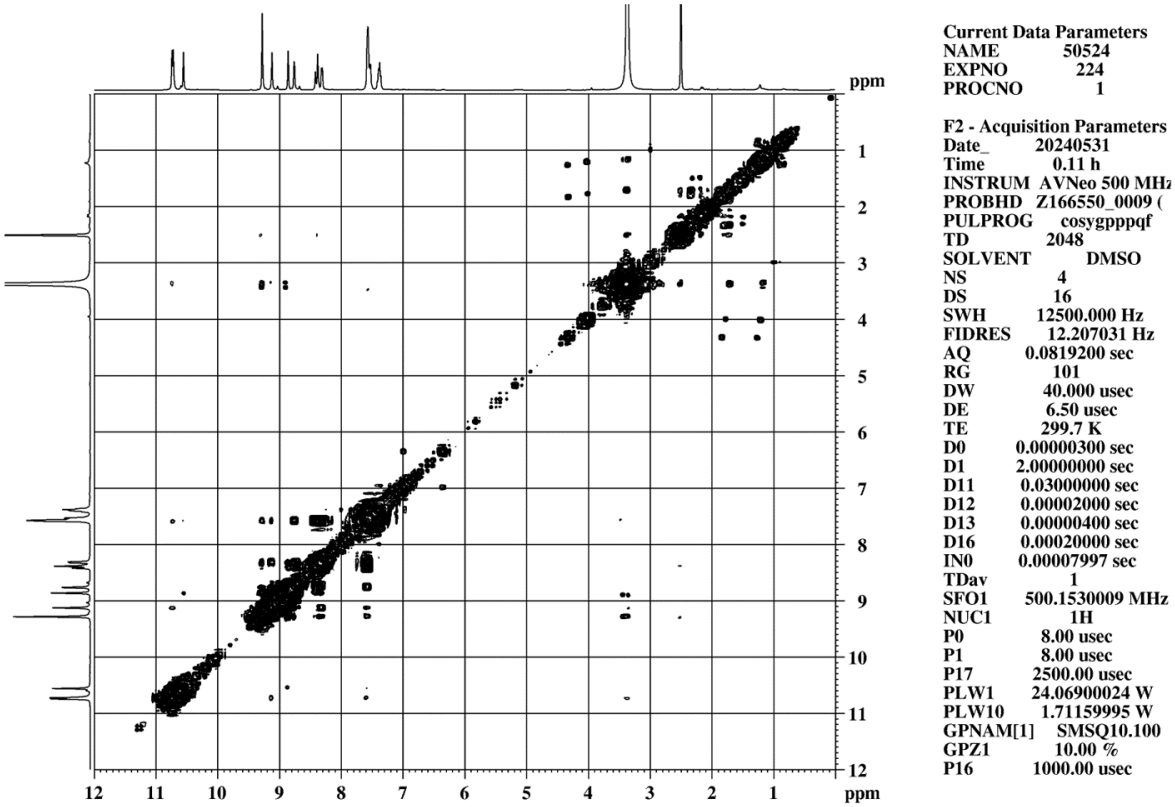

Figure S10. H-H COSY (500 MHz, 298 K) spectrum of ligand, **L3** in DMSO-d_6.

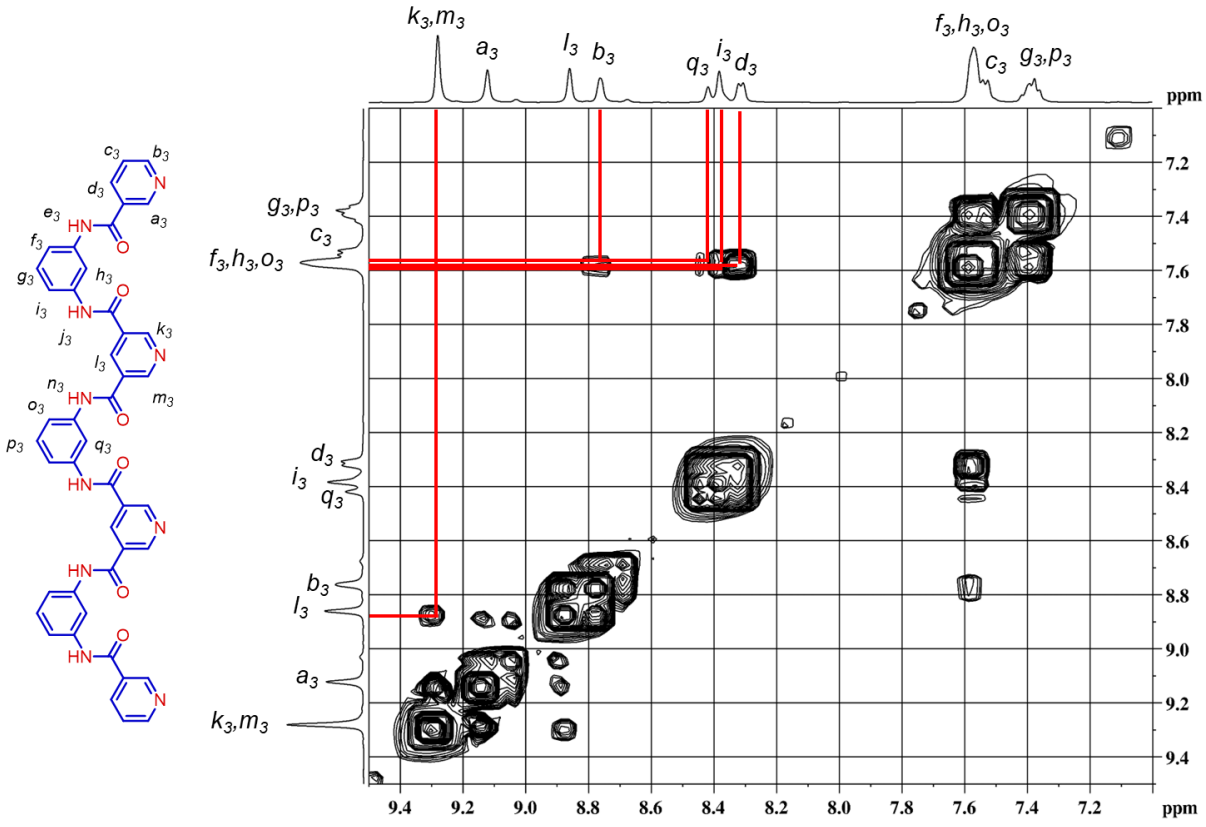

Figure S10a. H-H COSY (500 MHz, 298 K) expansion spectrum of ligand **L3** in DMSO-d_6.

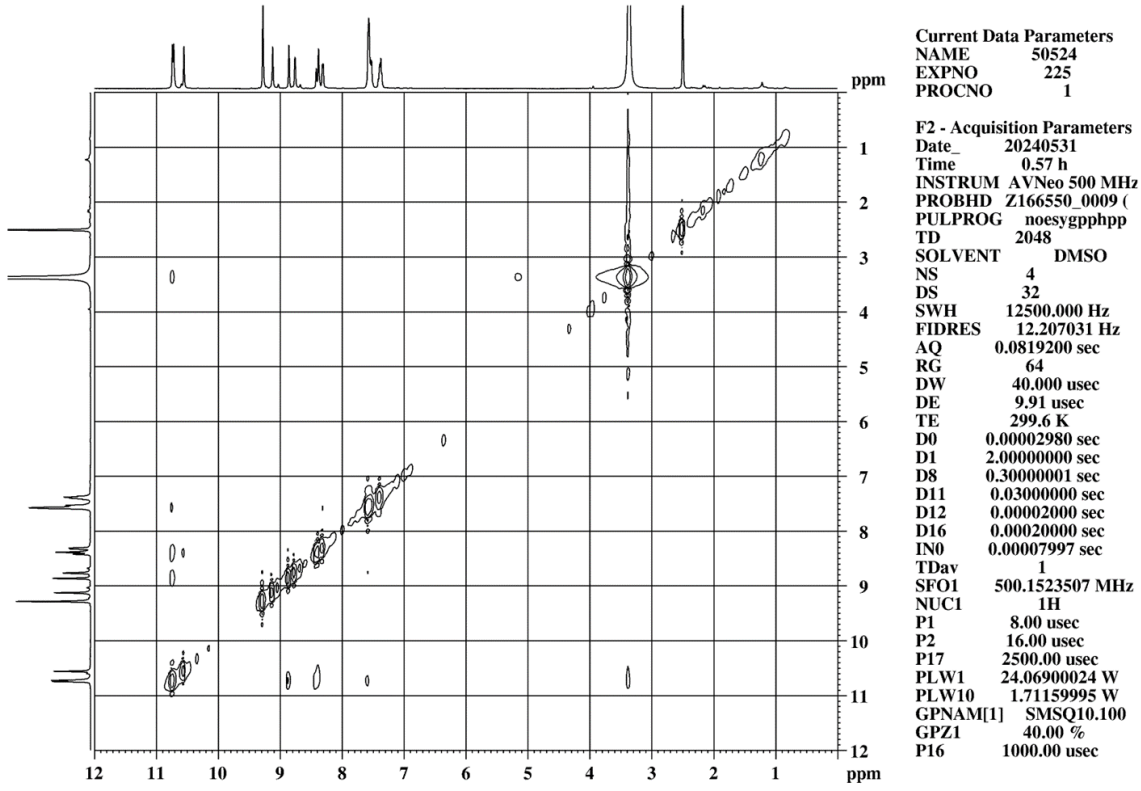

Figure S11. H-H NOESY (500 MHz, 298 K) spectrum of ligand **L3** in DMSO-d_6.

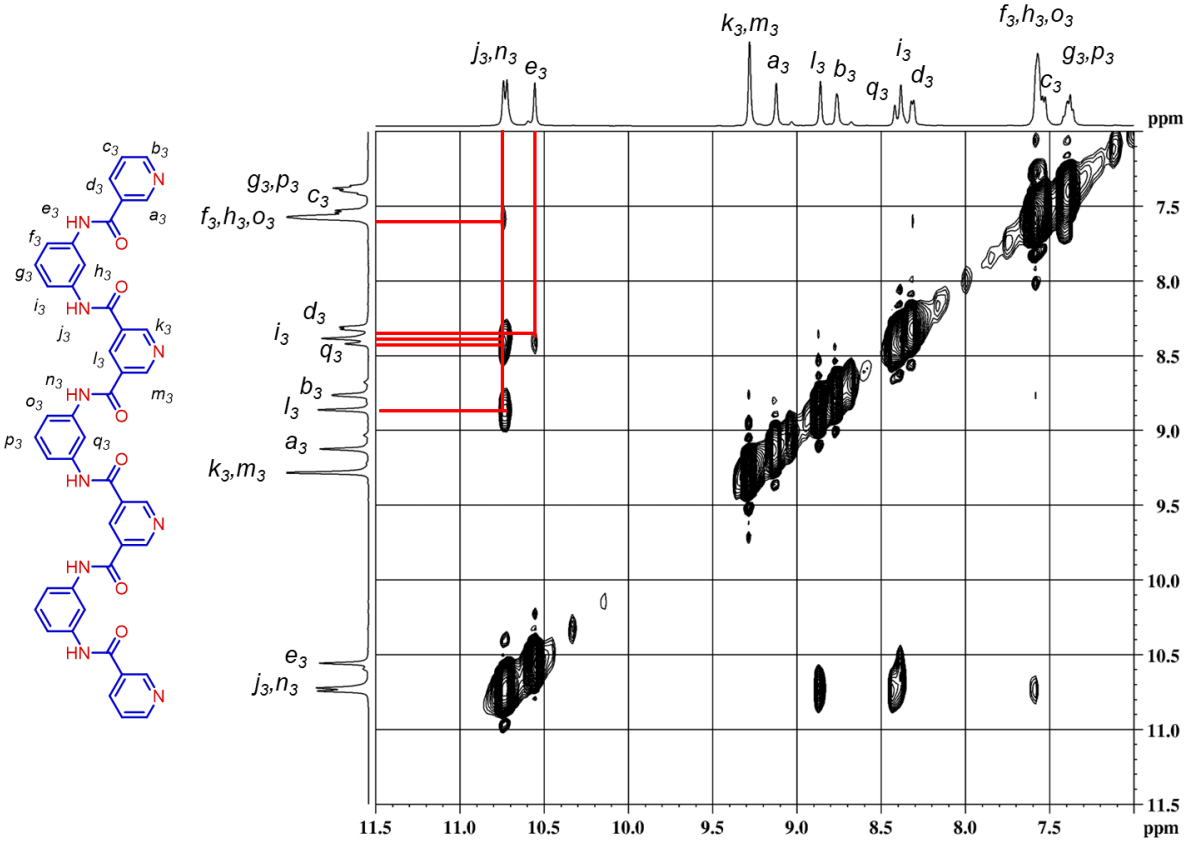

Figure S11a. H-H NOESY (500 MHz, 298 K) expansion spectrum of ligand **L3** in DMSO-d_6.

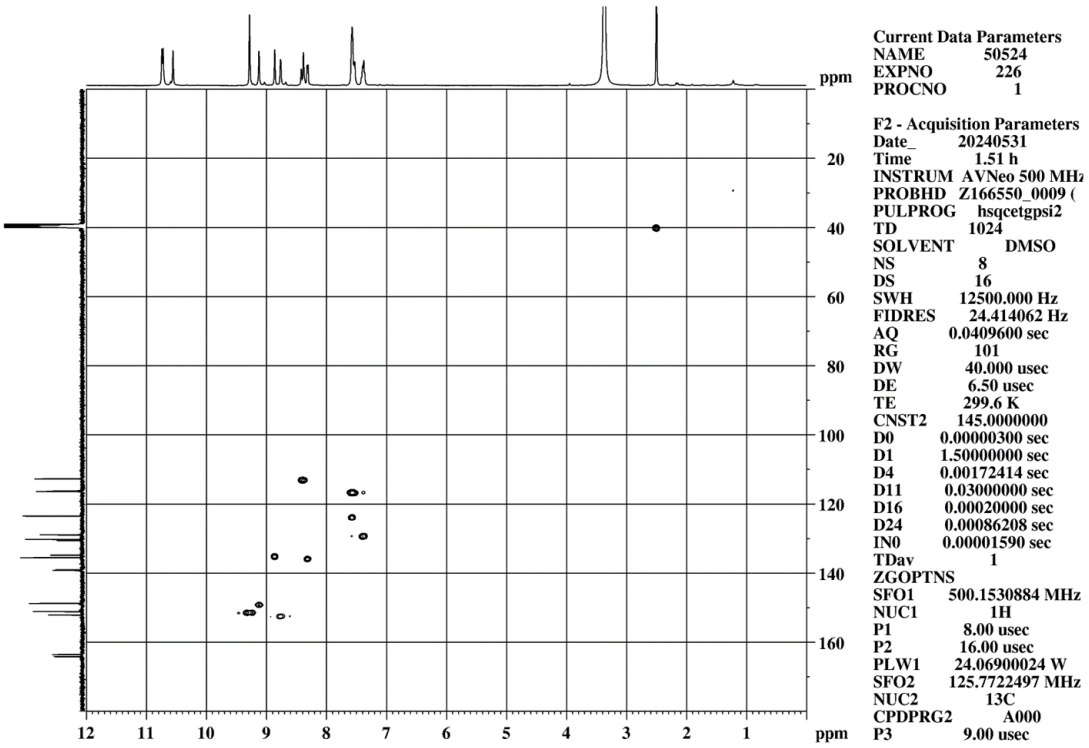

Figure S12. C-H COSY (500/125 MHz, 298 K) spectrum of ligand **L3** in DMSO-d_6.

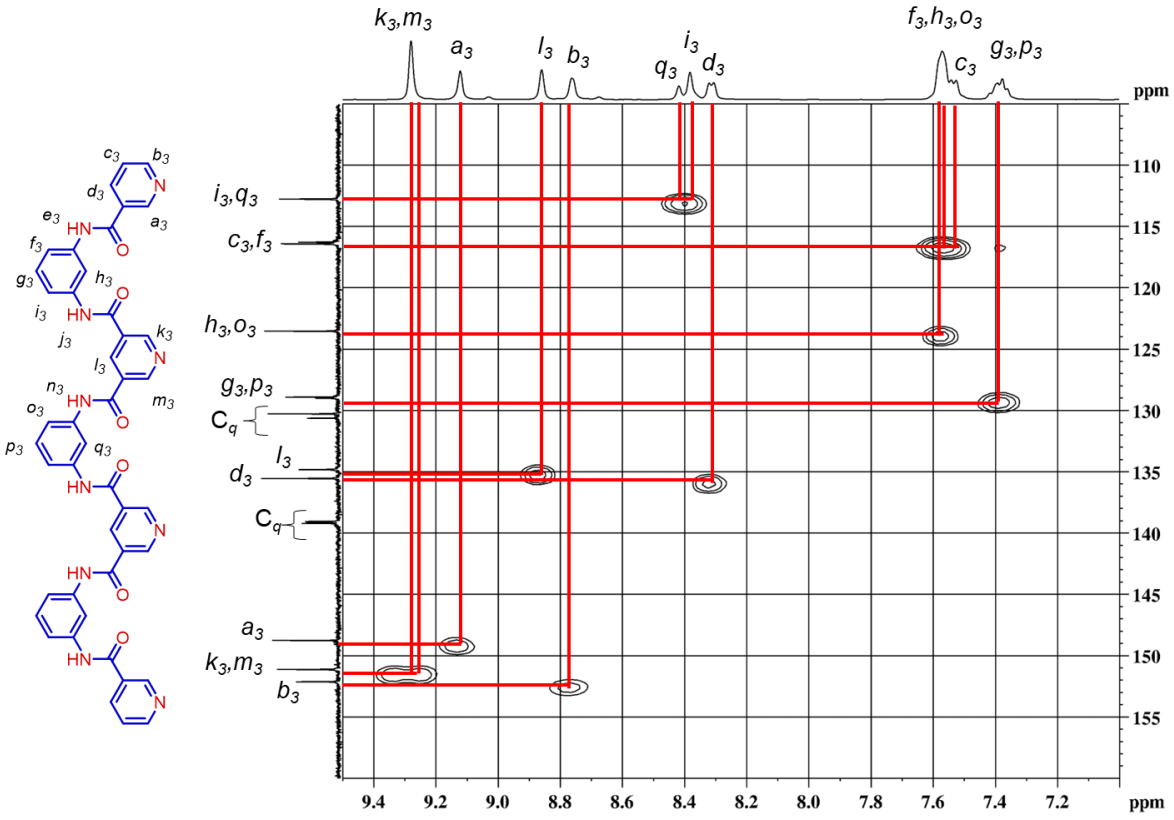

Figure S12a. C-H COSY (500/125 MHz, 298 K) expansion spectrum of ligand **L3** in DMSO-d_6.

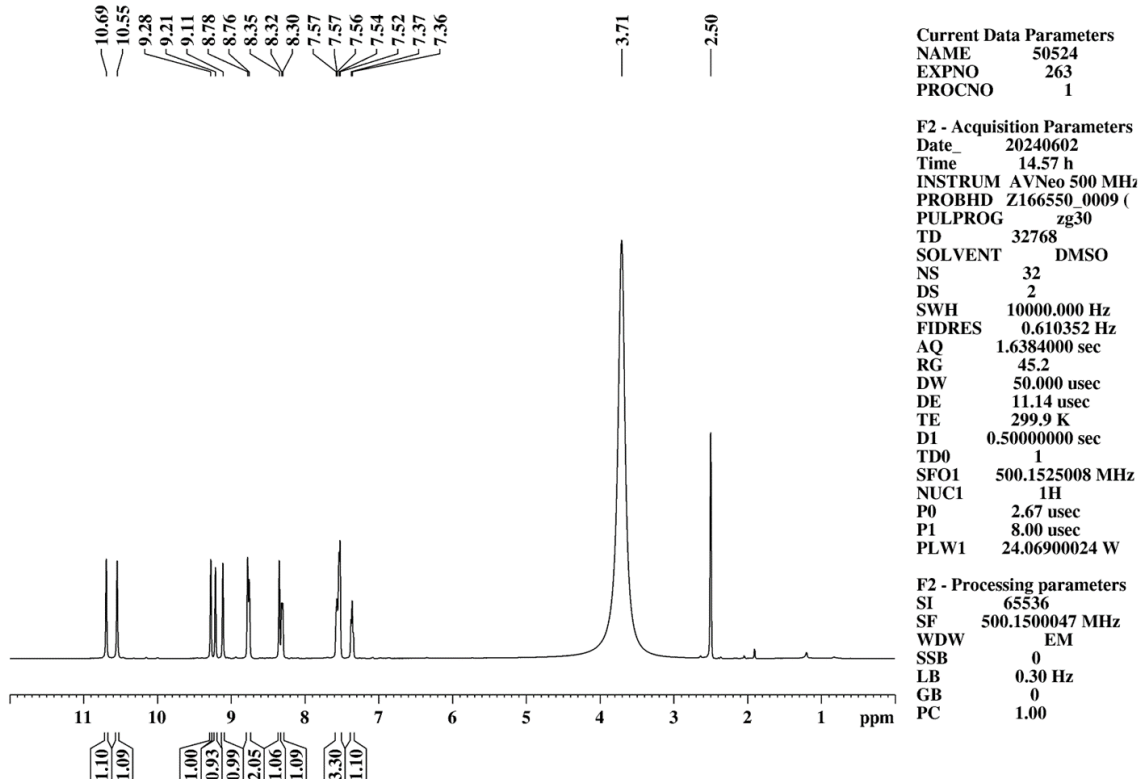

Figure S13. ^{1}H NMR (500 MHz, 298 K) spectrum of fragment **D** in DMSO-d_6.

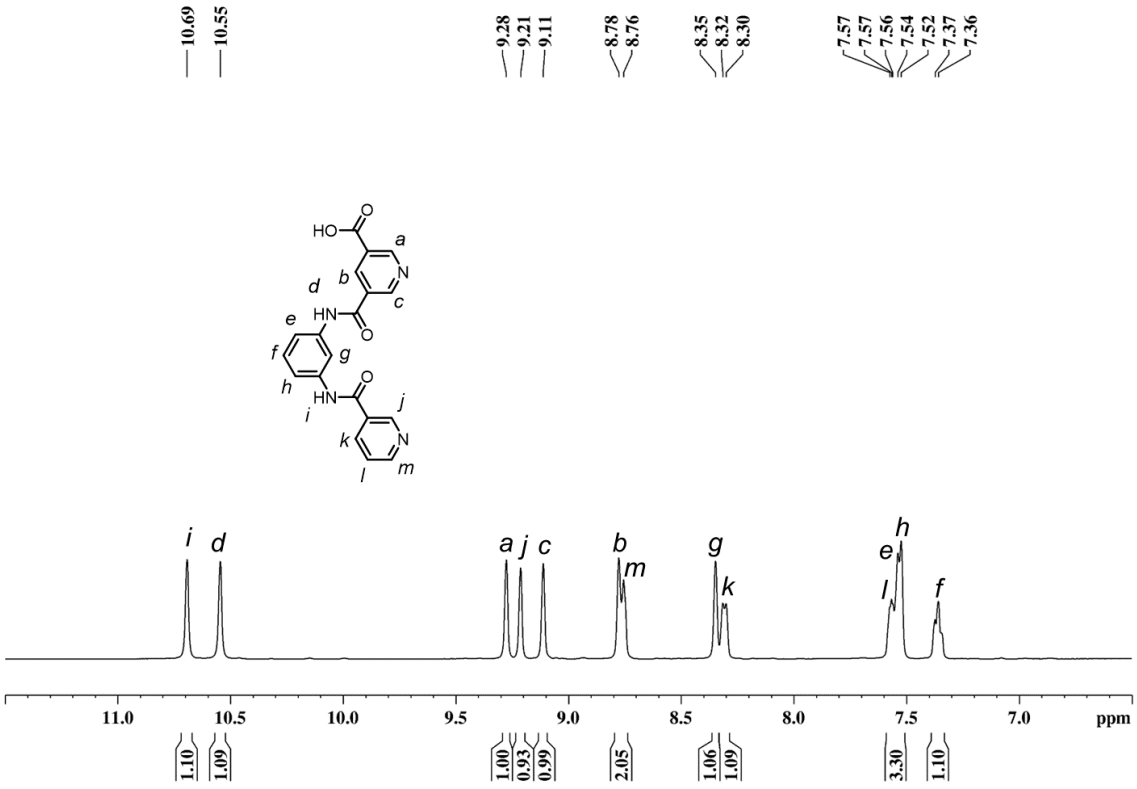

Figure S13a. ^{1}H NMR (500 MHz, 298 K) expansion spectrum of fragment **D** in DMSO-d_6.

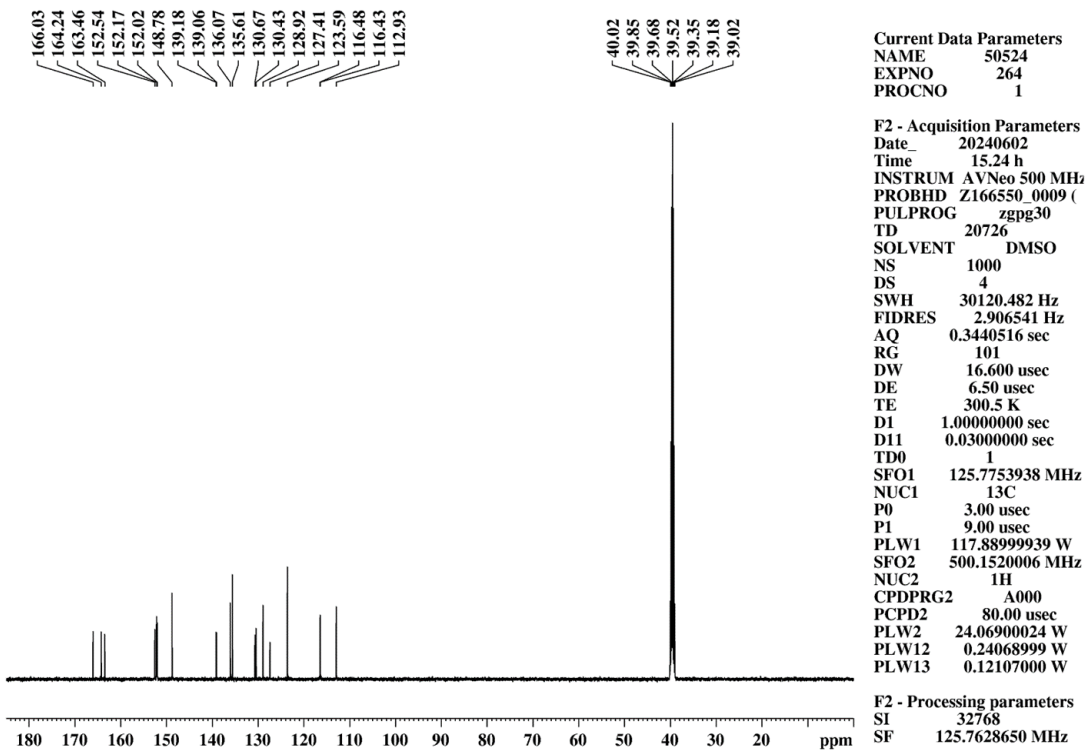

Figure S14. ^{13}C NMR (125 MHz, 298 K) spectrum of fragment **D** in DMSO-d_6.

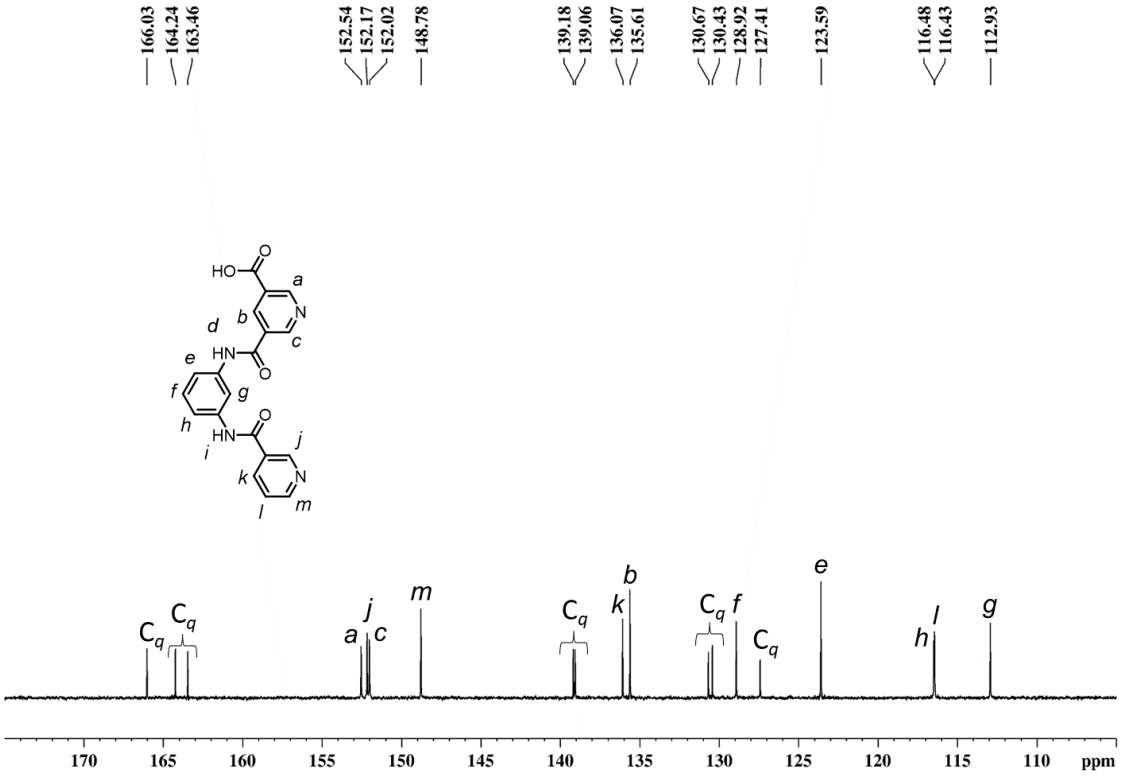

Figure S14a. ^{13}C NMR (125 MHz, 298 K) expansion spectrum of fragment **D** in DMSO-d_6.

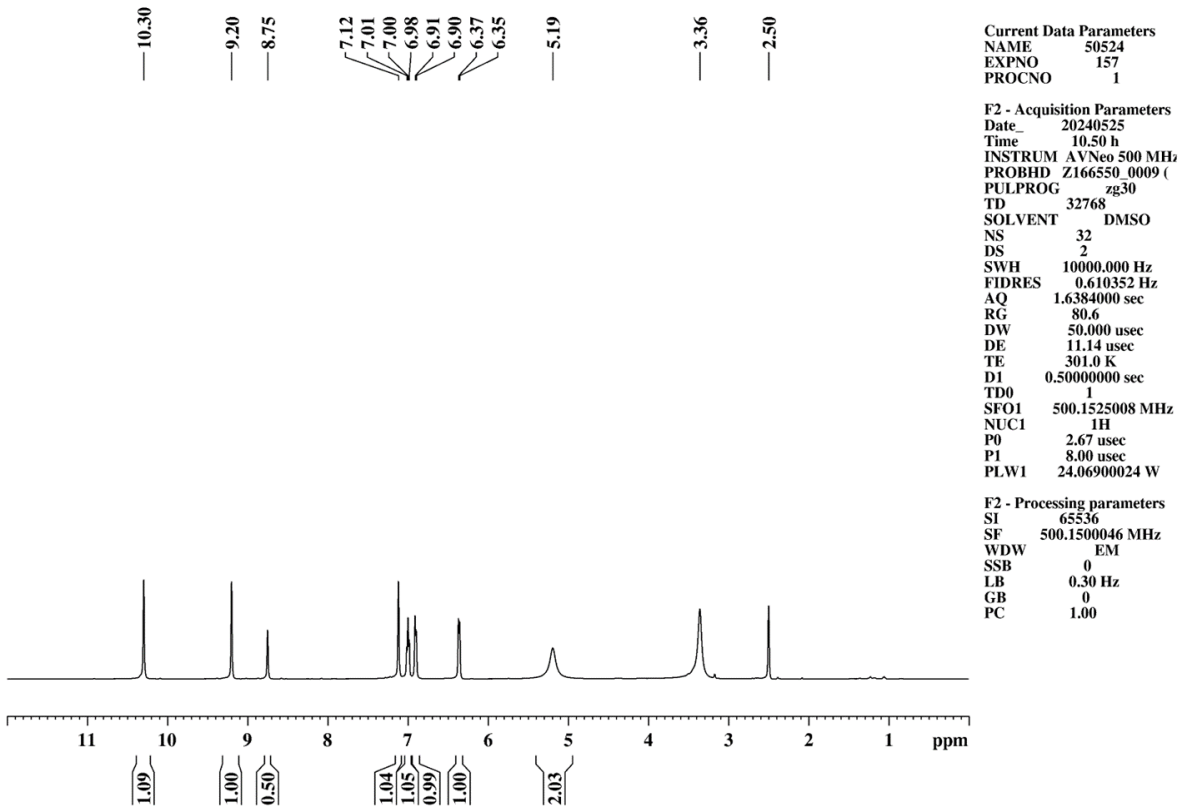

Figure S15. ^{1}H NMR (500 MHz, 298 K) spectrum of fragment **E** in DMSO-d_6.

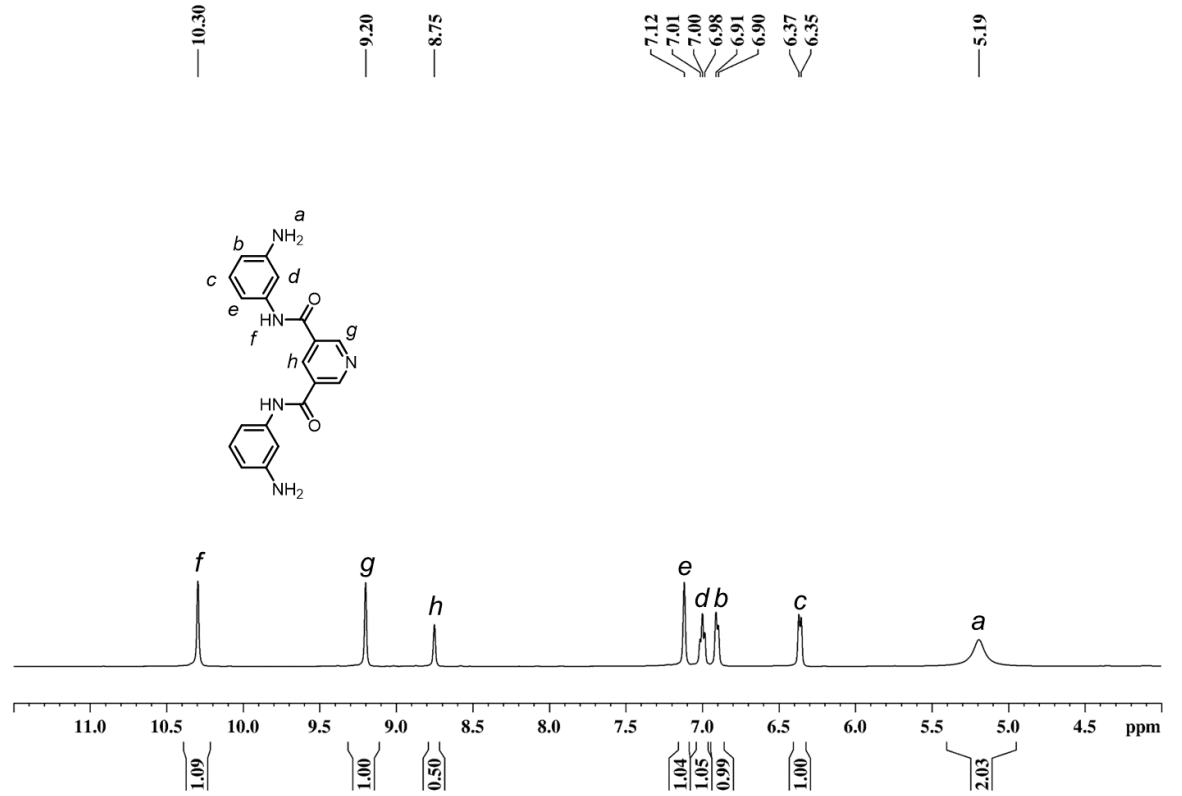

Figure S15a. ^{1}H NMR (500 MHz, 298 K) expansion spectrum of fragment **E** in DMSO-d_6.

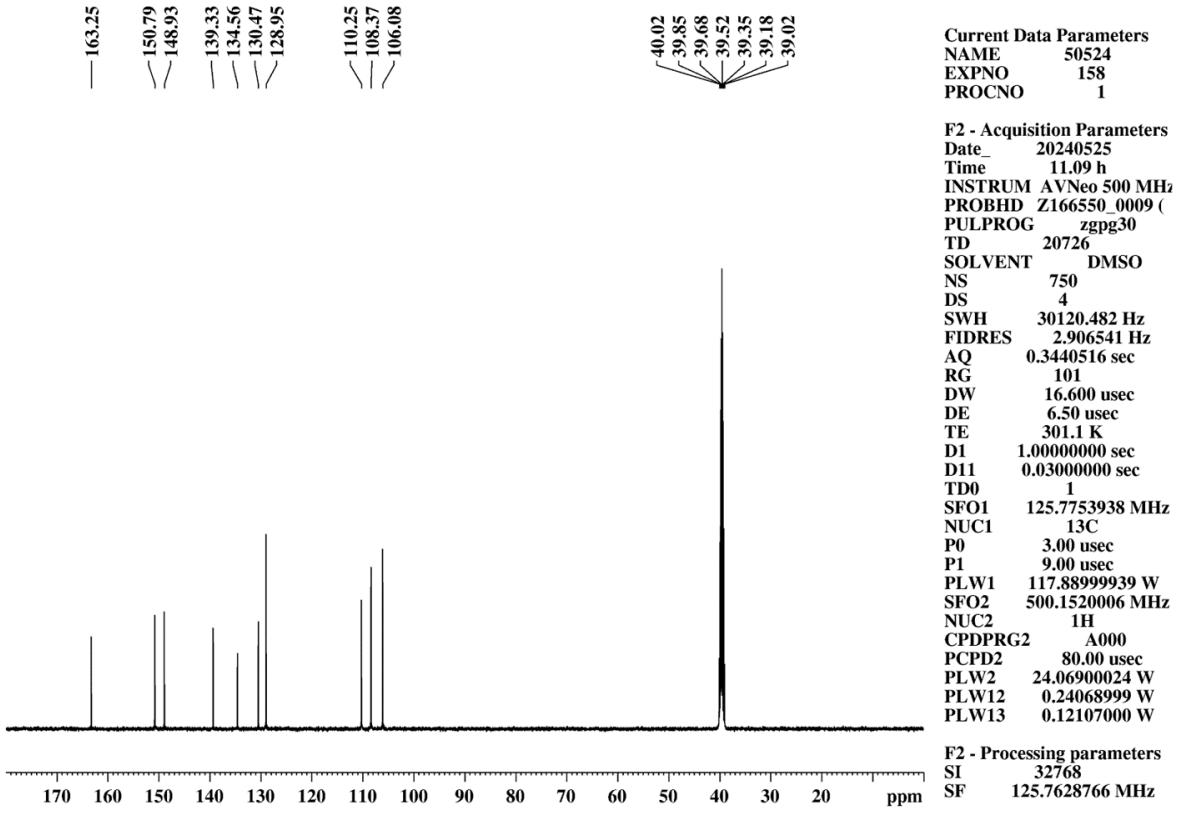

Figure S16. ^{13}C NMR (125 MHz, 298 K) spectrum of fragment **E** in DMSO-d_6.

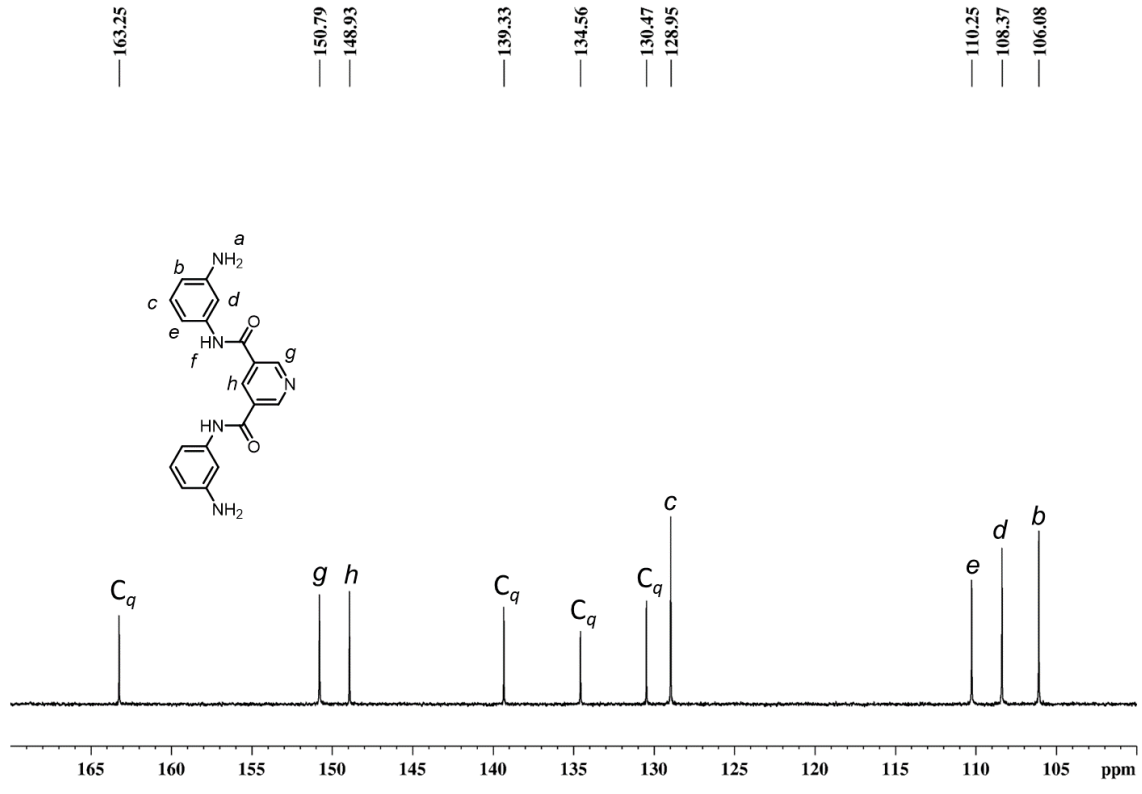

Figure S16a. ^{13}C NMR (125 MHz, 298 K) expansion spectrum of fragment **E** in DMSO-d_6.

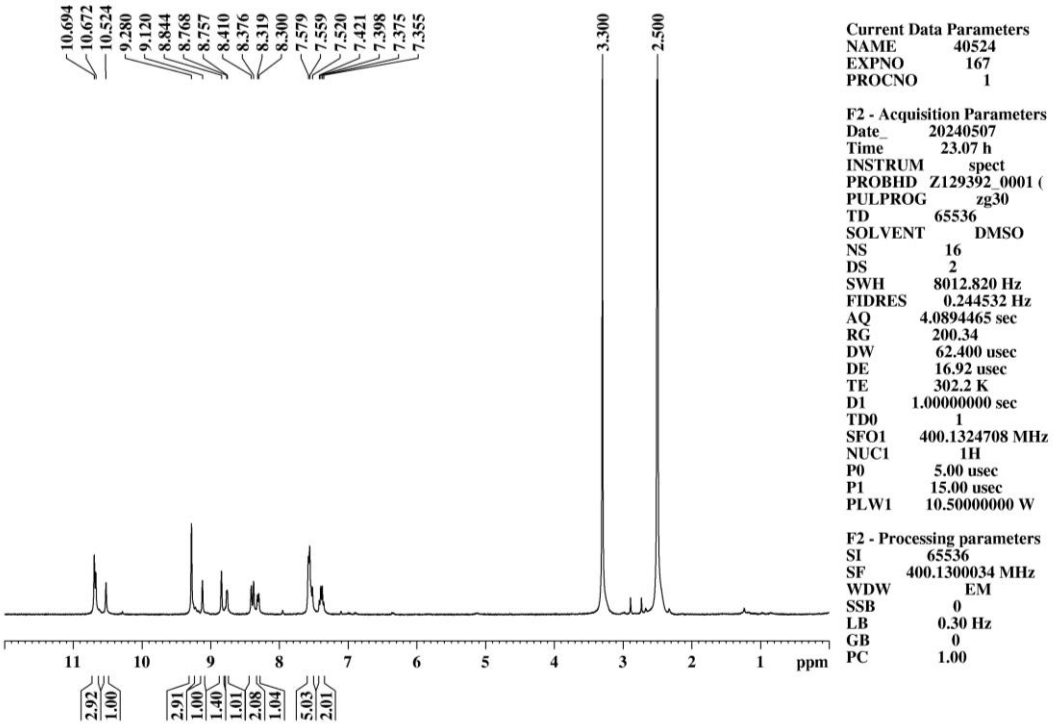

Figure S17. [1]H NMR (500 MHz, 298 K) spectrum of ligand **L4** in DMSO-d_6.

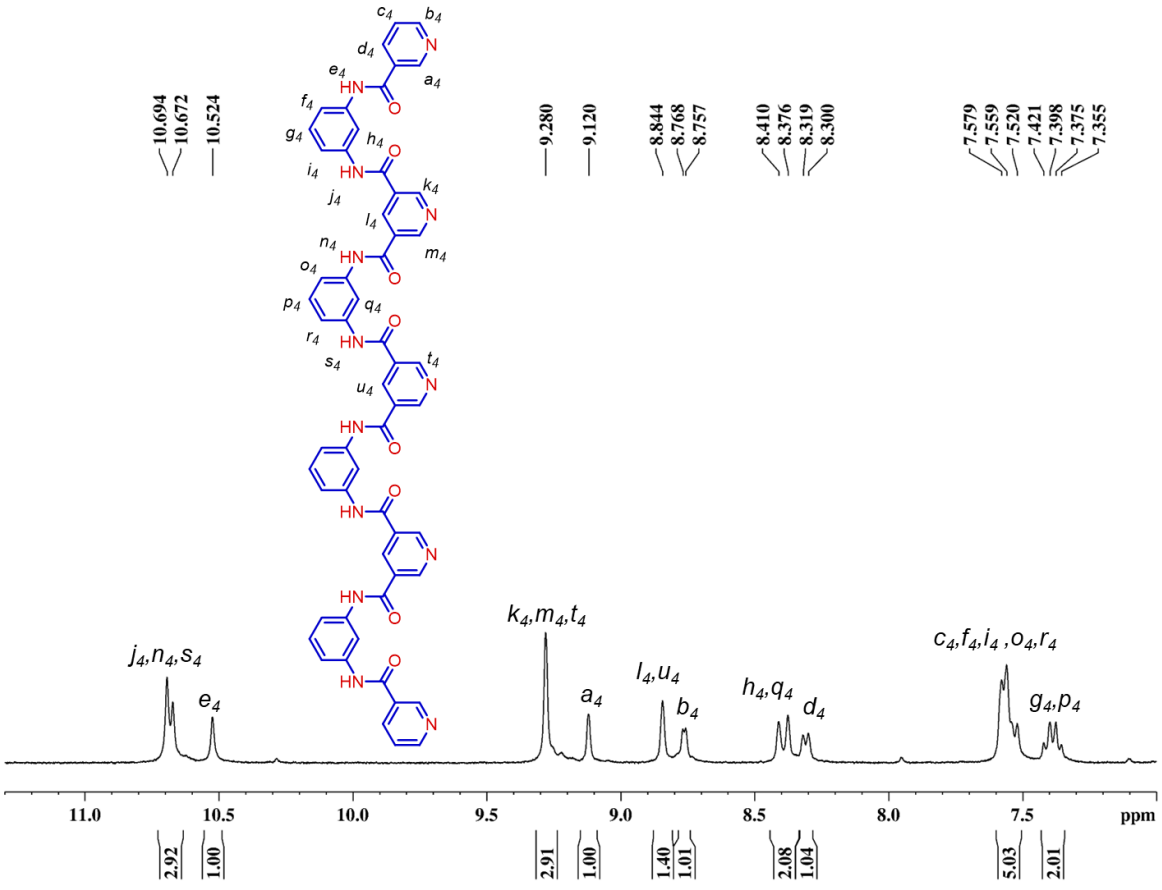

Figure S17a. [1]H NMR (500 MHz, 298 K) expansion spectrum of ligand **L4** in DMSO-d_6.

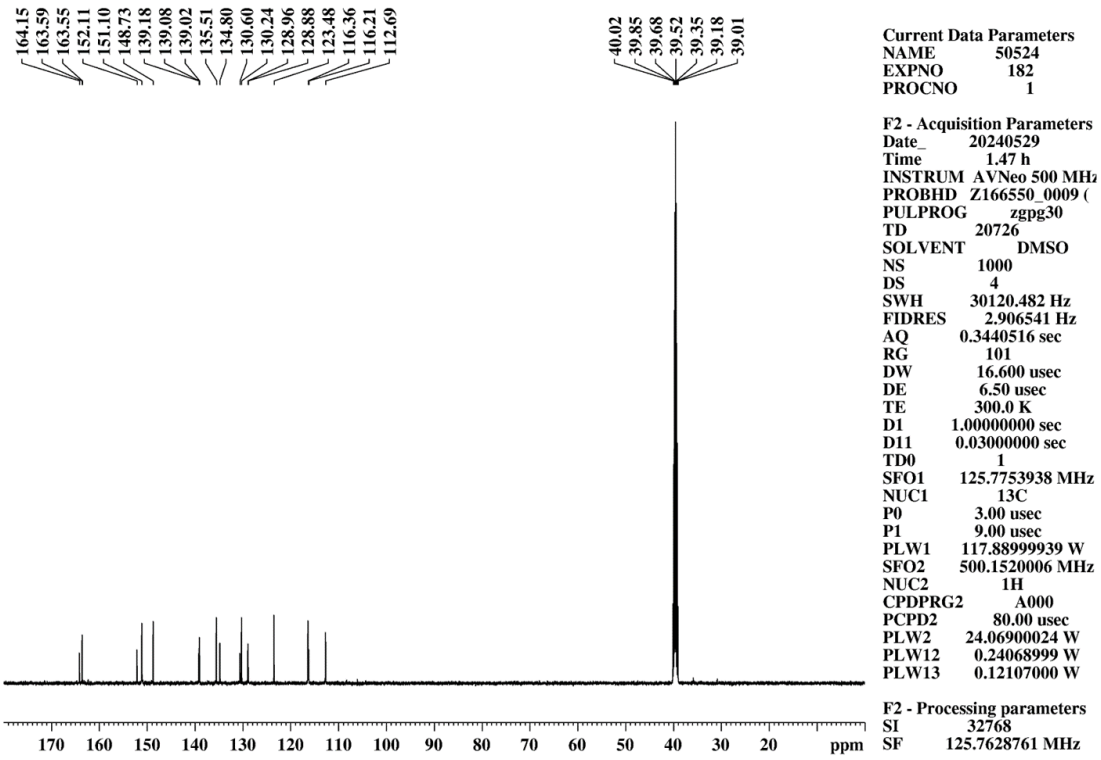

Figure S18. ^{13}C NMR (125 MHz, 298 K) spectrum of ligand **L4** in DMSO-d_6.

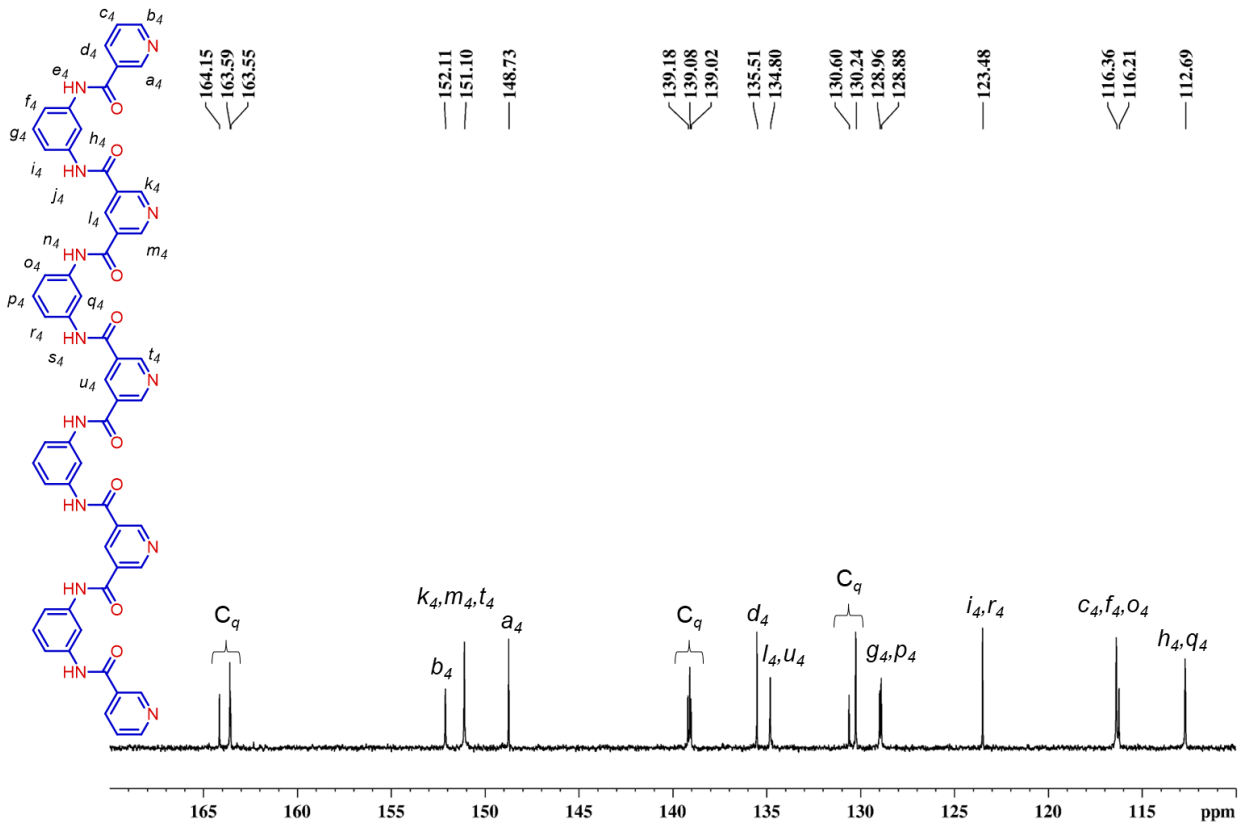

Figure S18a. ^{13}C NMR (125 MHz, 298 K) expansion spectrum of ligand **L4** in DMSO-d_6.

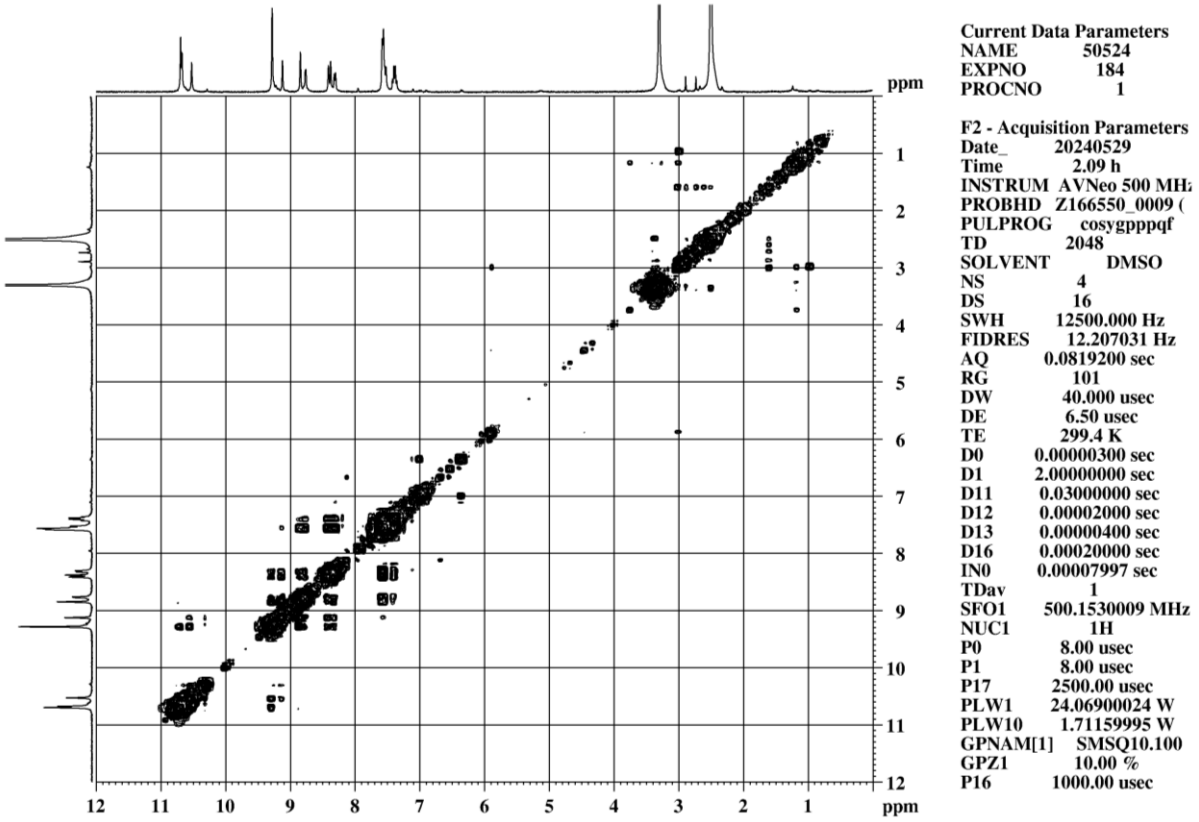

Figure S19. H-H COSY (500 MHz, 298 K) spectrum of ligand **L4** in DMSO-d_6.

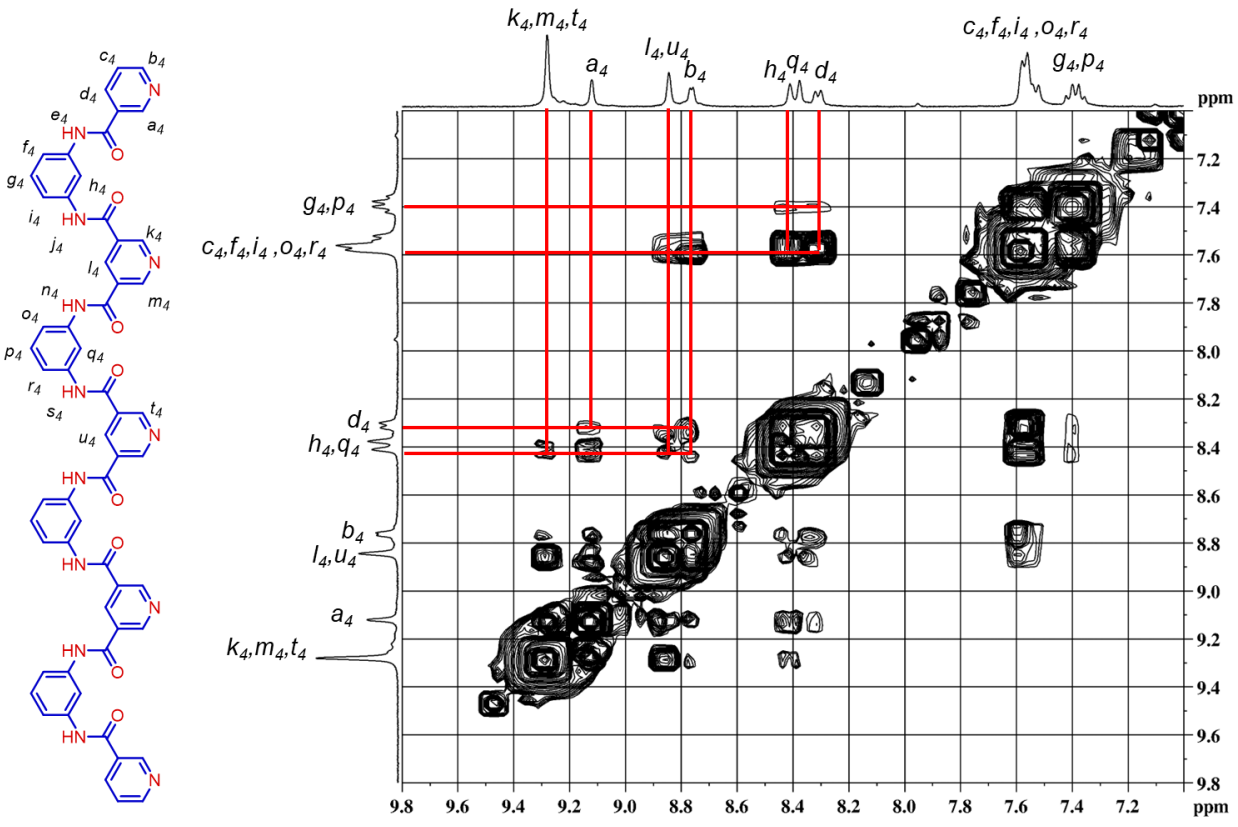

Figure S19a. H-H COSY (500 MHz, 298 K) expansion spectrum of ligand **L4** in DMSO-d_6.

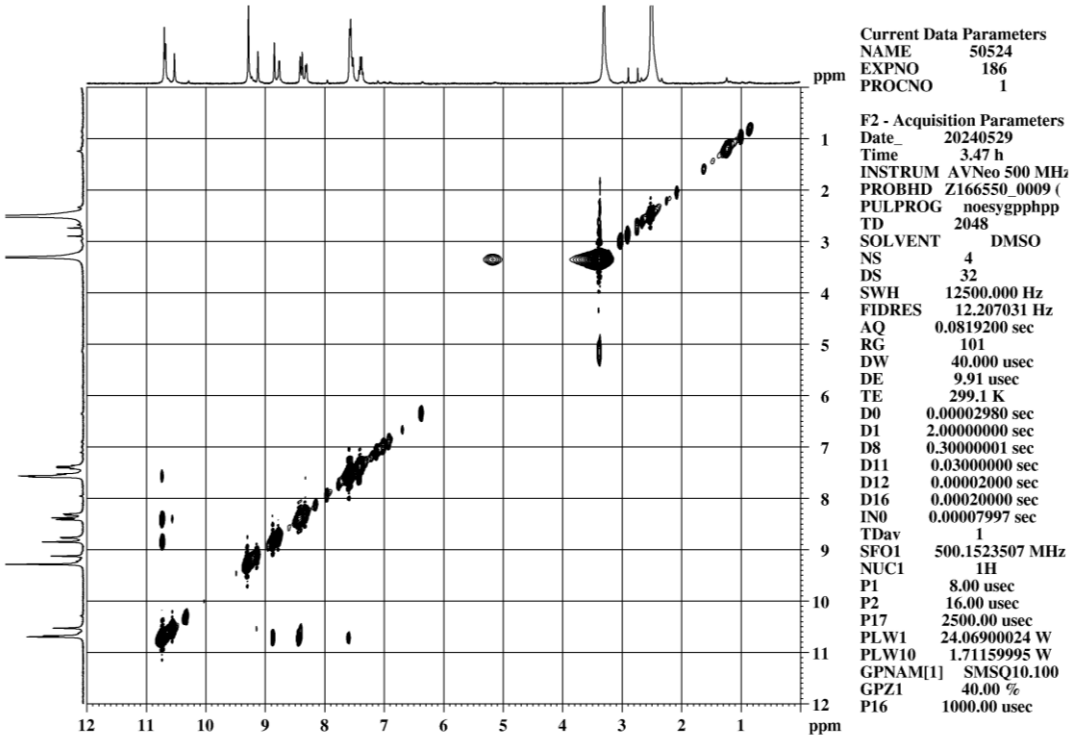

Figure S20. H-H NOESY (500 MHz, 298 K) spectrum of ligand **L4** in DMSO-d_6.

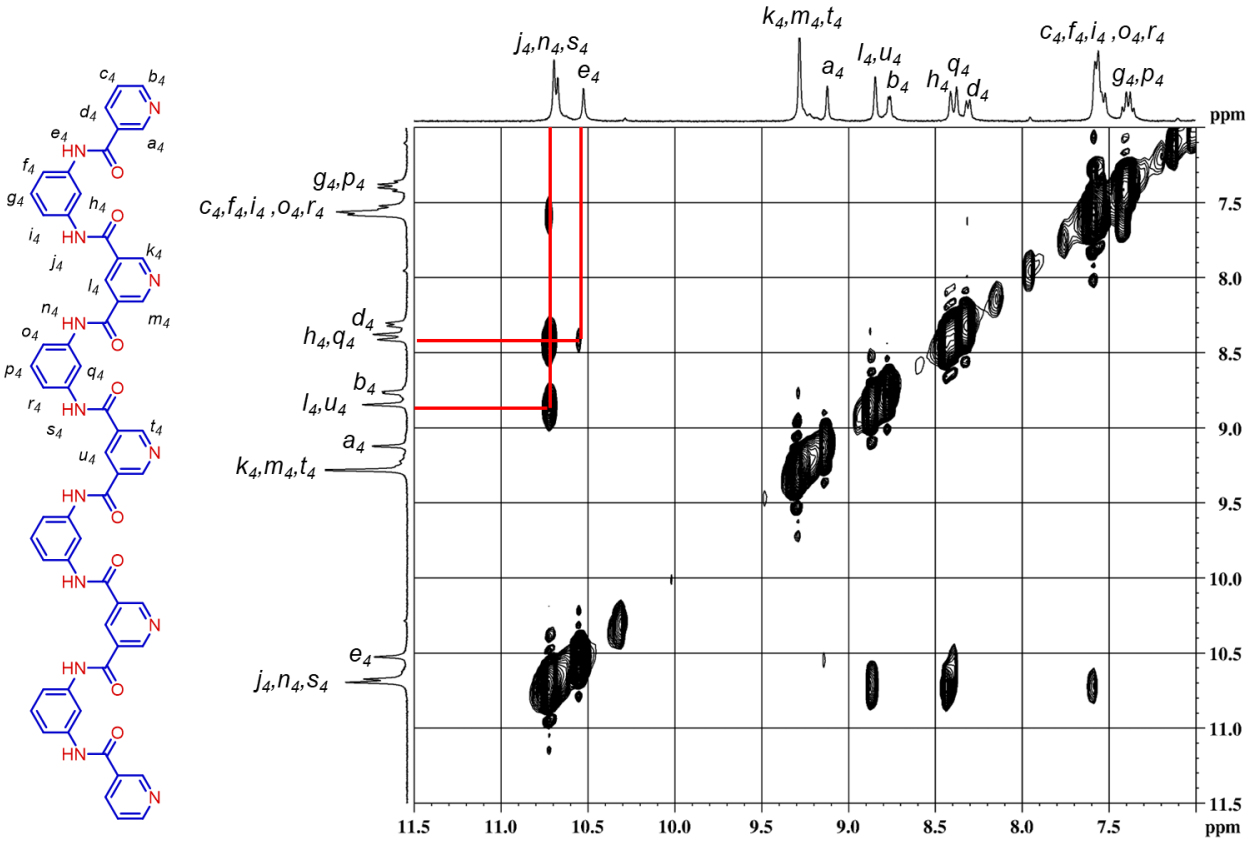

Figure S20a. H-H NOESY (500 MHz, 298 K) expansion spectrum of ligand **L3** in DMSO-d_6.

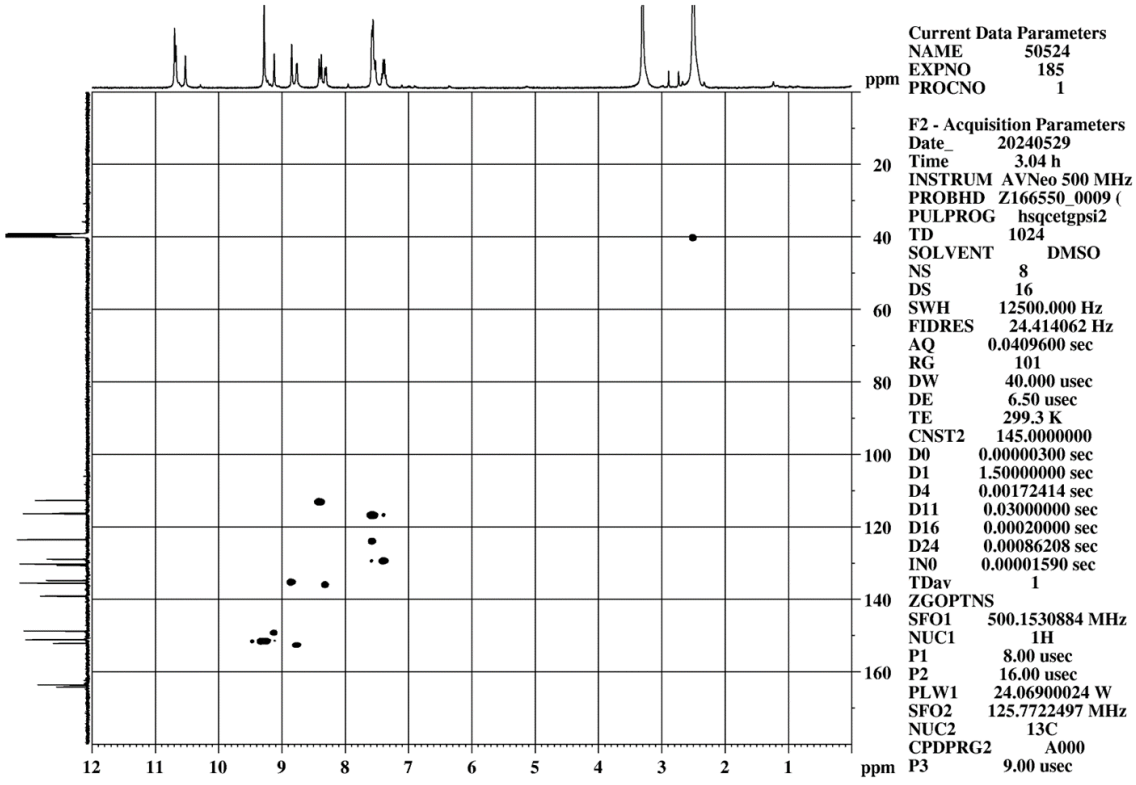

Figure S21. C-H COSY (500/125 MHz, 298 K) spectrum of ligand **L4** in DMSO-d_6.

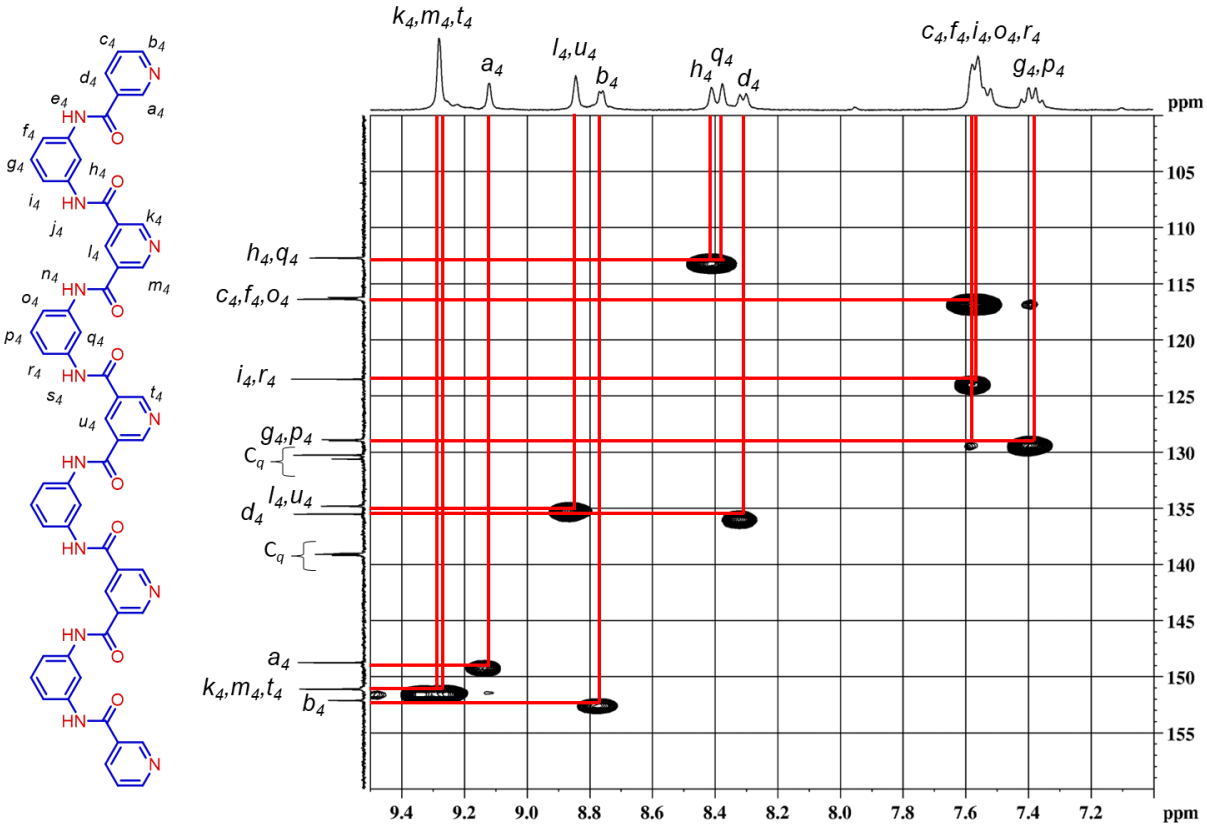

Figure S21a. C-H COSY (500/125 MHz, 298 K) expansion spectrum of ligand **L4** in DMSO-d_6.

S. ESI-MS Characterisation of the ligands and the precursors

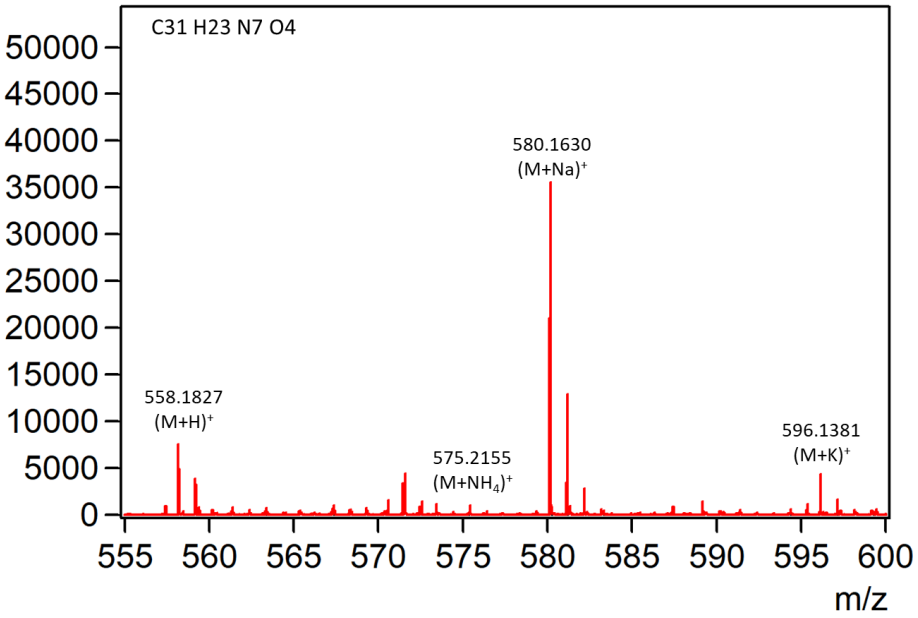

Figure S22. HRMS for the ligand **L2**.

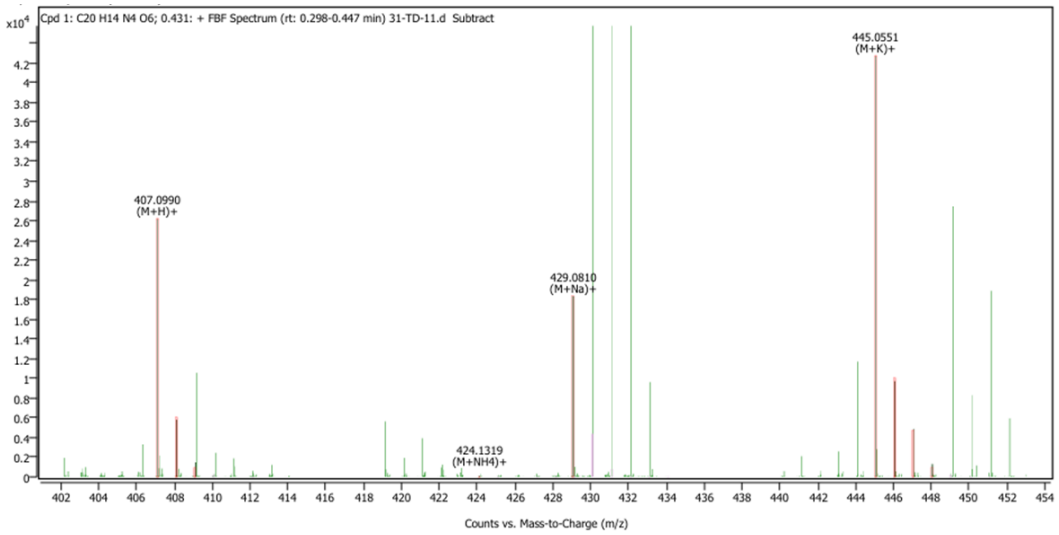

Figure S23. HRMS for the fragment **C**.

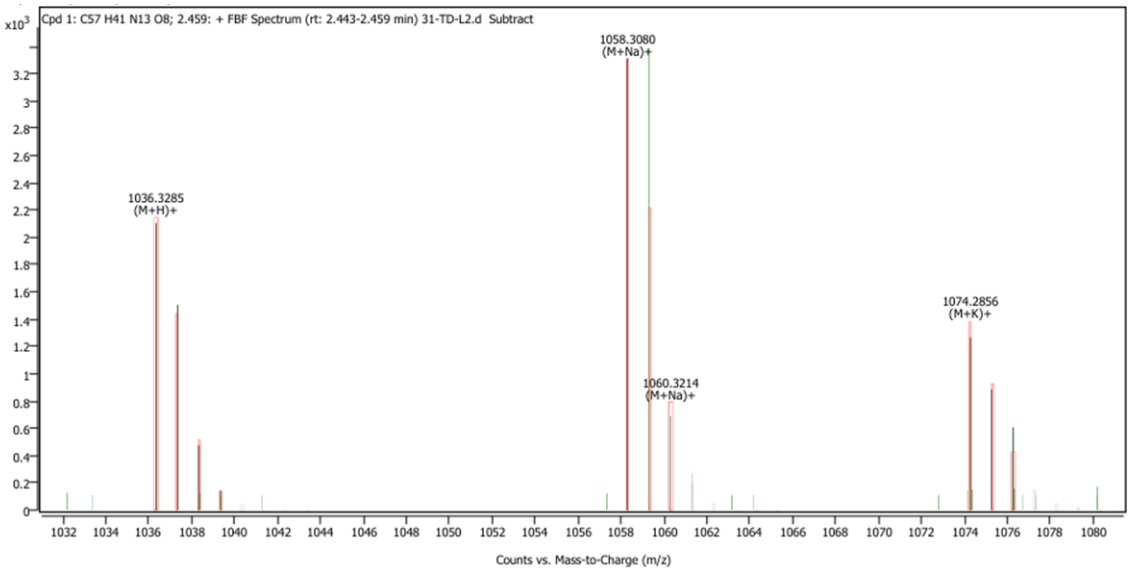

Figure S24. HRMS for the ligand **L3**.

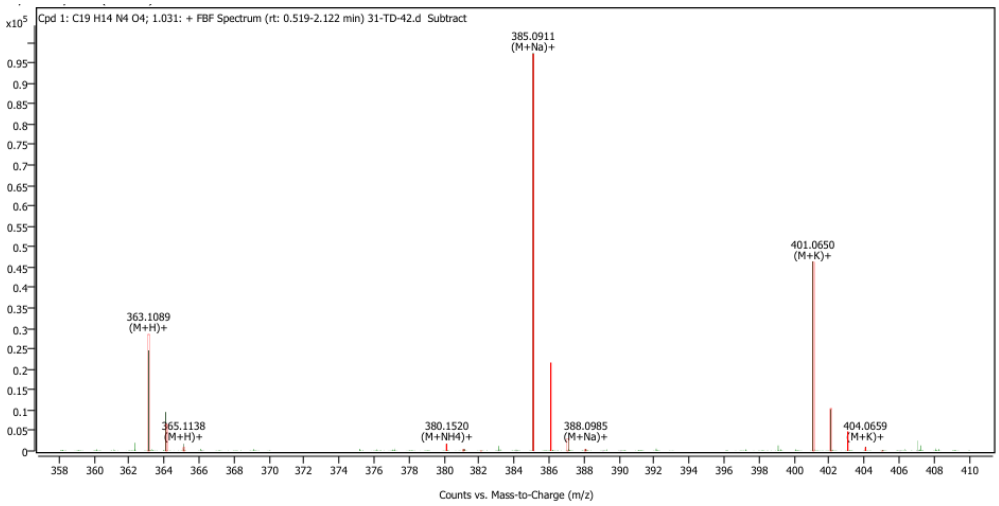

Figure S25. HRMS for the fragment **D**.

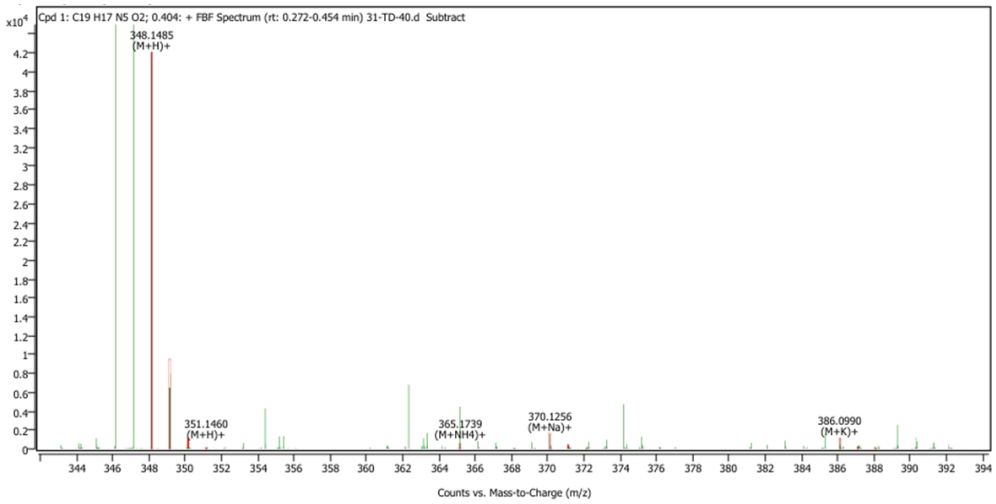

Figure S26. HRMS for the fragment **E**.

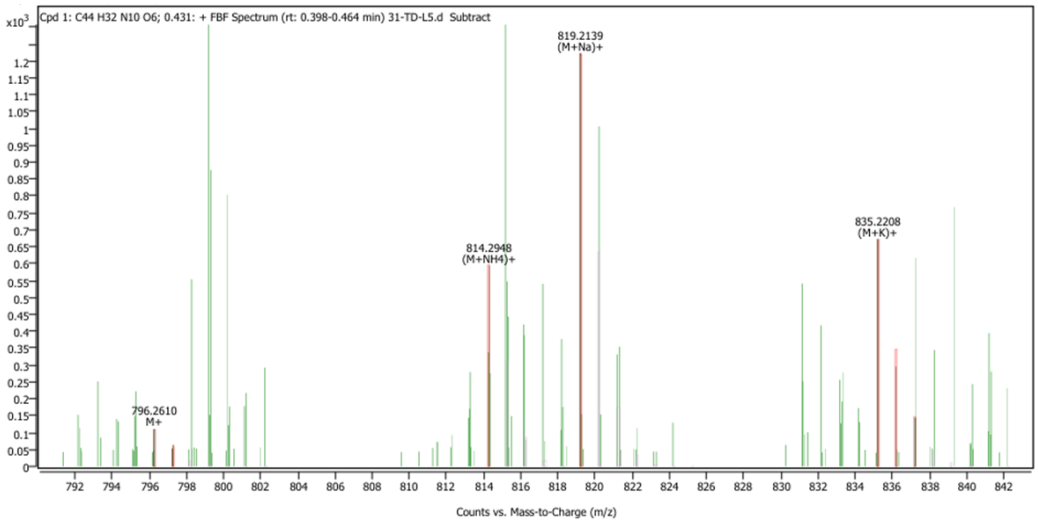

Figure S27. HRMS for the ligand **L4**.

S3. Synthesis and their characterisation of complexes

Synthesis of the complex $[(NO_3)_{2x}\subset Pd_3(L2)_4](NO_3)_{6-2x}$, $2\cdot 6NO_3$

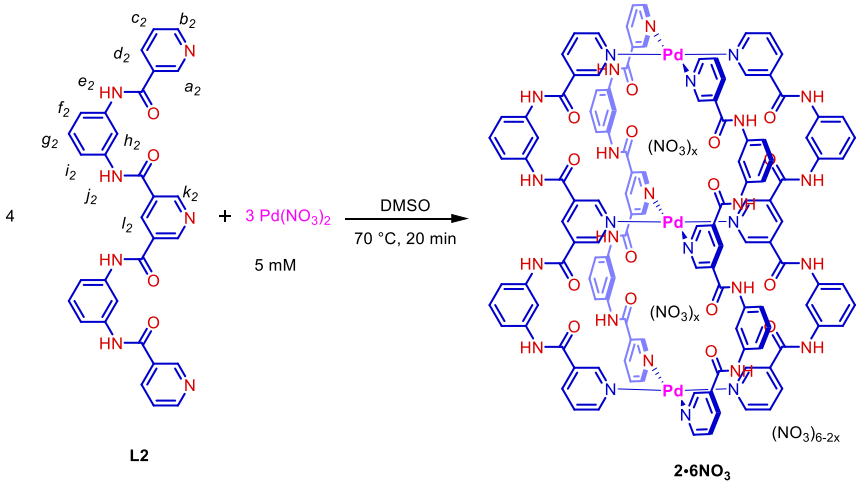

Scheme S4. Synthesis of complex **2·6NO₃**.

A solution of $Pd(NO_3)_2$ was prepared in 0.5 mL of DMSO-d_6 by stirring a mixture of $PdCl_2$ (0.44 mg, 0.005 mmol) and $AgNO_3$ (0.85 mg, 0.010 mmol) at 70 °C for 30 min. The precipitated AgCl was separated by centrifugation. The ligands **L2** (1.8 mg, 0.006 mmol) were added the supernatant and heated at 70 °C for 20 min to yield $[(NO_3)_{2x}\subset Pd_3(\mathbf{L2})_4](NO_3)_{6-2x}$, **2·6NO₃**.

^{1}H NMR (500 MHz, DMSO-d_6, 298 K): δ (ppm) 10.86 (s, 2H, H_{j2}), 10.68 (s, 2H, H_{e2}), 10.39 (s, 2H, H_{k2}), 10.15 (s, 2H, H_{a2}), 9.52 (d, 2H, J = 5.5 Hz, H_{b2}), 9.36 (d, 2H, J = 5.5 Hz, H_{l2}), 8.82 (s, 1H, H_{h2}), 8.65 (d, 2H, J = 8 Hz, H_{d2}), 7.92 (m, 4H, H_{c2}), 7.67 (dd, 2H, J_1 = 8 Hz, H_{i2}), 7.61 (dd, 2H, J_1 = 8 Hz, H_{f2}), 7.38 (t, 2H, J = 8.1 Hz, H_{g2}).

ESI-MS (ESI, DMSO): *m/z* Calc. for $[\mathbf{2\cdot 4NO_3}]^{2+}$ 1398.1966, found 1398.1945; Calc. for $[\mathbf{2\cdot 3NO_3}]^{3+}$ 911.4689, found 911.4675 and Calc. for $[\mathbf{2\cdot 2NO_3}]^{4+}$ 668.1046, found 668.1032.

Synthesis of the complex $[(NO_3)_{3x}\subset Pd_4(L3)_4](NO_3)_{8-3x}$, $3\cdot 8NO_3$

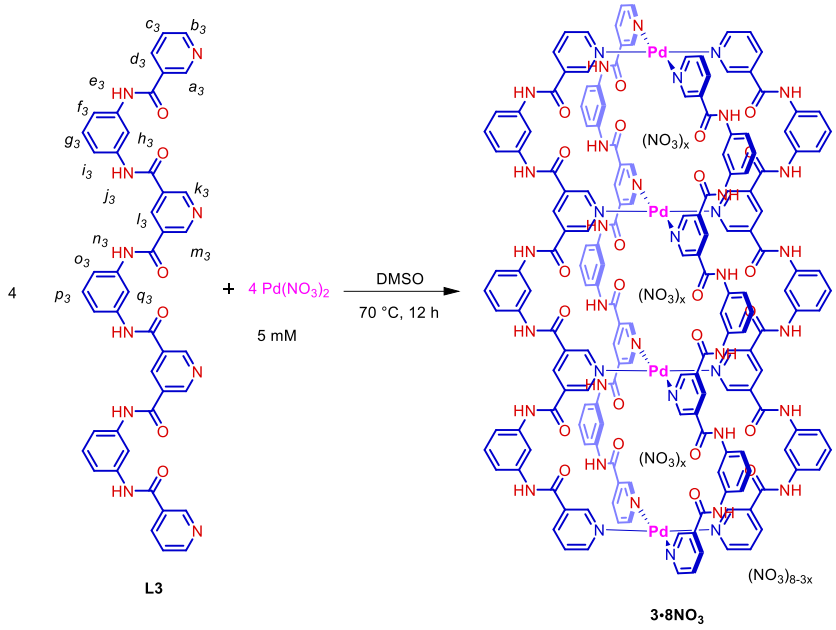

Scheme S5. Synthesis of complex $\mathbf{3\cdot 8NO_3}$.

A solution of $Pd(NO_3)_2$ was prepared in 0.5 mL of DMSO-d_6 by stirring a mixture of $PdCl_2$ (0.44 mg, 0.005 mmol) and $AgNO_3$ (0.85 mg, 0.010 mmol) at 70 °C for 30 min. The precipitated AgCl was separated by centrifugation. The ligands **L3** (1.99 mg, 0.005 mmol) were added the supernatant and heated at 70 °C for 12 h to yield $[(NO_3)_{3x}\subset Pd_4(\mathbf{L3})_4](NO_3)_{8-3x}$, $\mathbf{3\cdot 8NO_3}$.

^{1}H NMR (500 MHz, DMSO-d_6, 298 K): δ (ppm) 10.89 (s, 4H, H_{j3}, H_{n3}), 10.70 (s, 2H, H_{e3}), 10.42 (m, 4H, H_{k3}, H_{m3}), 10.17 (s, 2H, H_{a3}), 9.55 (s, 2H, H_{b3}), 9.40 (s, 2H, H_{l3}), 8.89 (s, 1H, H_{q3}), 8.84 (s, 2H, H_{l3}), 8.66 (s, 2H, H_{d3}), 7.93 (s, 2H, H_{c3}), 7.73 (s, 2H, H_{h3}), 7.70 (s, 2H, H_{o3}), 7.62 (s, 2H, H_{f3}), 7.73 (s, 4H, H_{g3}, H_{p3}).

ESI-MS (ESI, DMSO): *m/z* Calc. for $[\mathbf{3\cdot 5NO_3}]^{3+}$ 1307.5219, found 1307.4874; Calc. for $[\mathbf{3\cdot 4NO_3}]^{4+}$ 965.1446, found 965.1223; Calc. for $[\mathbf{3\cdot 3NO_3}]^{5+}$ 759.7182, found 759.7011 and Calc. for $[\mathbf{3\cdot 2NO_3}]^{6+}$ 622.7673, found 622.7536.

Synthesis of the complex $[(NO_3)_{4x}\subset Pd_5(L4)_4](NO_3)_{10-4x}$, $4\cdot10NO_3$

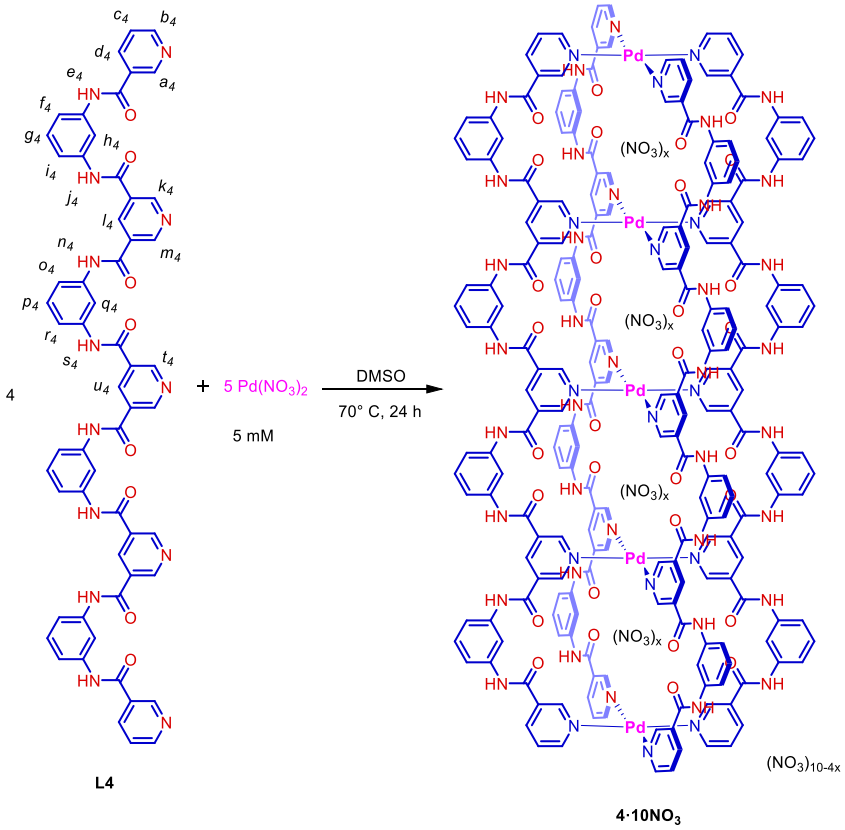

Scheme S6. Synthesis of complex **4·10NO₃**.

A solution of $Pd(NO_3)_2$ was prepared in 0.5 mL of DMSO-d_6 by stirring a mixture of $PdCl_2$ (0.44 mg, 0.005 mmol) and $AgNO_3$ (0.85 mg, 0.010 mmol) at 70 °C for 30 min. The precipitated AgCl was separated by centrifugation. The ligands **L4** (2.07 mg, 0.004 mmol) were added the supernatant and heated at 70 °C for 24 h to yield $[(NO_3)_{4x}\subset Pd_5(\mathbf{L4})_4](NO_3)_{10-4x}$, **4·10NO₃**.

^{1}H NMR (500 MHz, DMSO-d_6, 298 K): δ (ppm) 10.92 (bs, 6H, H_{j4}, H_{n4}, H_4), 10.70 (s, 2H, H_{e4}), 10.44 (m, 6H, H_{k4}, H_{m4}, H_{t4}), 10.18 (s, 2H, H_{a4}), 9.54 (s, 2H, H_{b4}), 9.42 (m, 4H, H_{l4}, H_{u4}), 8.92 (s, 2H, H_{q4}), 8.86 (s, 2H, H_{h4}), 8.67 (s, 2H, H_{d4}), 7.94 (s, 2H, H_{c4}), 7.73 (m, 6H, H_{i4}, H_{o4}, H_{r4}), 7.63 (s, 2H, H_{f4}) , 7.42 (m, 4H, H_{g4}, H_{p4}).

ESI-MS (ESI, DMSO): *m/z* Calc. for $[\mathbf{4\cdot6NO_3}]^{4+}$ 1261.9344, found 1261.9052; Calc. for $[\mathbf{4\cdot5NO_3}]^{5+}$ 997.1501, found 997.1277; Calc. for $[\mathbf{4\cdot4NO_3}]^{6+}$ 820.6275, found 820.6101 and Calc. for $[\mathbf{4\cdot3NO_3}]^{7+}$ 694.5394, found 694.5270.

Characterisation of complexes

Characterisation of complex 2·6NO$_3$

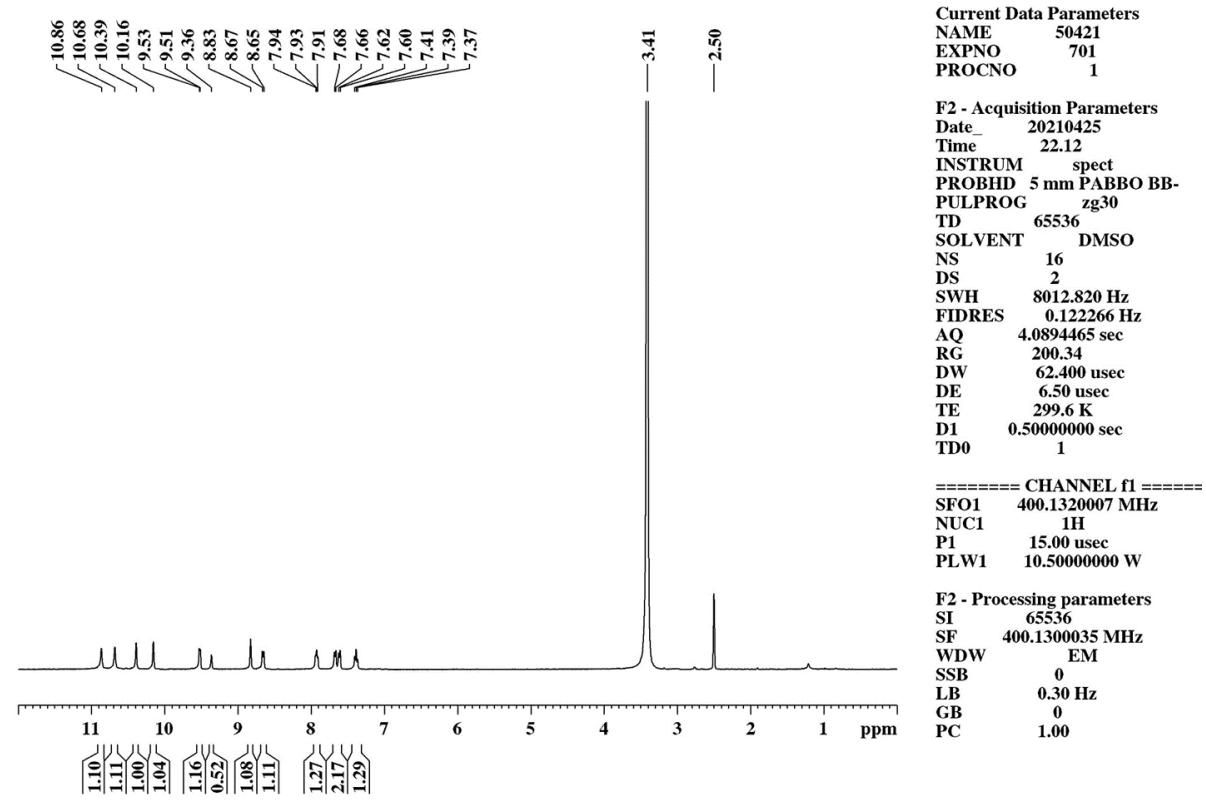

Figure S28. [1]H NMR (500 MHz, 298 K) spectrum of complex, **2·6NO$_3$** in DMSO-d_6.

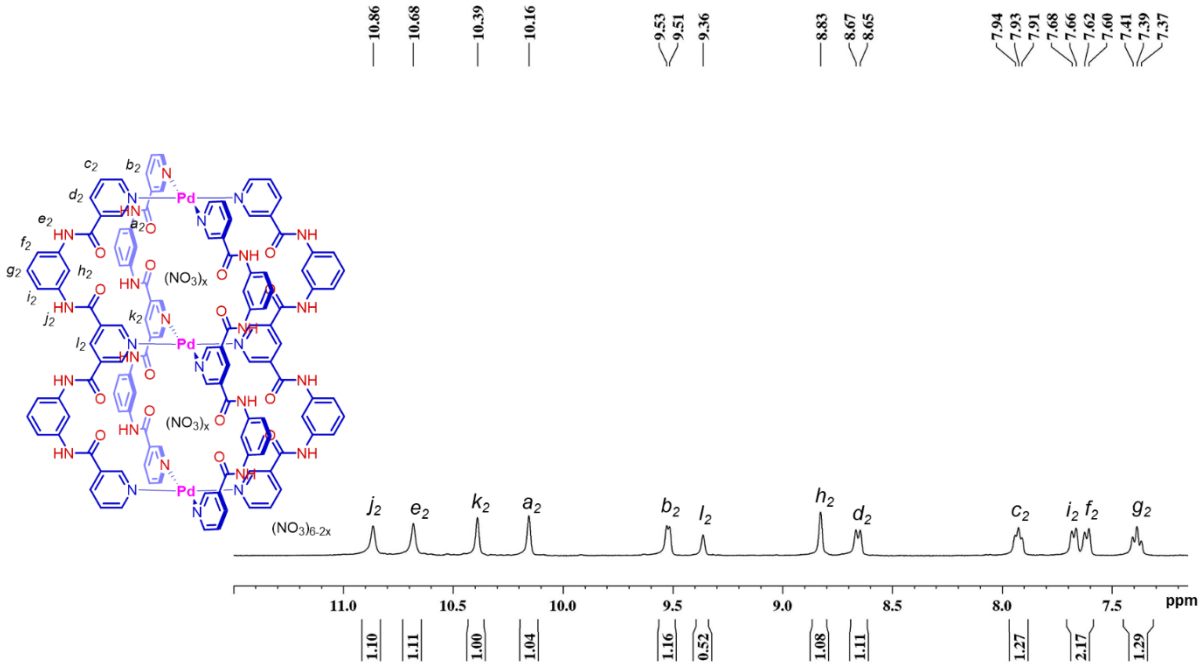

Figure S28a. [1]H NMR (500 MHz, 298 K) expansion spectrum of complex, **2·6NO$_3$** in DMSO-d_6.

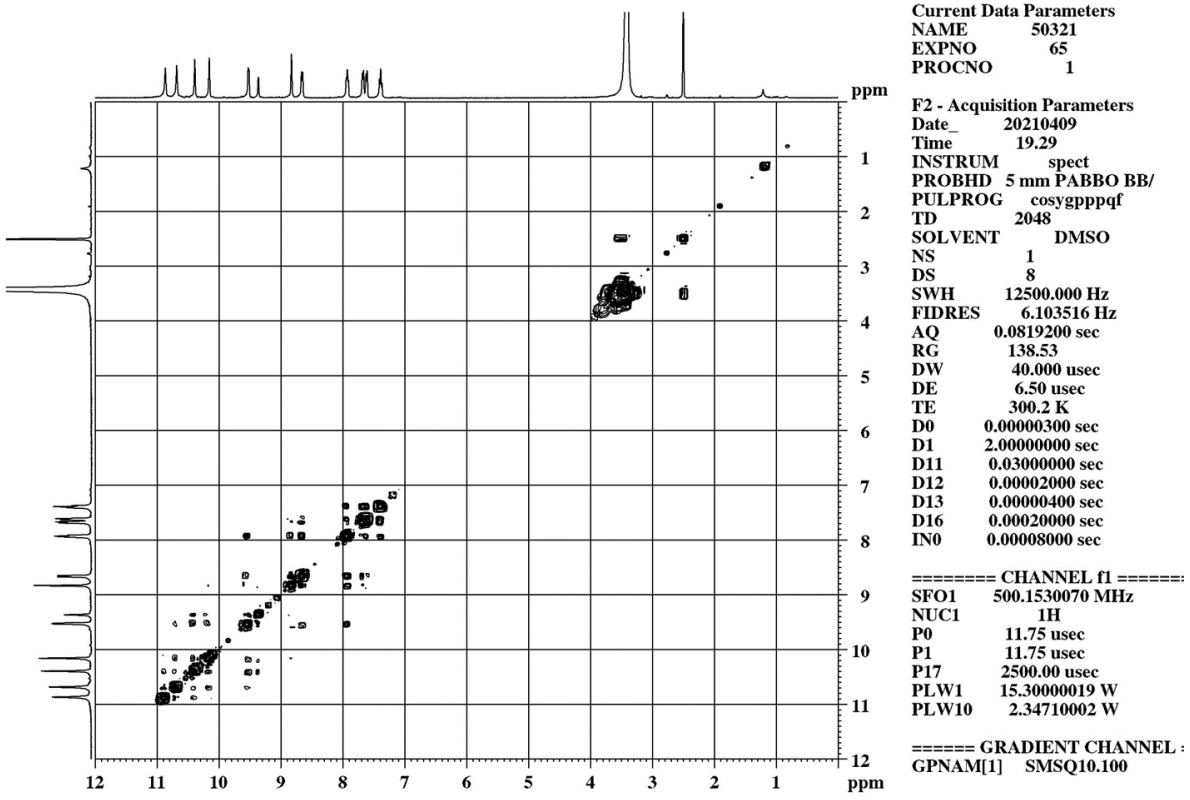

Figure S29. H-H COSY (500 MHz, 298 K) spectrum of complex, **2·6NO₃** in DMSO-d_6.

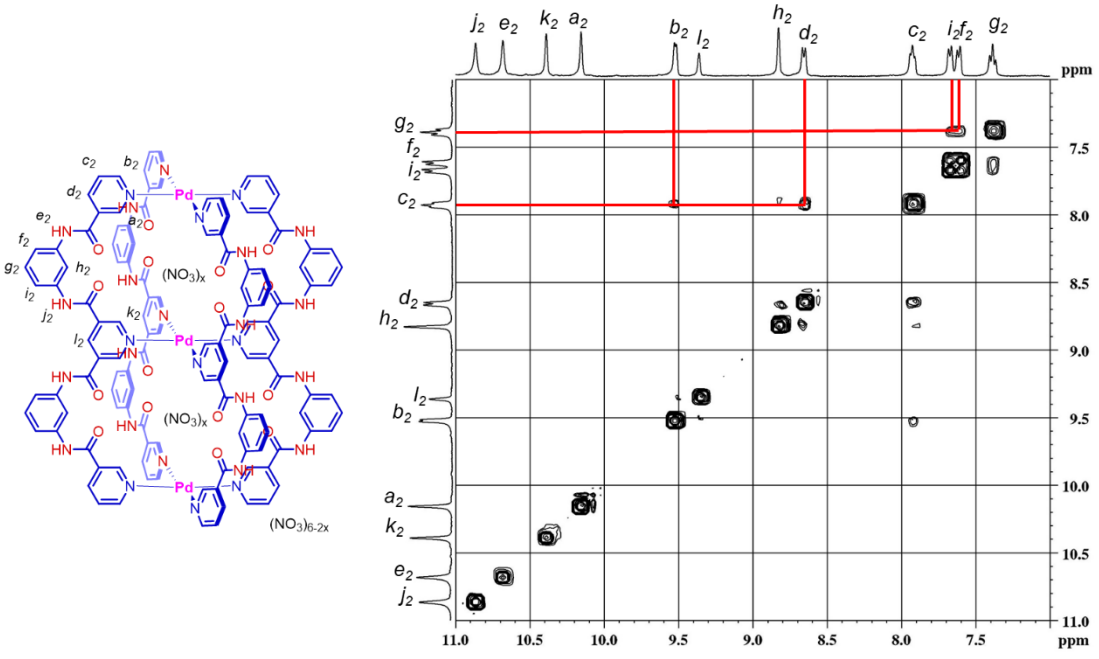

Figure S29a. H-H COSY (500 MHz, 298 K) expansion spectrum of complex, **2·6NO₃** in DMSO-d_6.

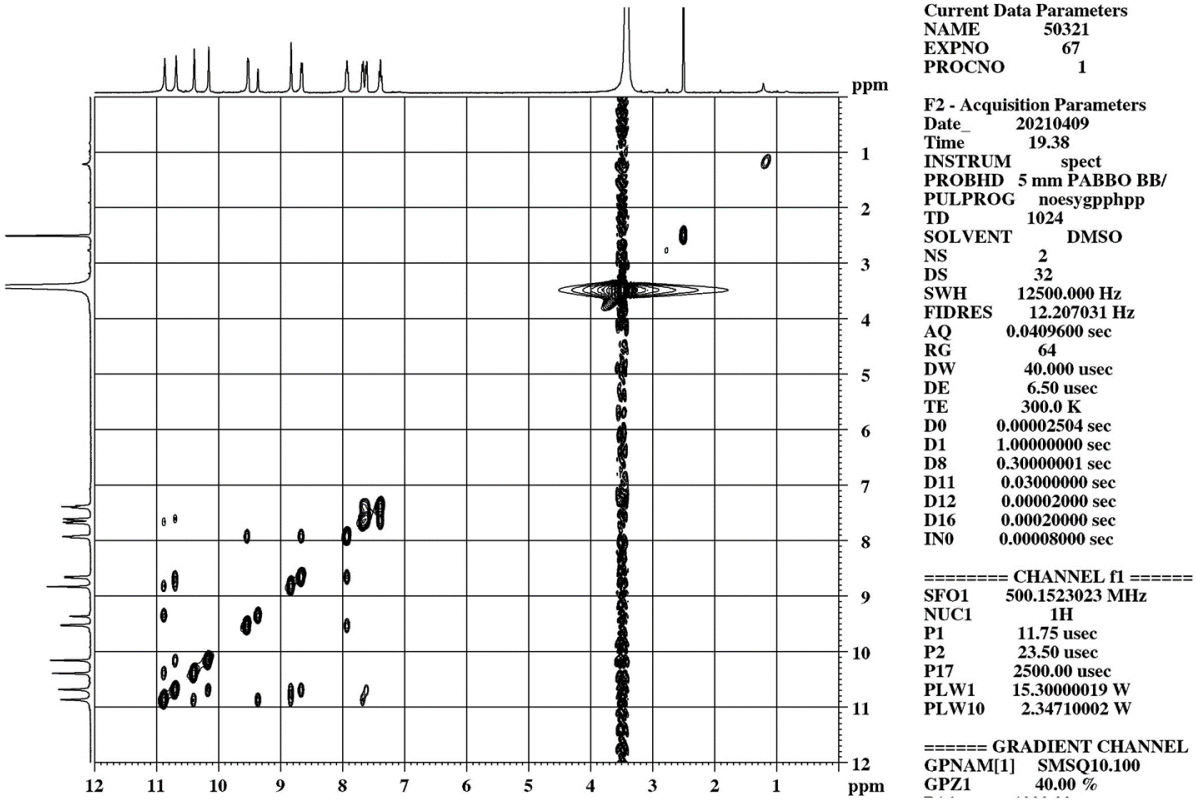

Figure S30. H-H NOESY (500 MHz, 298 K) spectrum of complex, **2·6NO$_3$** in DMSO-d_6.

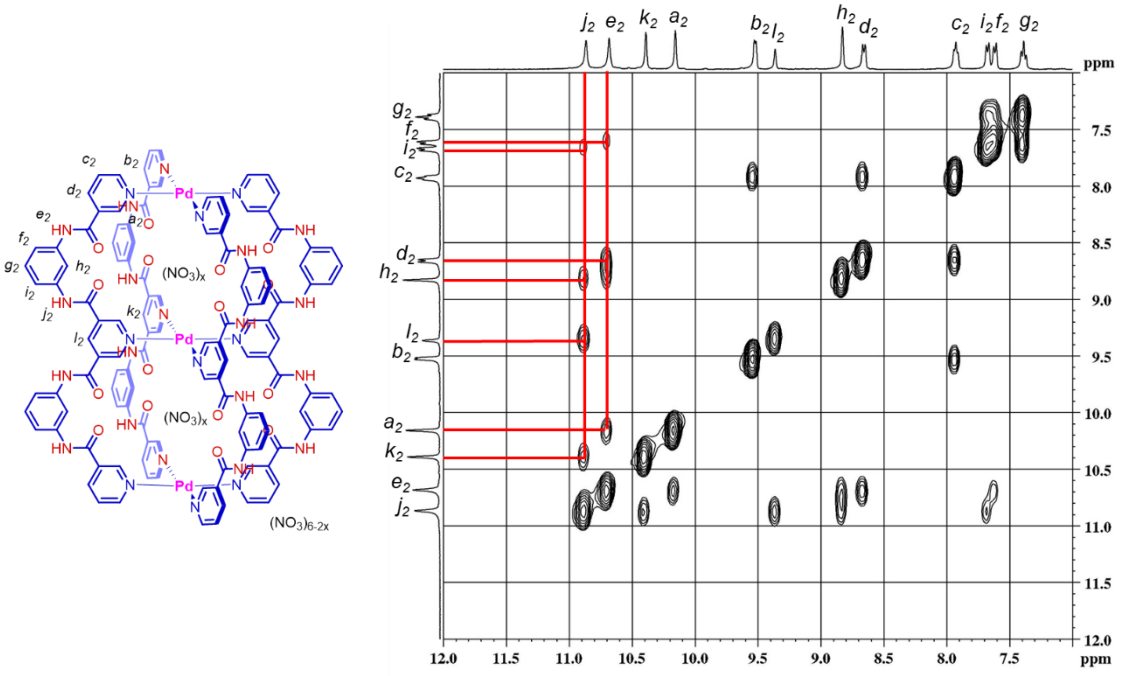

Figure S30a. H-H NOESY (500 MHz, 298 K) expansion spectrum of complex, **2·6NO$_3$** in DMSO-d_6.

Characterisation of complex 3·8NO$_3$

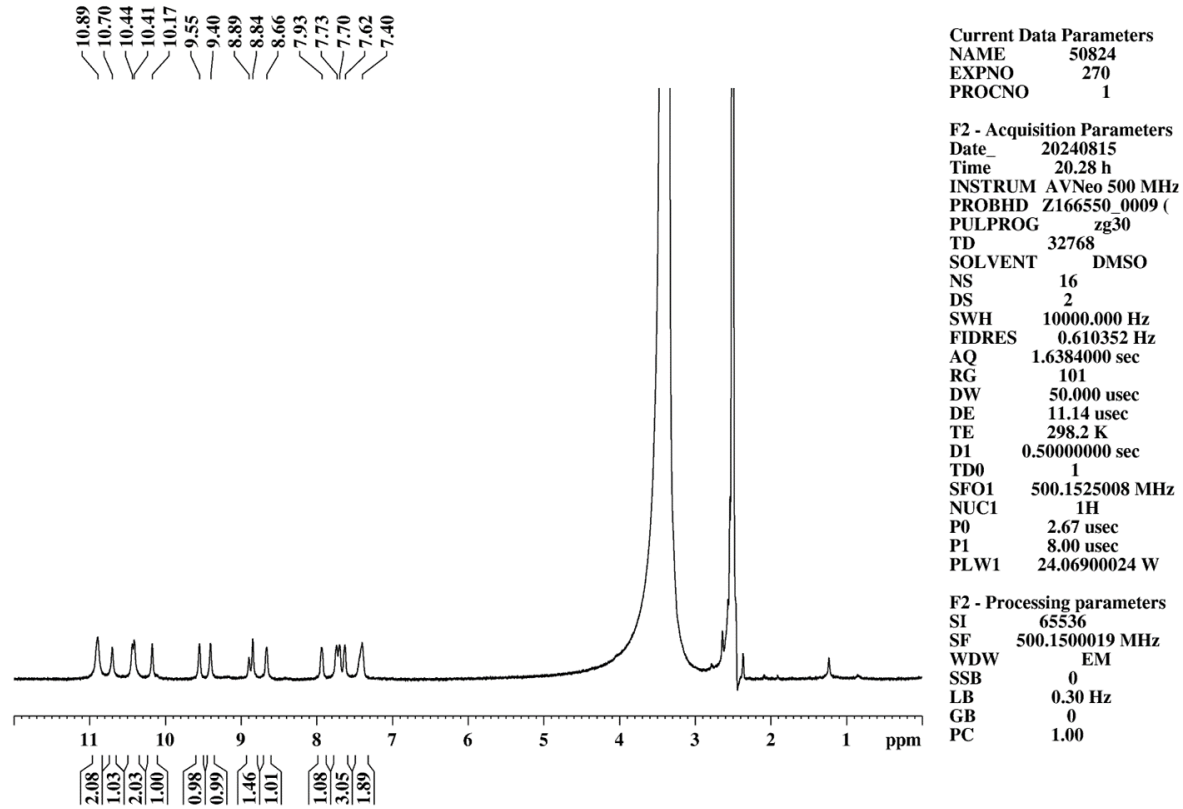

Figure S31. [1]H NMR (500 MHz, 298 K) spectrum of complex, **3·8NO$_3$** in DMSO-d_6.

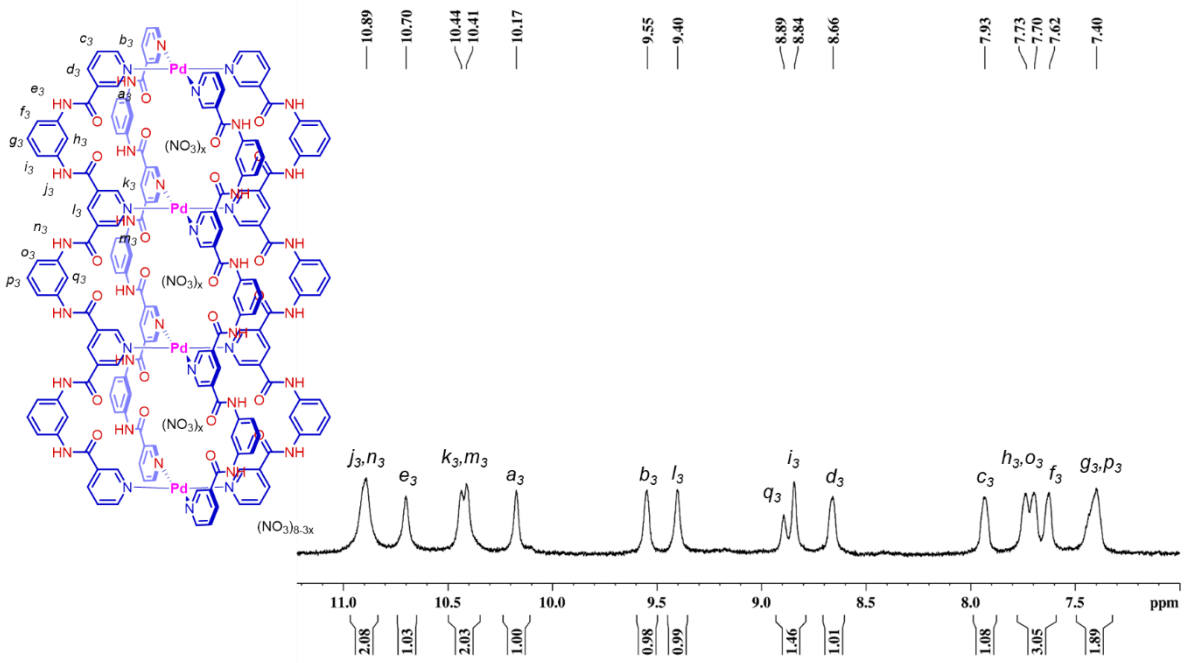

Figure S31a. [1]H NMR (500 MHz, 298 K) expansion spectrum of complex, **3·8NO$_3$** in DMSO-d_6.

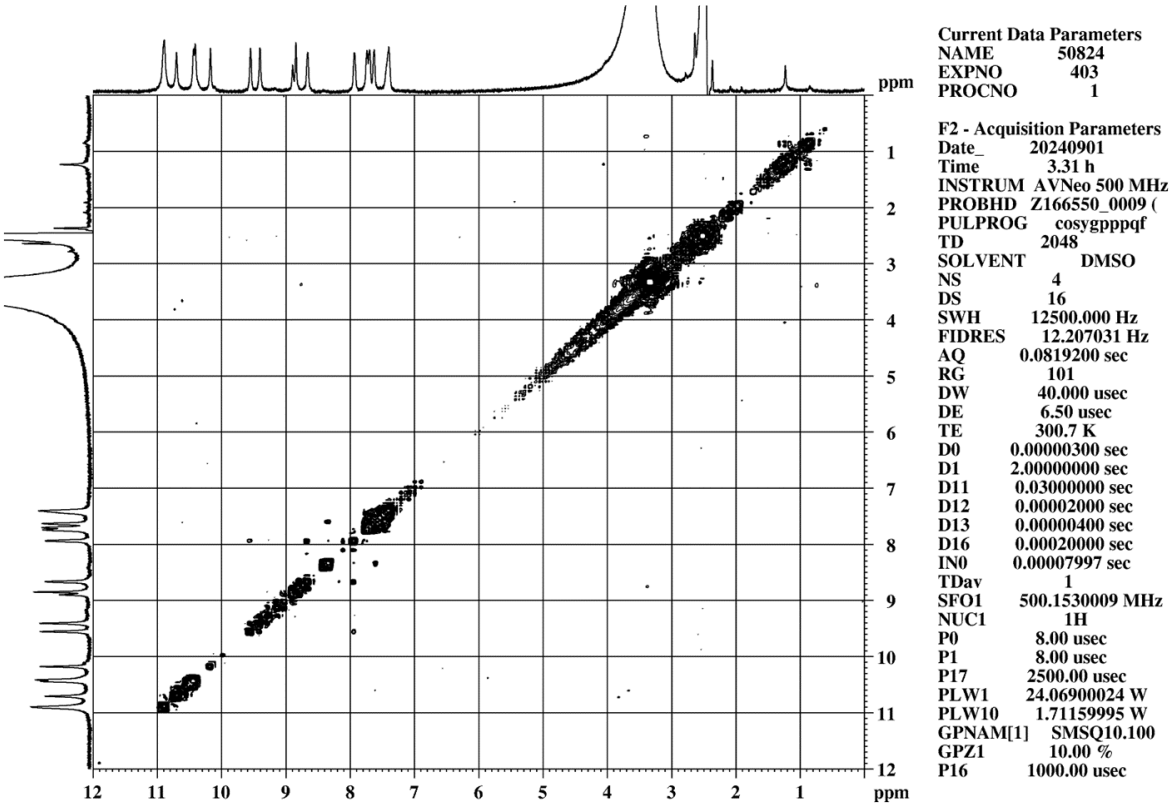

Figure S32. H-H COSY (500 MHz, 298 K) spectrum of complex, **3·8NO$_3$** in DMSO-d_6.

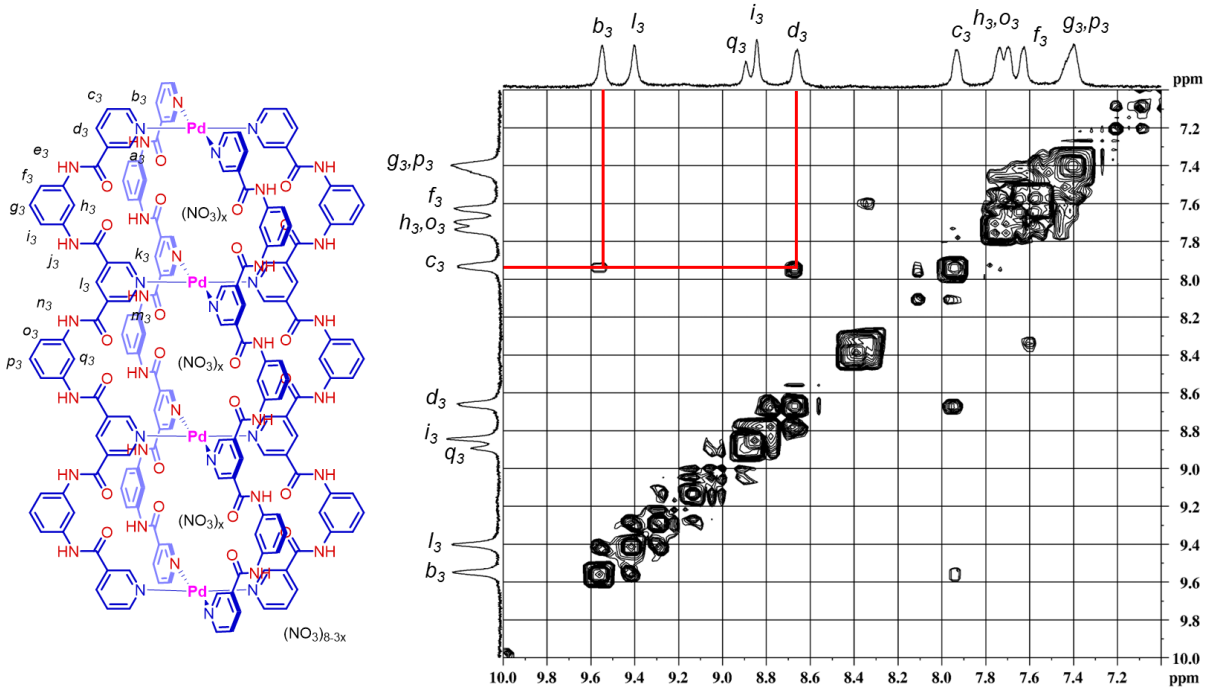

Figure S32a. H-H COSY (500 MHz, 298 K) expansion spectrum of complex, **3·8NO$_3$** in DMSO-d_6.

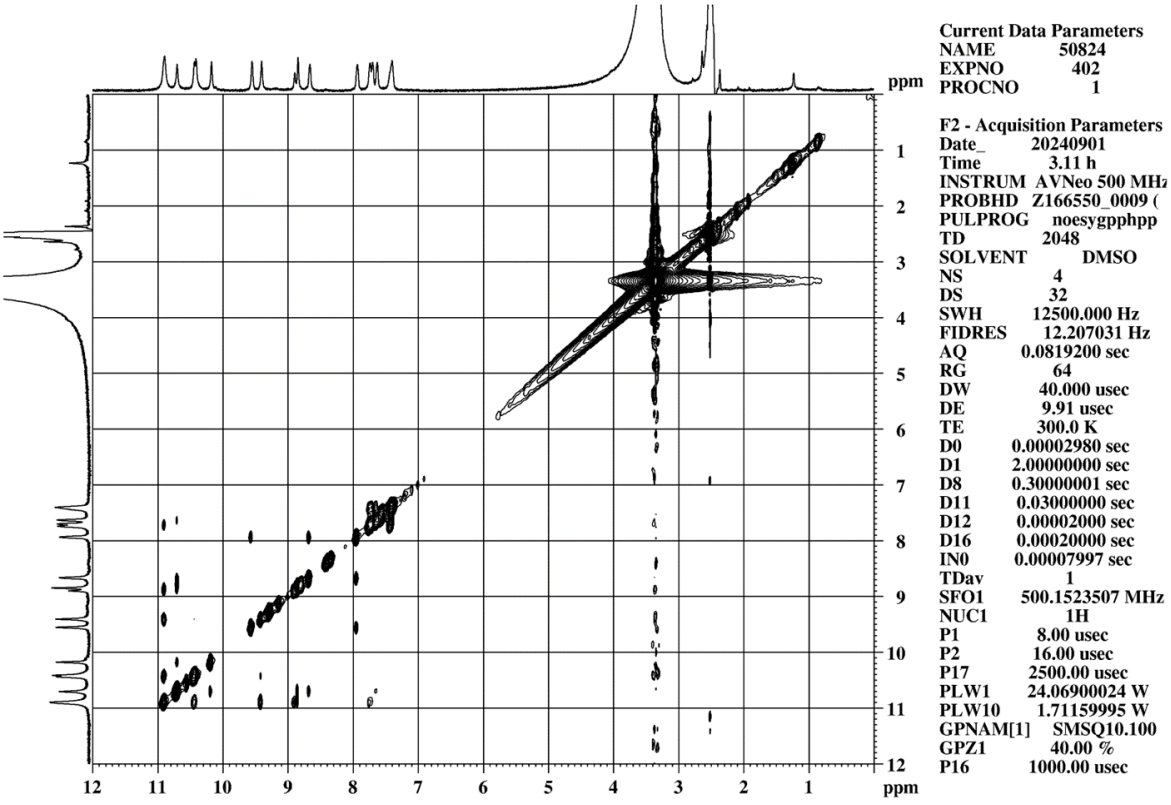

Figure S33. H-H NOESY (500 MHz, 298 K) spectrum of complex, **3·8NO$_3$** in DMSO-d_6.

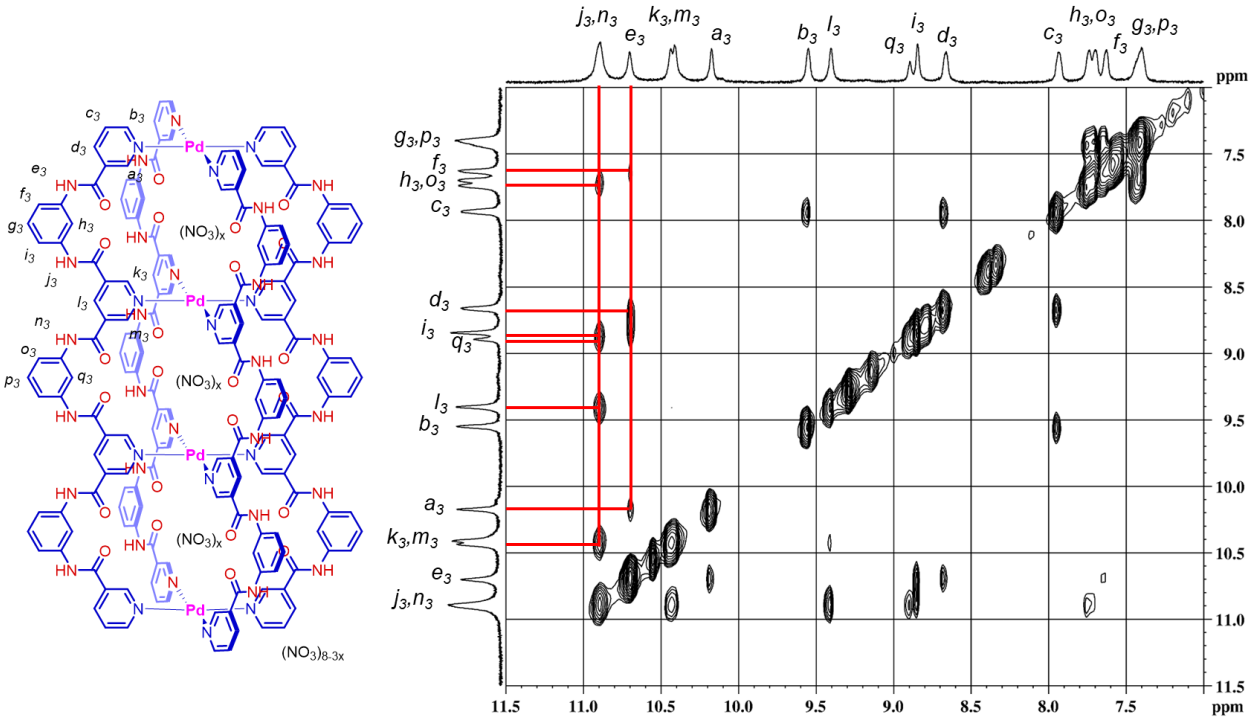

Figure S33a. H-H NOESY (500 MHz, 298 K) expansion spectrum of complex, **3·8NO$_3$** in DMSO-d_6.

.

Characterisation of complex **4·10NO$_3$**

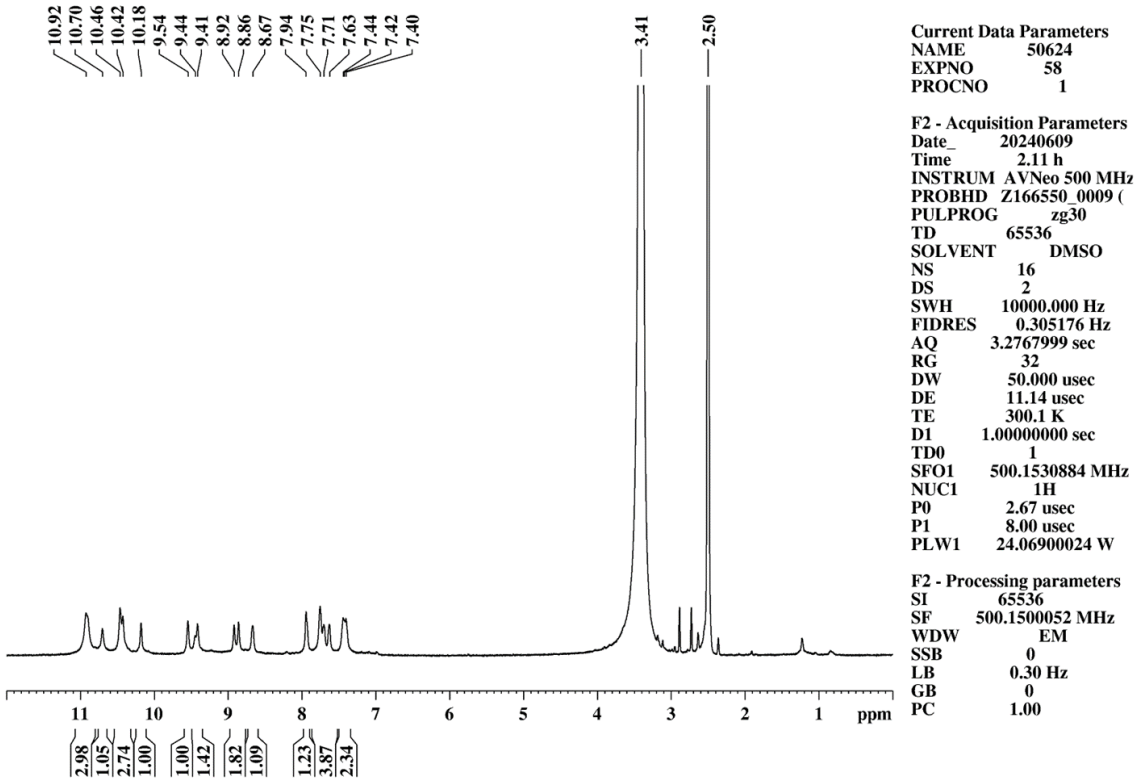

Figure S34. ^{1}H NMR (500 MHz, 298 K) spectrum of complex, **4·10NO$_3$** in DMSO-d_6.

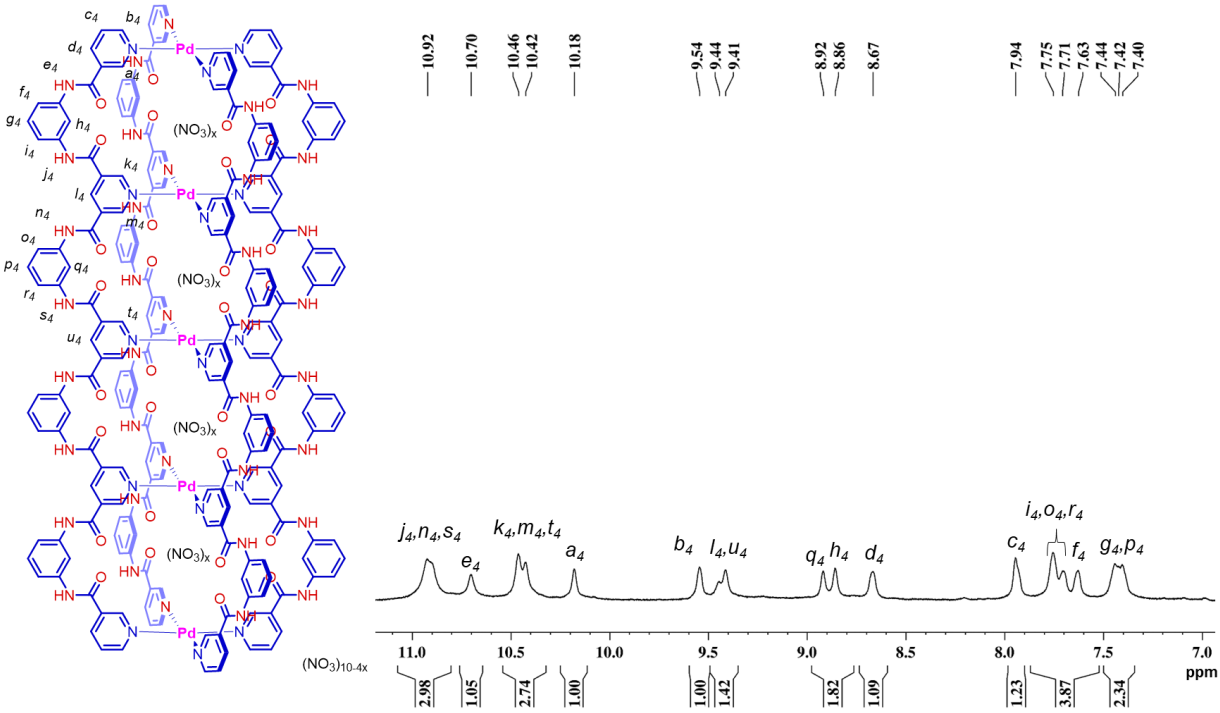

Figure S34a. ^{1}H NMR (500 MHz, 298 K) expansion spectrum of complex, **4·10NO$_3$** in DMSO-d_6.

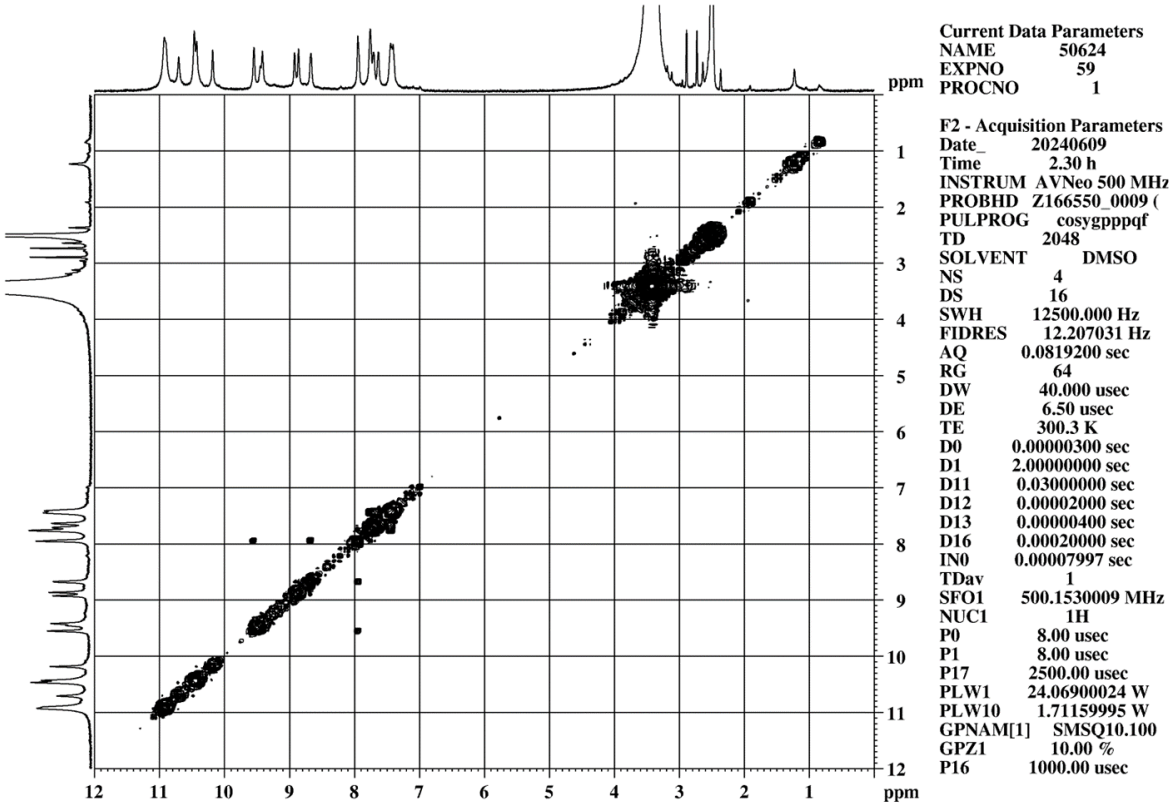

Figure S35. H-H COSY (500 MHz, 298 K) spectrum of complex, **4·10NO$_3$** in DMSO-d_6.

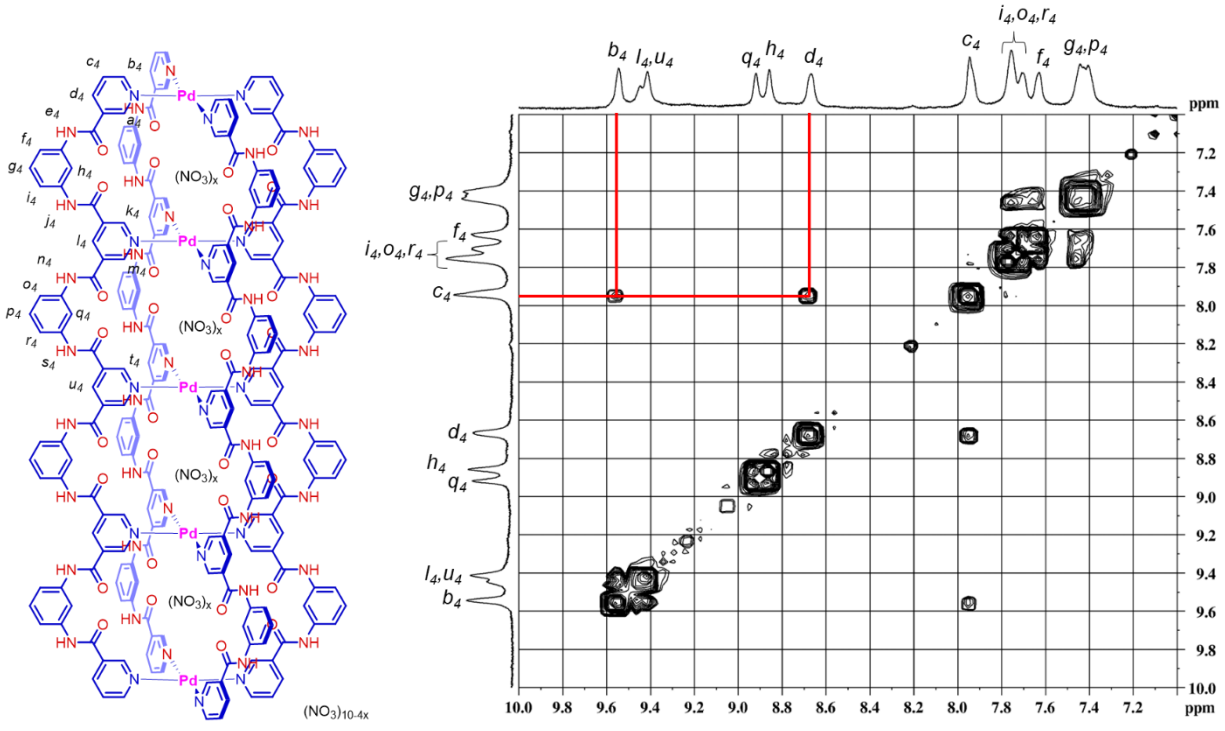

Figure S35a. H-H COSY (500 MHz, 298 K) expansion spectrum of complex, **4·10NO$_3$** in DMSO-d_6.

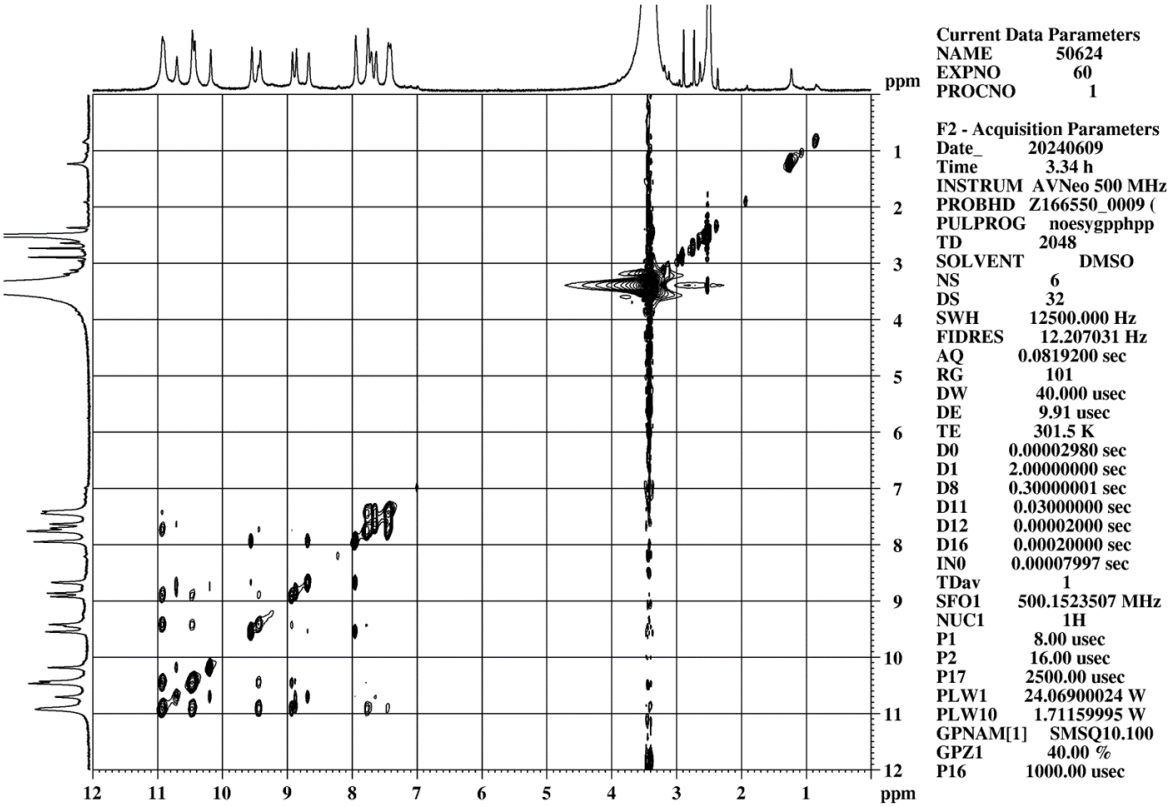

Figure S36. H-H NOESY (500 MHz, 298 K) spectrum of complin DMSO-d_6.

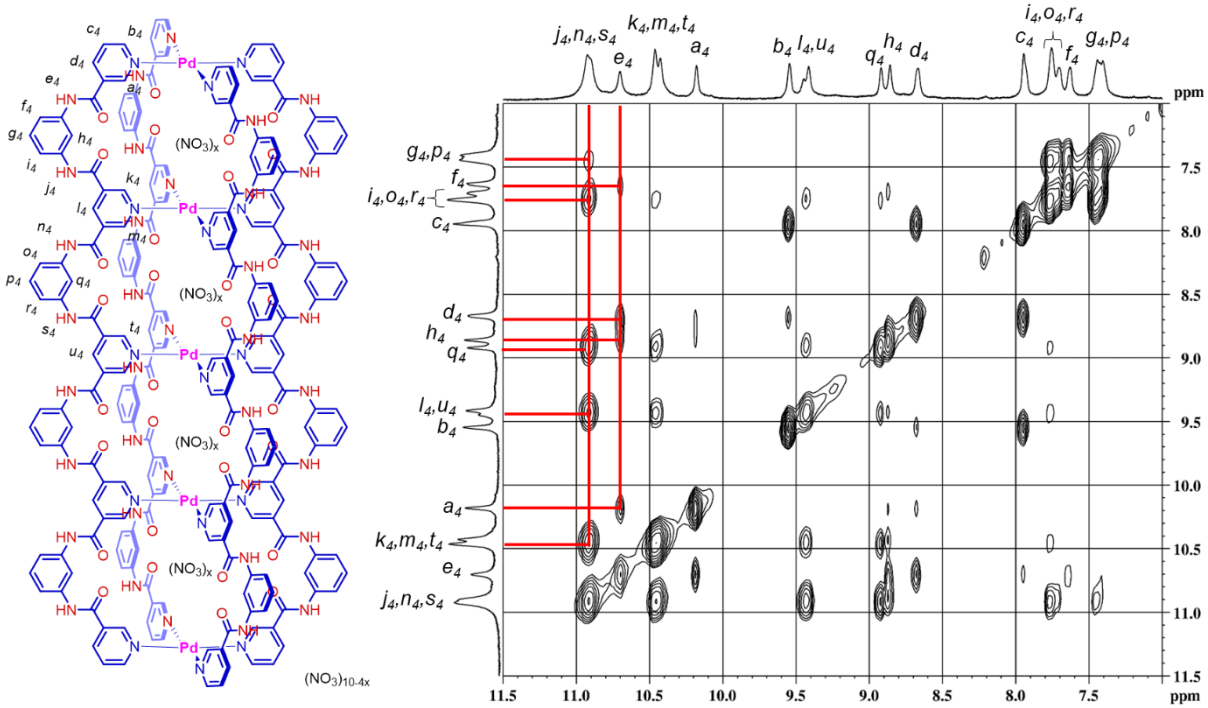

Figure S36a. H-H NOESY (500 MHz, 298 K) expansion spectrum of complex, **4·10NO$_3$** in DMSO-d_6.

S. ESI-MS Characterisation of the Pd(II) complexes

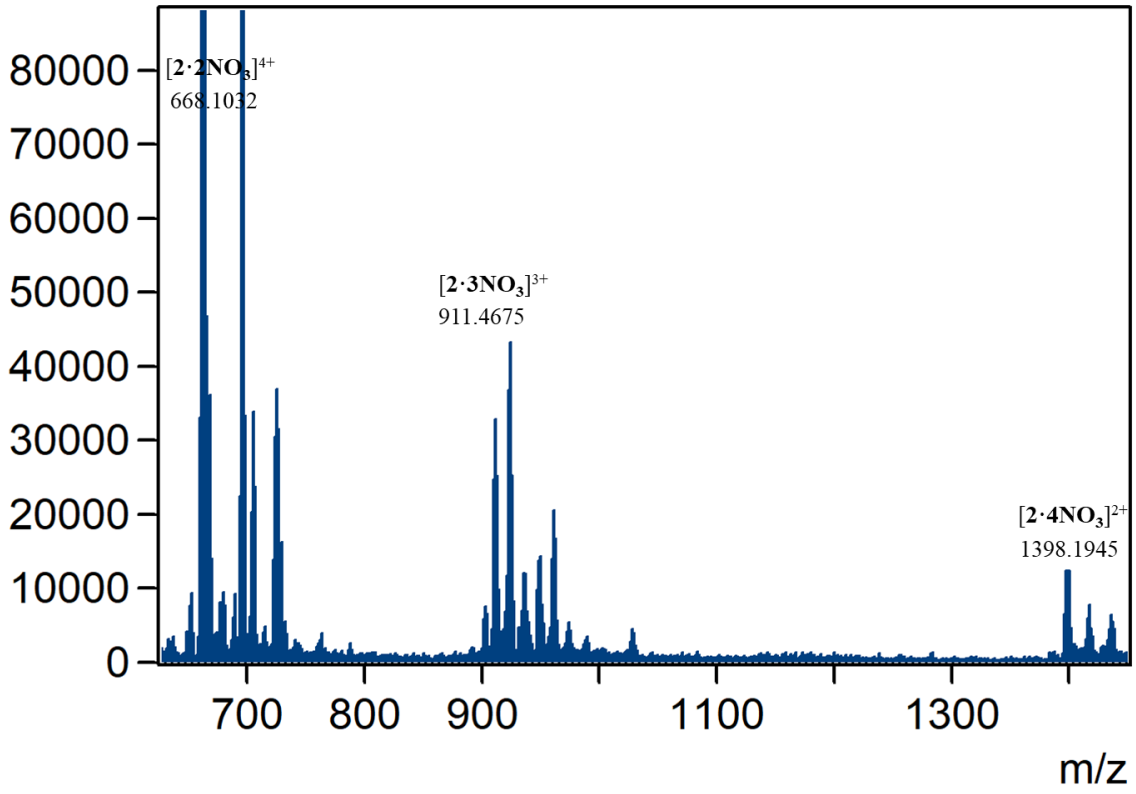

Figure S37. ESI mass spectral analysis for complex **2·6NO₃**

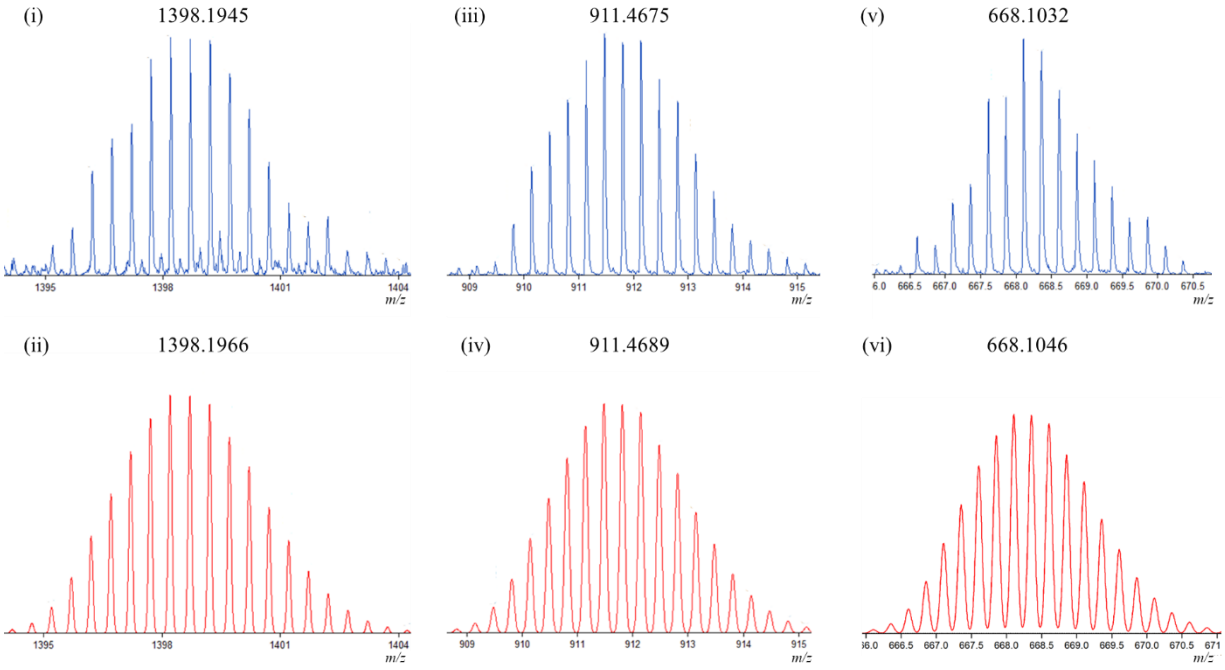

Figure S37a. Experimental (i), (iii), (v) and theoretical (ii), (iv), (vi) isotopic pattern for $[\mathbf{2\cdot4NO_3}]^{2+}$, $[\mathbf{2\cdot3NO_3}]^{3+}$ and $[\mathbf{2\cdot2NO_3}]^{4+}$ respectively.

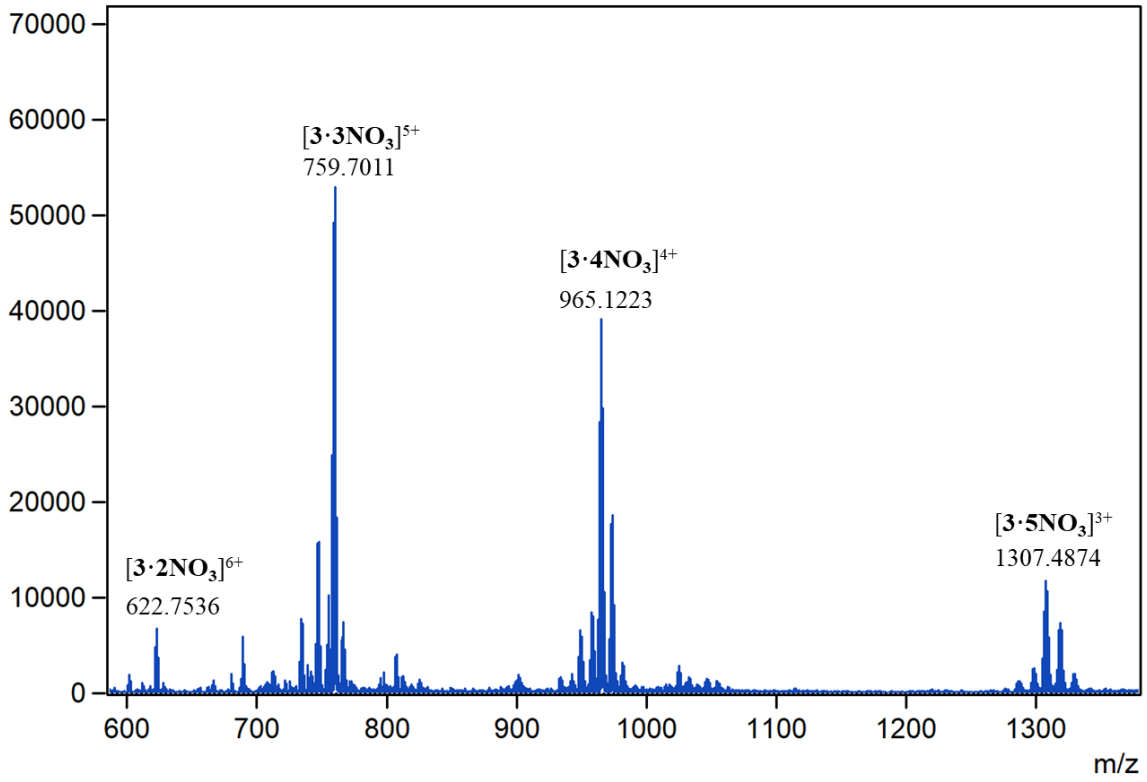

Figure S38. ESI mass spectral analysis for complex **3·8NO$_3$**

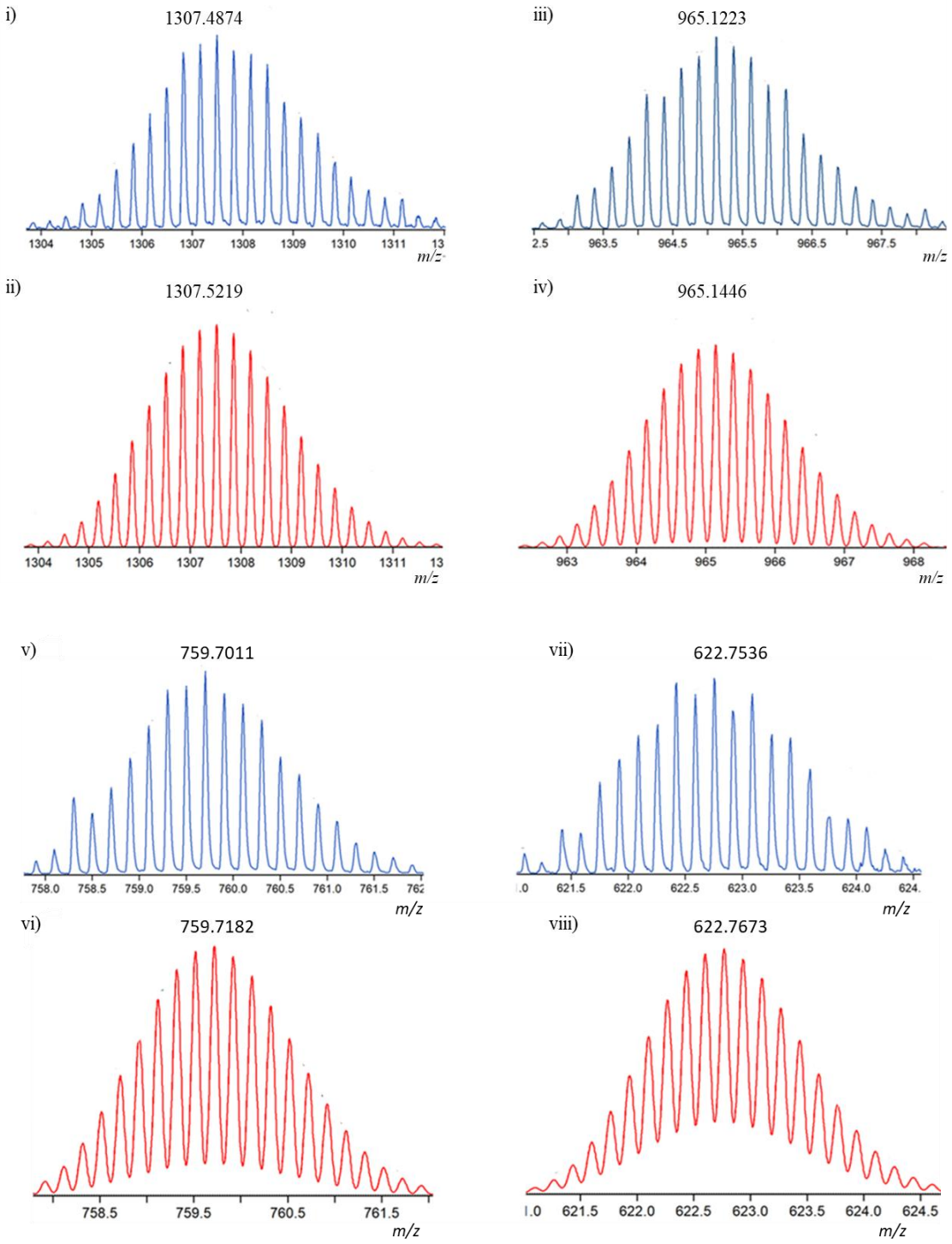

Figure S38a. Experimental (i), (iii), (v), (vii) and theoretical (ii), (iv), (vi), (viii) isotopic pattern for $[\mathbf{3{\cdot}5NO_3}]^{3+}$, $[\mathbf{3{\cdot}4NO_3}]^{4+}$, $[\mathbf{3{\cdot}3NO_3}]^{5+}$ and $[\mathbf{3{\cdot}2NO_3}]^{6+}$ respectively.

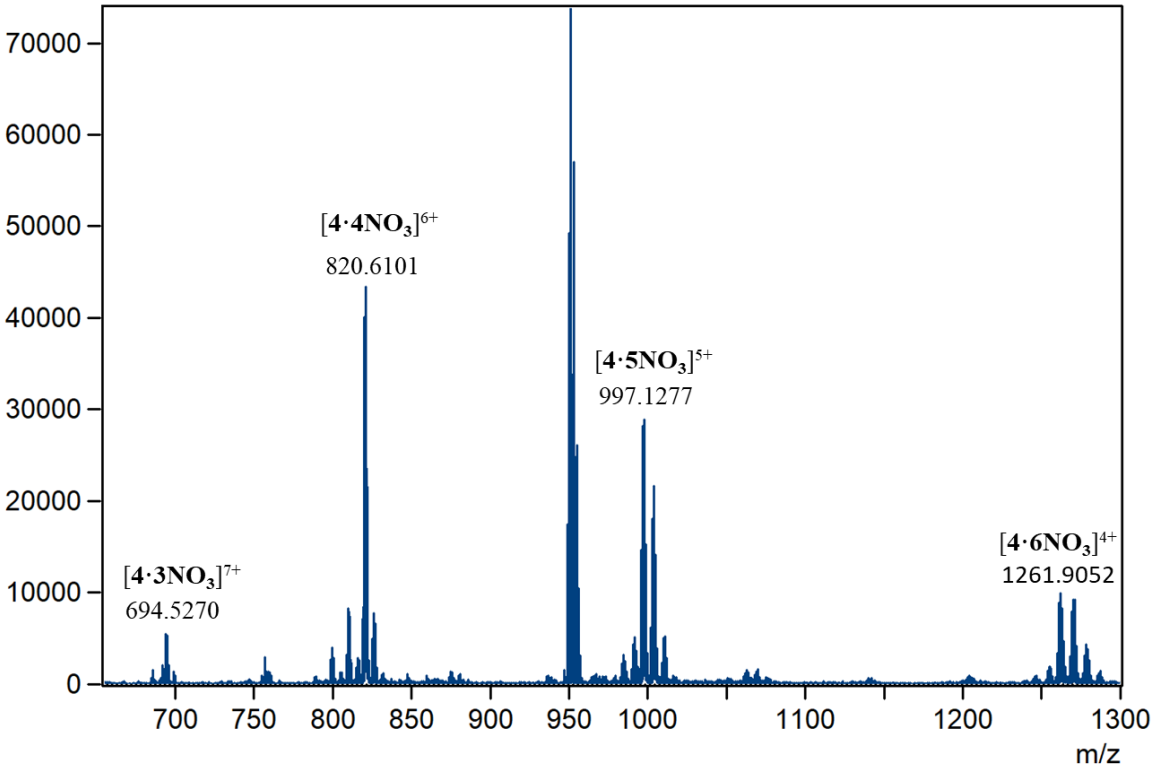

Figure S39. ESI mass spectral analysis for complex **4·10NO$_3$**

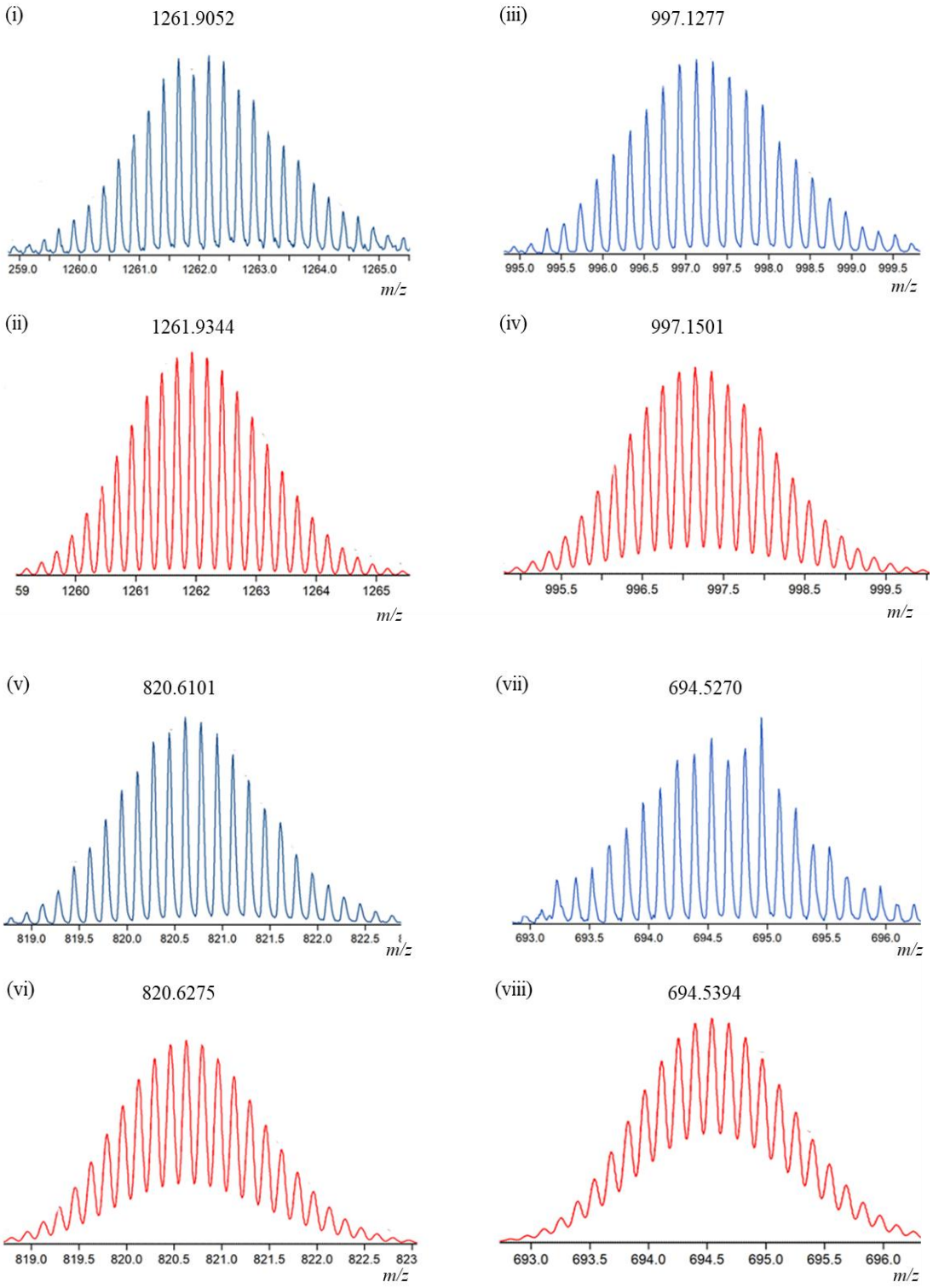

Figure S39a. Experimental (i), (iii), (v), (vii) and theoretical (ii), (iv), (vi), (viii) isotopic pattern for $[\mathbf{4{\cdot}6NO_3}]^{4+}$, $[\mathbf{4{\cdot}5NO_3}]^{5+}$, $[\mathbf{4{\cdot}4NO_3}]^{6+}$ and $[\mathbf{4{\cdot}3NO_3}]^{7+}$ respectively.

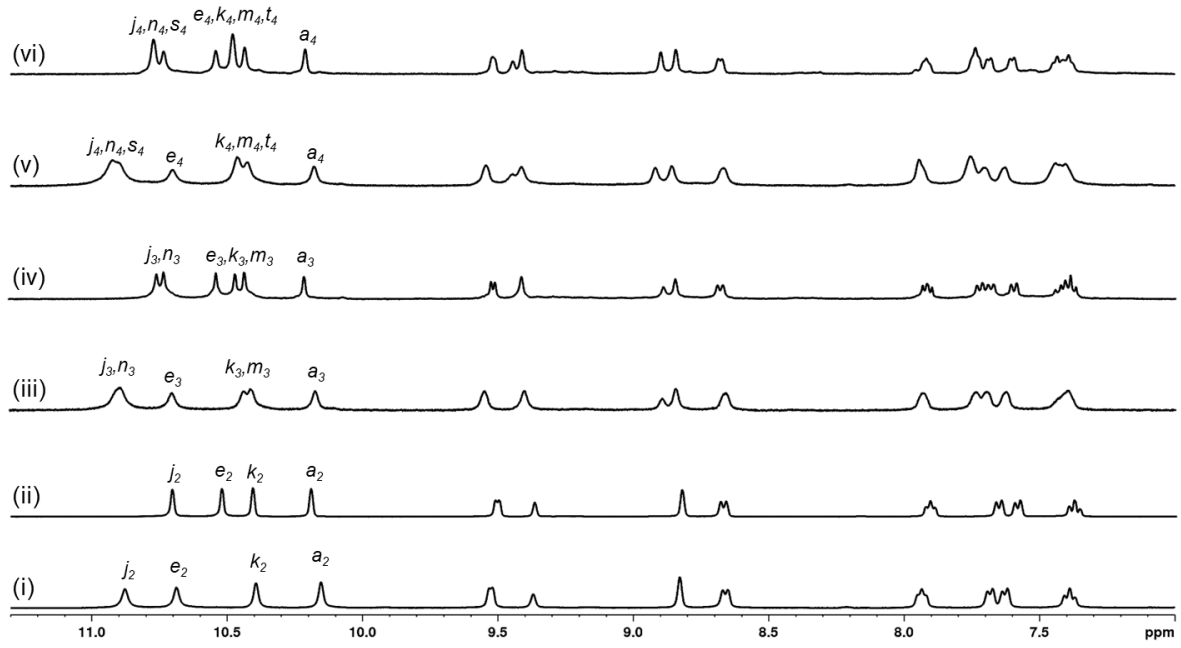

Figure S40. Stacked partial ^{1}H NMR spectra (400 MHz) at 298 K of (i) complex **2·6NO$_3$**, (iii) complex **3·8NO$_3$**, (v) complex **4·10NO$_3$**, and at 353 K (ii) complex **2·6NO$_3$**, (iv) complex **3·8NO$_3$**, (vi) complex **4·10NO$_3$**.

S4. Narcissistic self-sorting

One pot complexation of $Pd(NO_3)_2$ with a mixture of L1 and L2

Synthesis procedure: Mixture of ligands **L1** (1.01 mg, 0.008 mmol) and **L2** (1.78 mg, 0.008 mmol) were dissolved in 0.4 mL of DMSO-d_6, to which solution $Pd(NO_3)_2$ (0.92 mg, 0.010 mmol) was added and stirred at 70 °C for 20 min to obtain dynamic equilibrium of $[(NO_3)_x \subset Pd_2(\mathbf{L1})_4](NO_3)_{4-x}$, **1·4NO₃** and $[(NO_3)_y \subset Pd_3(\mathbf{L1})_6](NO_3)_{6-y}$, **1'·6NO₃** along with narcissistically self-sorted $[(NO_3)_{2x} \subset Pd_3(\mathbf{L2})_4](NO_3)_{6-2x}$, **2·6NO₃**.

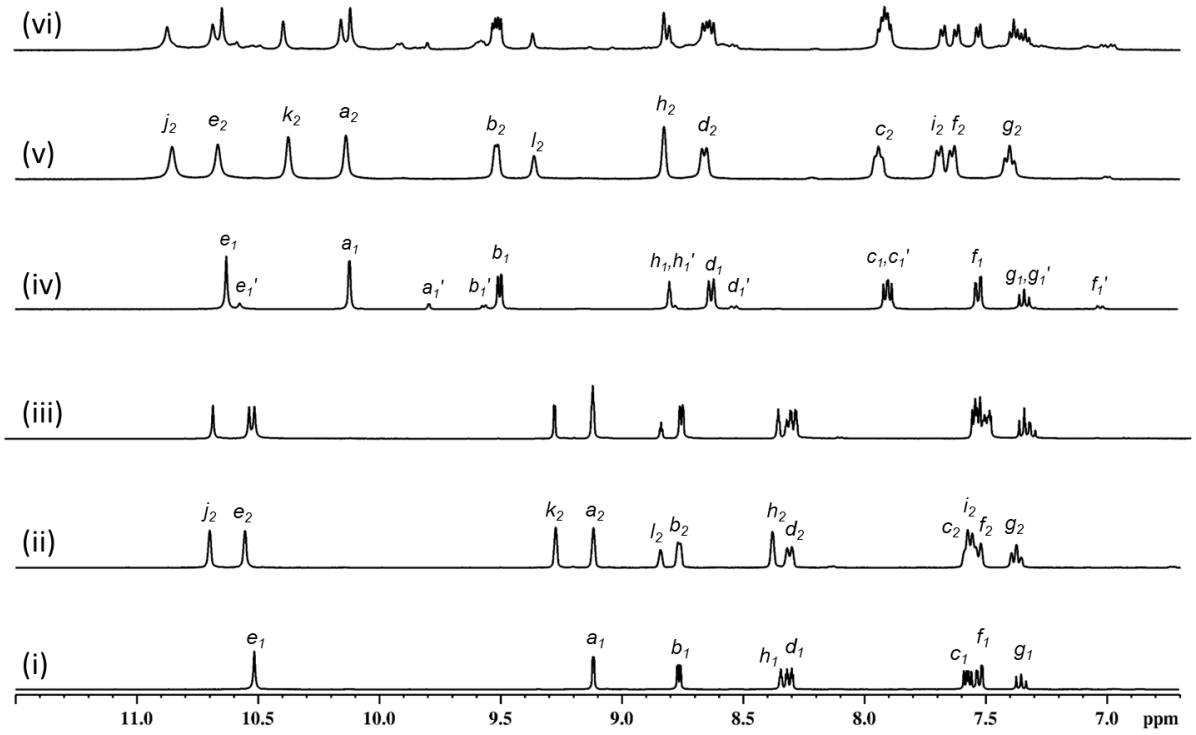

Figure S41. Partial ^{1}H NMR spectra (400 MHz, 298 K, DMSO-d_6) of i) ligand **L1**, ii) ligand **L2**, iii) **L1** + **L2** (1:1), iv) **L1** + $Pd(NO_3)_2$, 5 min, rt, **1·4NO₃** + **1'·6NO₃**, v) **L2** + $Pd(NO_3)_2$, 20 min, 70 ˚C, **2·6NO₃**, and vi) **L1** + **L2** (1:1) + $Pd(NO_3)_2$, 20 min, 70 ˚C, mixture of **1·4NO₃** + **1'·6NO₃** + **2·6NO₃**

One pot complexation of $Pd(NO_3)_2$ with a mixture of L1 and L3

Synthesis procedure: Mixture of ligands **L1** (0.84 mg, 0.0066 mmol) and **L3** (2.12 mg, 0.0066 mmol) were dissolved in 0.4 mL of DMSO-d_6, to which solution $Pd(NO_3)_2$ (0.92 mg, 0.010 mmol) was added and stirred at 70 °C for 12 h to obtain dynamic equilibrium of $[(NO_3)_x \subset Pd_2(\mathbf{L1})_4](NO_3)_{4-x}$, **1·4NO₃** and $[(NO_3)_y \subset Pd_3(\mathbf{L1})_6](NO_3)_{6-y}$, **1'·6NO₃** along with narcissistically self-sorted $[(NO_3)_{3x} \subset Pd_4(\mathbf{L3})_4](NO_3)_{8-3x}$, **3·8NO₃**.

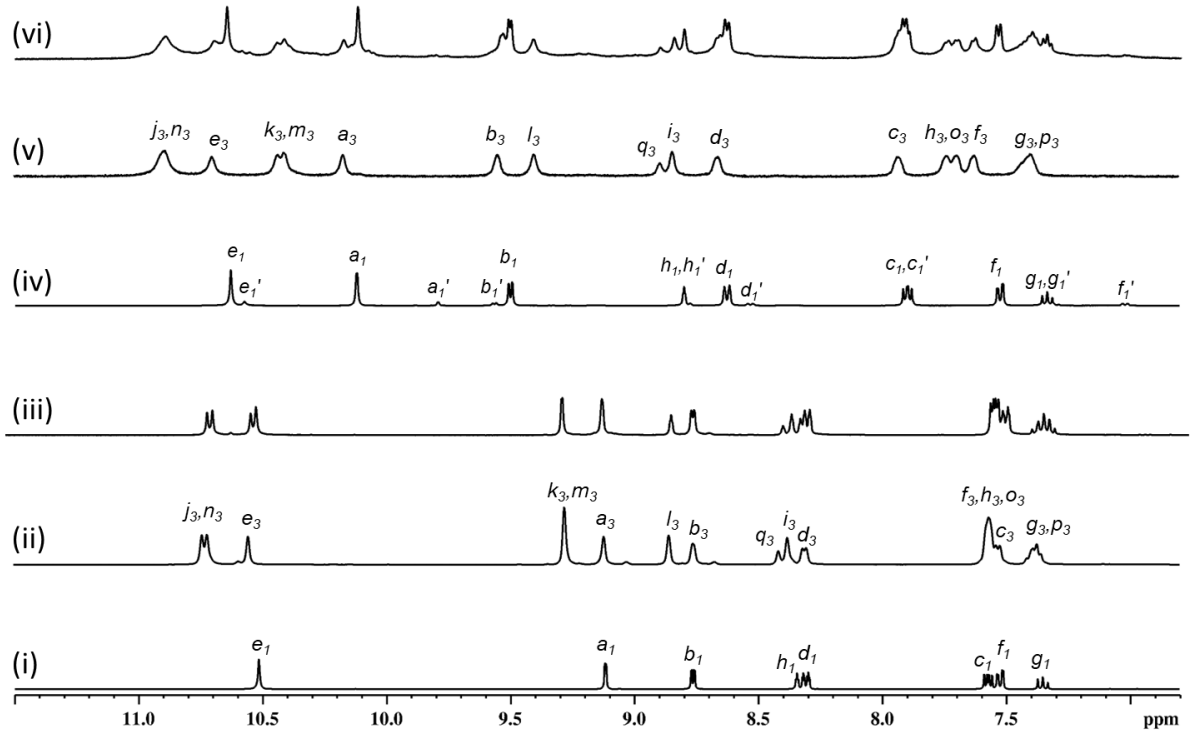

Figure S42. Partial ^{1}H NMR spectra (400 MHz, 298 K, DMSO-d_6) of i) ligand **L1**, ii) ligand **L3**, iii) **L1** + **L3** (1:1), iv) **L1** + $Pd(NO_3)_2$, 5 min, rt, **1·4NO₃** + **1'·6NO₃**, v) **L3** + $Pd(NO_3)_2$, 12 h, 70 ˚C, **3·8NO₃**, and vi) **L1** + **L3** (1:1) + $Pd(NO_3)_2$, 12 h, 70 ˚C, mixture of **1·4NO₃** + **1'·6NO₃** + **3·8NO₃**

One pot complexation of $Pd(NO_3)_2$ with a mixture of L1 and L4

Synthesis procedure: Mixture of ligands **L1** (0.50 mg, 0.004 mmol) and **L**4 (1.65 mg, 0.004 mmol) were dissolved in 0.4 mL of DMSO-d_6, to which solution $Pd(NO_3)_2$ (0.64 mg, 0.007 mmol) was added and stirred at 70 °C for 24 h to obtain dynamic equilibrium of $[(NO_3)_x \subset Pd_2(\mathbf{L1})_4](NO_3)_{4-x}$, **1·4NO₃** and $[(NO_3)_y \subset Pd_3(\mathbf{L1})_6](NO_3)_{6-y}$, **1'·6NO₃** along with narcissistically self-sorted $[(NO_3)_{4x} \subset Pd_5(\mathbf{L4})_4](NO_3)_{10-4x}$, **4·10NO₃**.

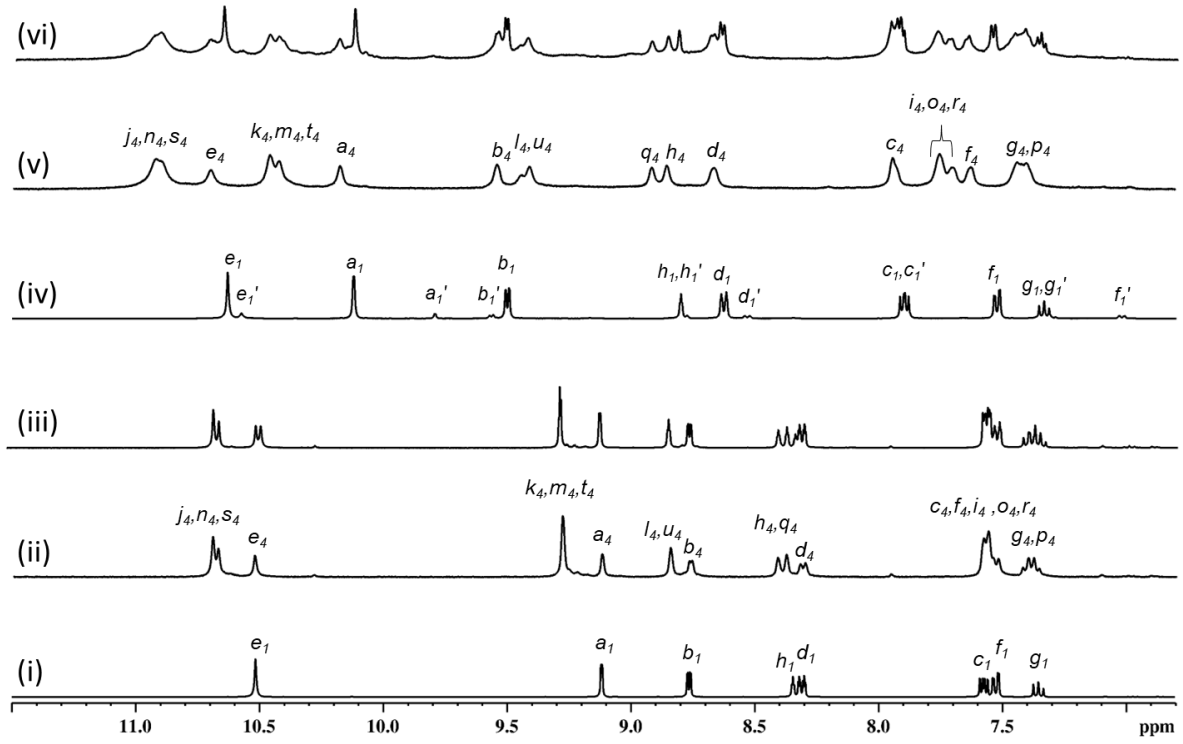

Figure S43. Partial ^{1}H NMR spectra (400 MHz, 298 K, DMSO-d_6) of i) ligand **L1**, ii) ligand **L4**, iii) **L1** + **L4** (1:1), iv) **L1** + $Pd(NO_3)_2$, 5 min, rt, **1·4NO₃** + **1'·6NO₃**, v) **L4** + $Pd(NO_3)_2$, 24 h, 70 ˚C, **4·10NO₃**, and vi) **L1** + **L4** (1:1) + $Pd(NO_3)_2$, 24 h, 70 ˚C, mixture of **1·4NO₃** + **1'·6NO₃** + **4·10NO₃**

S5. Host-Guest study (at 298 K)

Encapsulation study in $[(NO_3)_{2x}\subset Pd_3(L2)_4](NO_3)_{4-2x}$, $2\cdot 6NO_3$

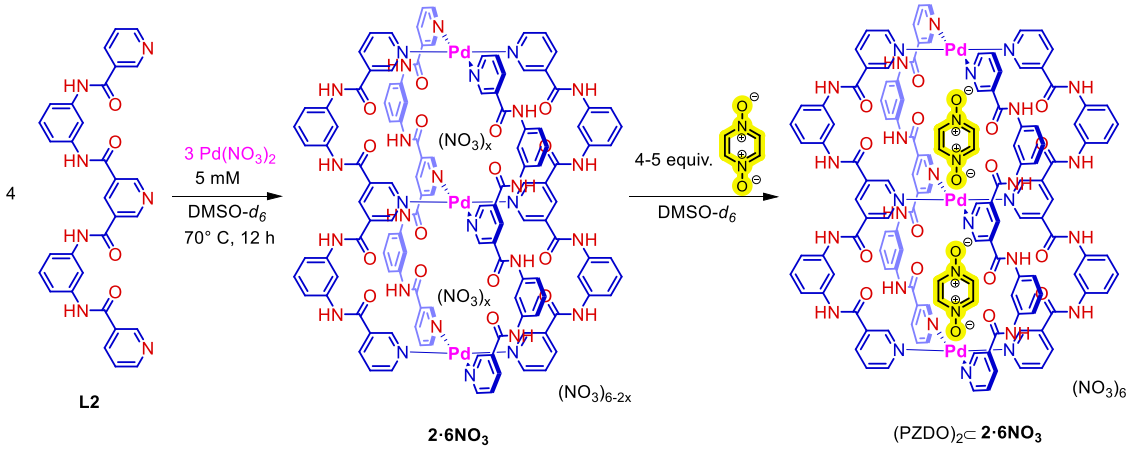

Scheme S7. Synthesis of complex $\mathbf{2\cdot 6NO_3}$ and $(PZDO)_2\subset\mathbf{2\cdot 6NO_3}$.

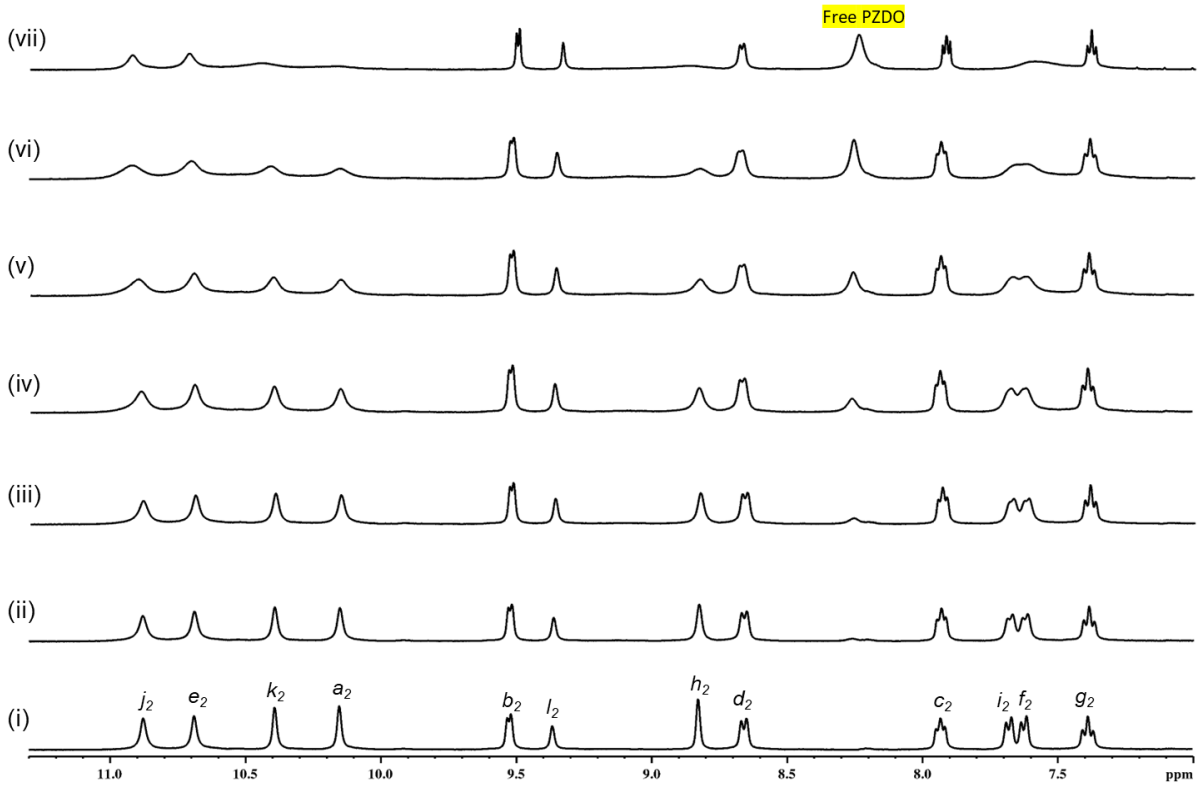

Figure S44. Stacked partial ^{1}H NMR spectra (400 MHz, 298 K) of (i) complex $\mathbf{2\cdot 6NO_3}$**;** portion-wise addition of PZDO to complex $\mathbf{2\cdot 6NO_3}$ (ii) 0.5 equiv., (iii) 1 equiv., (iv) 2 equiv., (v) 3 equiv., (vi) 4 equiv. and (vii) 7 equiv. in DMSO-d_6.

Encapsulation study in $[(NO_3)_{3x}\subset Pd_4(L3)_4](NO_3)_{8-3x}$, $3\cdot 8NO_3$

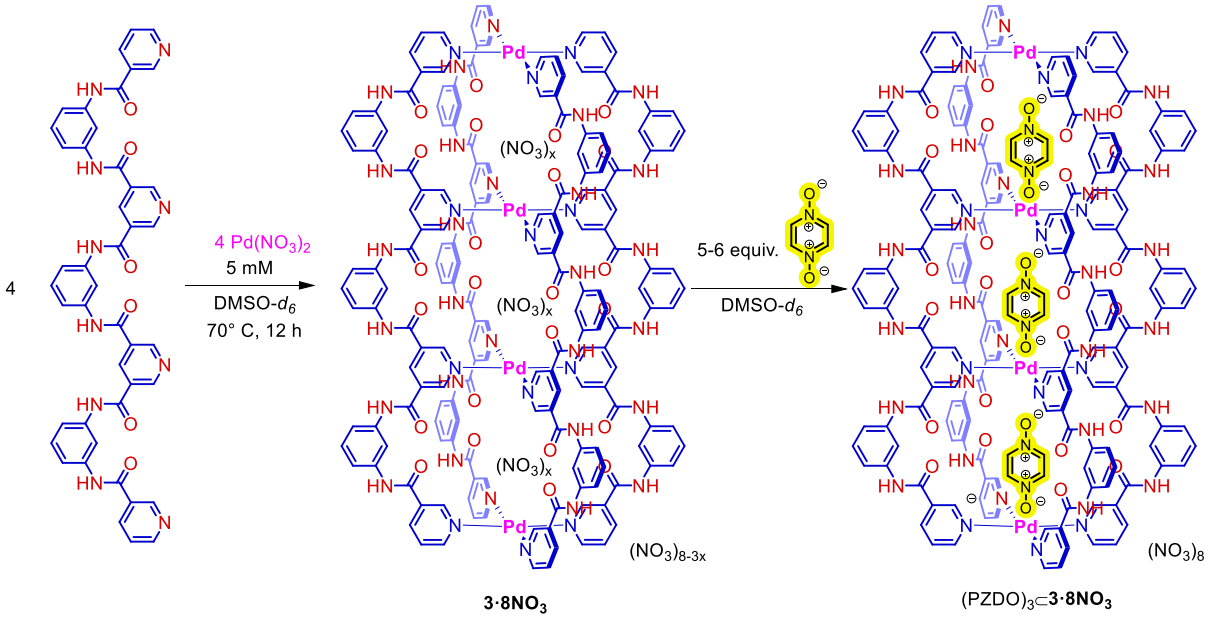

Scheme S8. Synthesis of complex $\mathbf{3\cdot 8NO_3}$ and $(PZDO)_3\subset\mathbf{3\cdot 8NO_3}$.

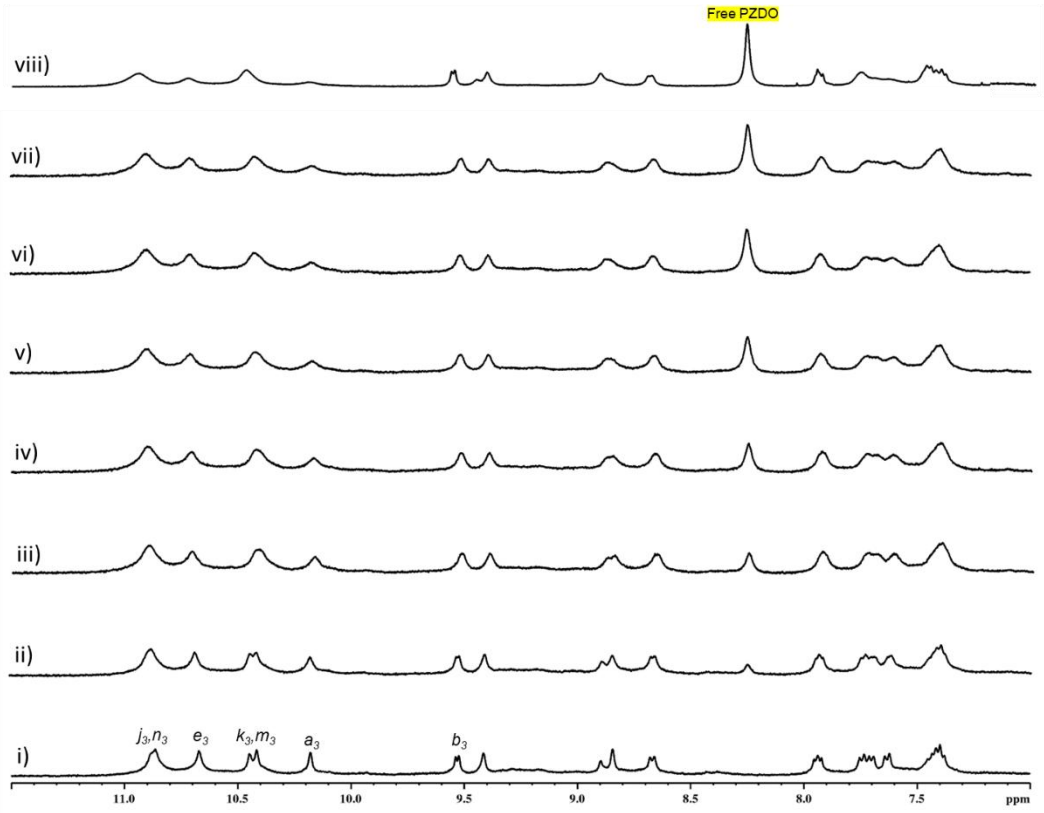

Figure S45. Stacked partial ^{1}H NMR spectra (400 MHz, 298 K) of (i) complex $\mathbf{3\cdot 8NO_3}$**;** portion-wise addition of PZDO to complex $\mathbf{3\cdot 8NO_3}$ (ii) 1 equiv., (iii) 2 equiv., (iv) 3 equiv., (v) 4 equiv., (vi) 5 equiv., (vii) 8 equiv. and (viii) 10 equiv. in DMSO-d_6.

Encapsulation study in $[(NO_3)_{4x}\subset Pd_5(L4)_4](NO_3)_{10-4x}$, $4\cdot10NO_3$

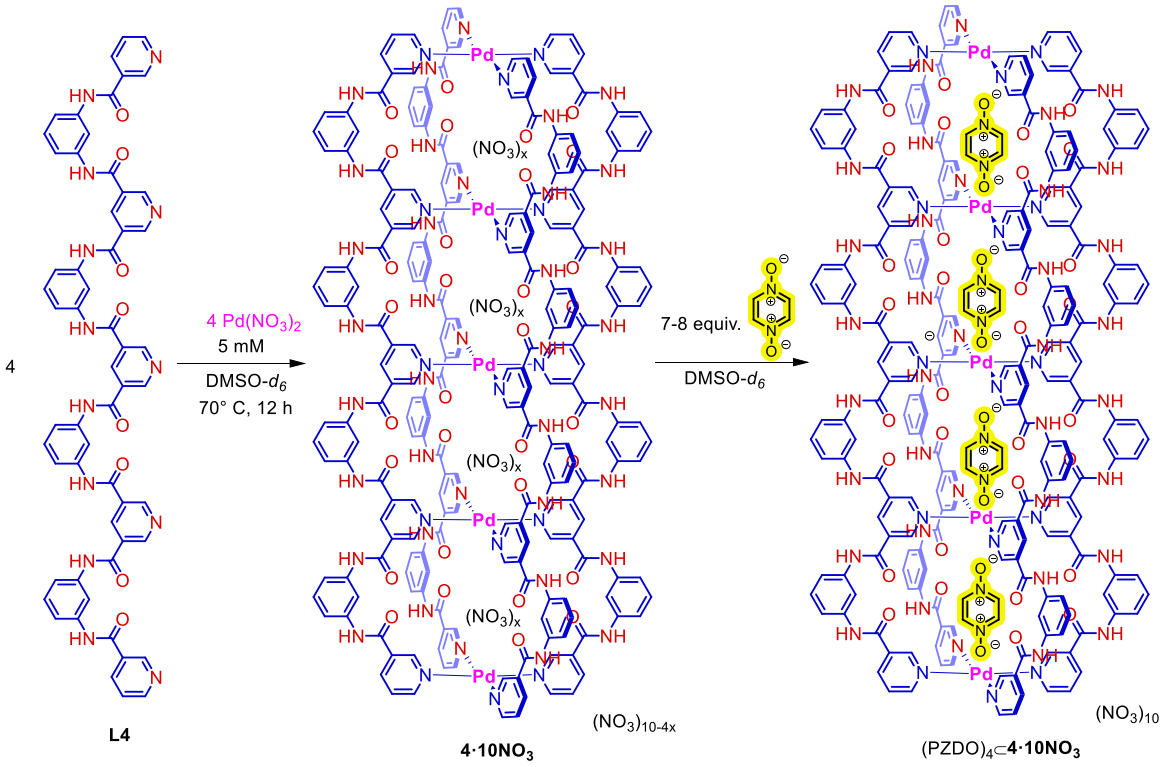

Scheme S9. Synthesis of complex $\mathbf{4\cdot10NO_3}$ and $(PZDO)_4\subset\mathbf{4\cdot10NO_3}$.

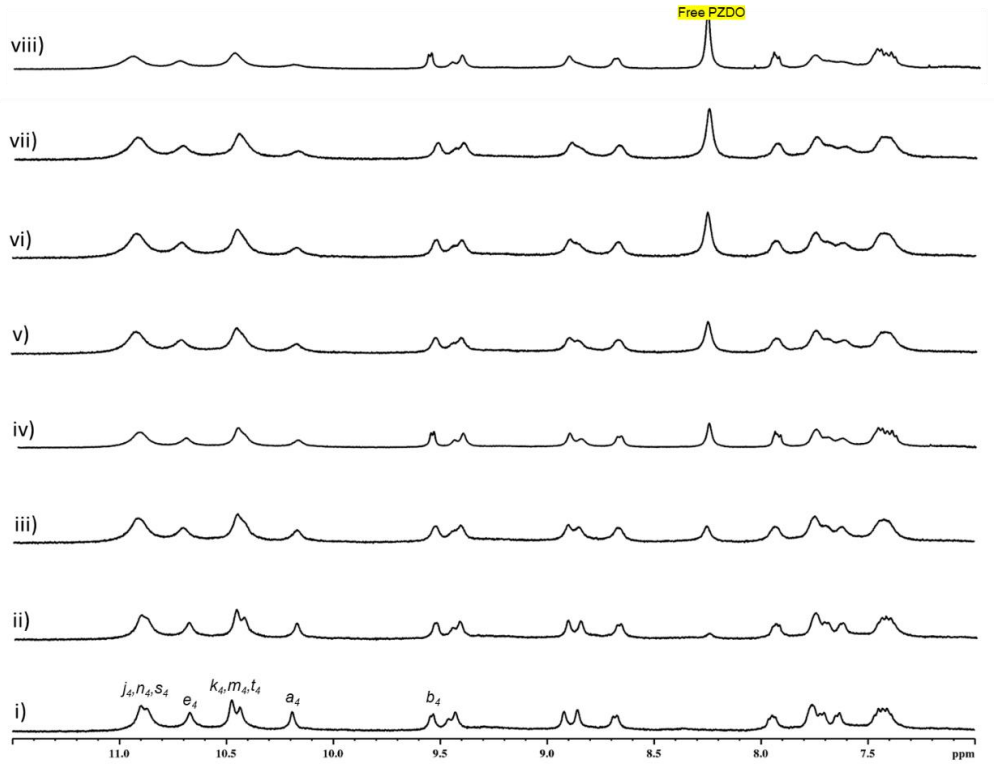

Figure S46. Stacked partial ^{1}H NMR spectra (400 MHz, 298 K) of (i) complex $\mathbf{4\cdot10NO_3}$**;** portion-wise addition of PZDO to complex $\mathbf{4\cdot10NO_3}$ (ii) 1 equiv., (iii) 3 equiv., (iv) 4 equiv., (v) 5 equiv., (vi) 6 equiv., (vii) 8 equiv. and (viii) 10 equiv. in DMSO-d_6.

Host-Guest study (at 353 K)

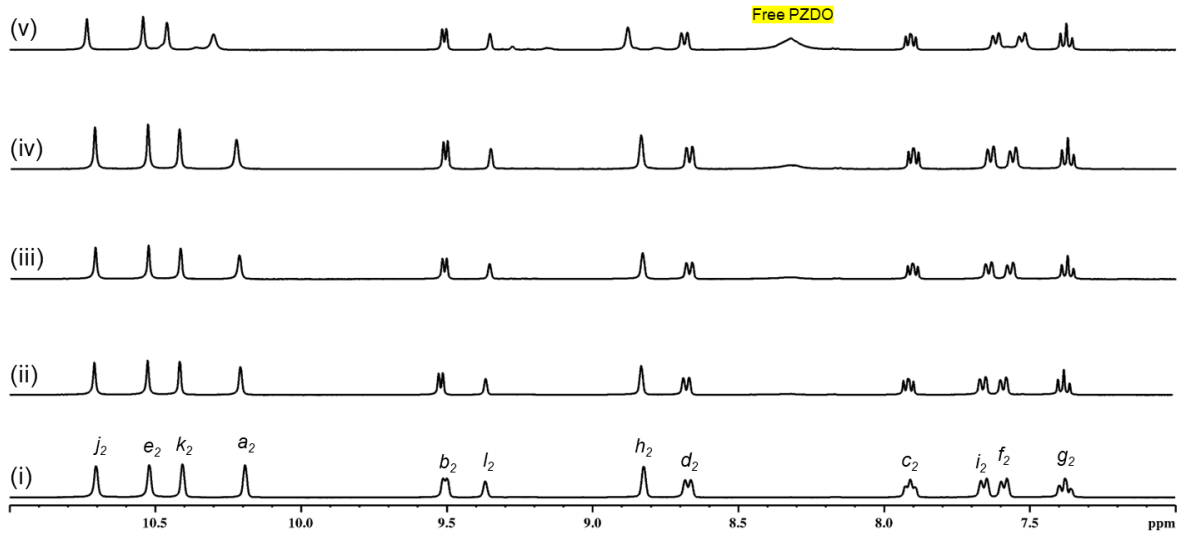

Figure S47. Stacked partial ^{1}H NMR spectra (400 MHz, 353 K) of (i) complex **2·6NO$_3$;** portion-wise addition of PZDO to complex **2·6NO$_3$** (ii) 0.5 equiv., (iii) 1 equiv., (iv) 1.5 equiv. and (v) 4 equiv. in DMSO-d_6.

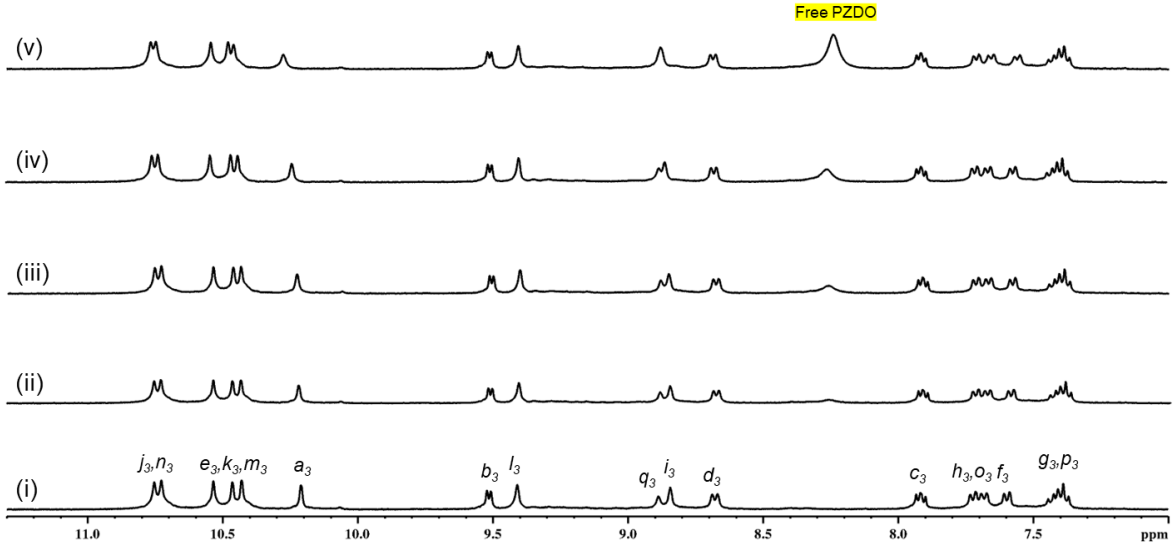

Figure S48. Stacked partial ^{1}H NMR spectra (400 MHz, 353 K) of (i) complex **3·8NO$_3$**; portion-wise addition of PZDO to complex **3·8NO$_3$** (ii) 1 equiv., (iii) 2 equiv., (iv) 3 equiv. and (v) 6 equiv. in DMSO-d_6.

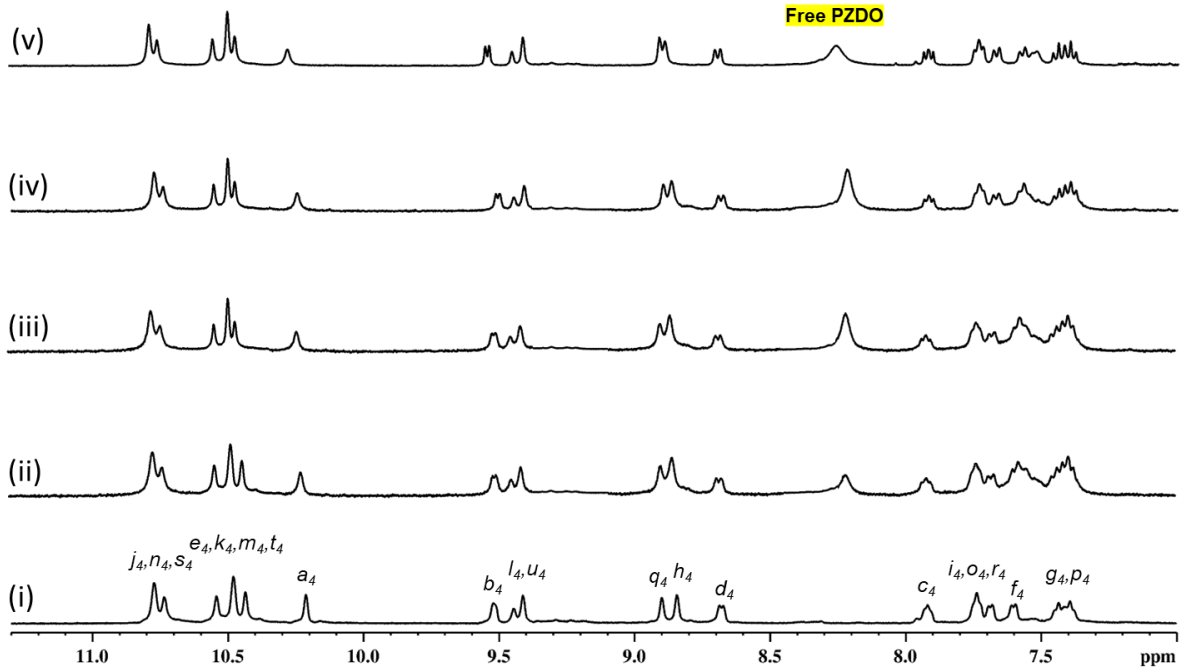

Figure S49. Stacked partial ^{1}H NMR spectra (400 MHz, 353 K) of (i) complex **4·10NO$_3$**; portion-wise addition of PZDO to complex **4·10NO$_3$** (ii) 2 equiv., (iii) 4 equiv., (iv) 6 equiv. and (v) 8 equiv. in DMSO-*d*$_6$.

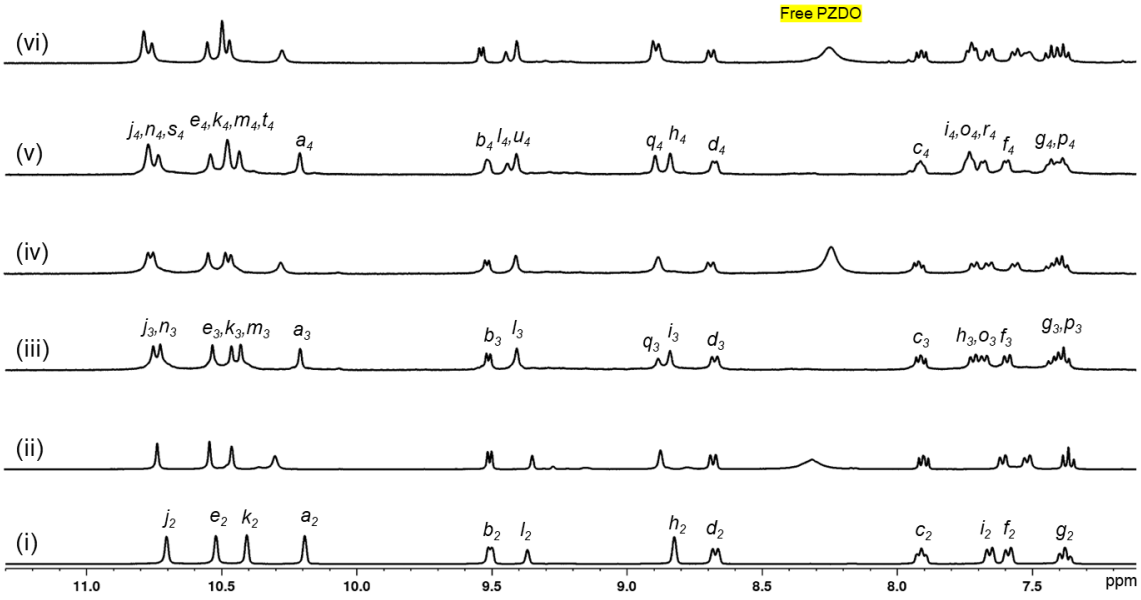

Figure S50. Stacked partial ^{1}H NMR spectra (400 MHz, 353 K) of (i) complex **2·6NO$_3$**, (ii) **2·6NO$_3$** + 4 equiv. PZDO, (iii) complex **3·8NO$_3$**, (iv) **3·8NO$_3$** + 6 equiv. PZDO, (v) complex **4·10NO$_3$** and (vi) **4·10NO$_3$** + 8 equiv. PZDO in DMSO-*d*$_6$.

ESI-MS Characterisation of the Host-Guest complexes

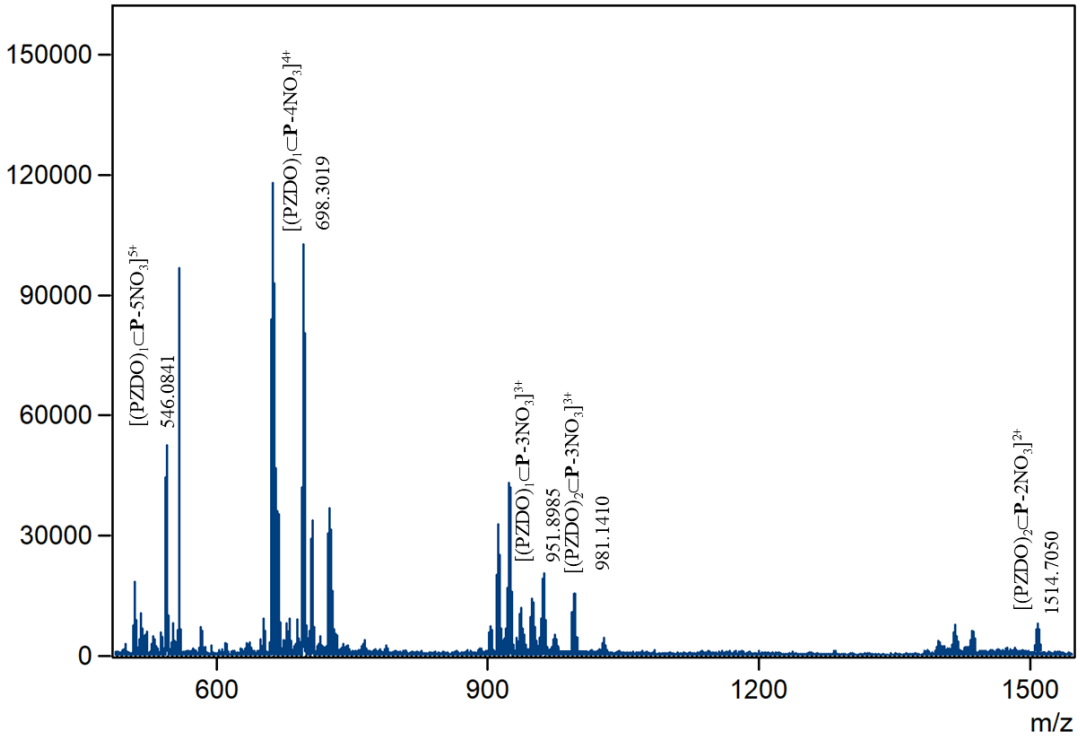

Figure S51. ESI mass spectral analysis for complex [$(PZDO)_n$⊂**P**] (where **P**=**2·6NO₃** and n = 1,2)

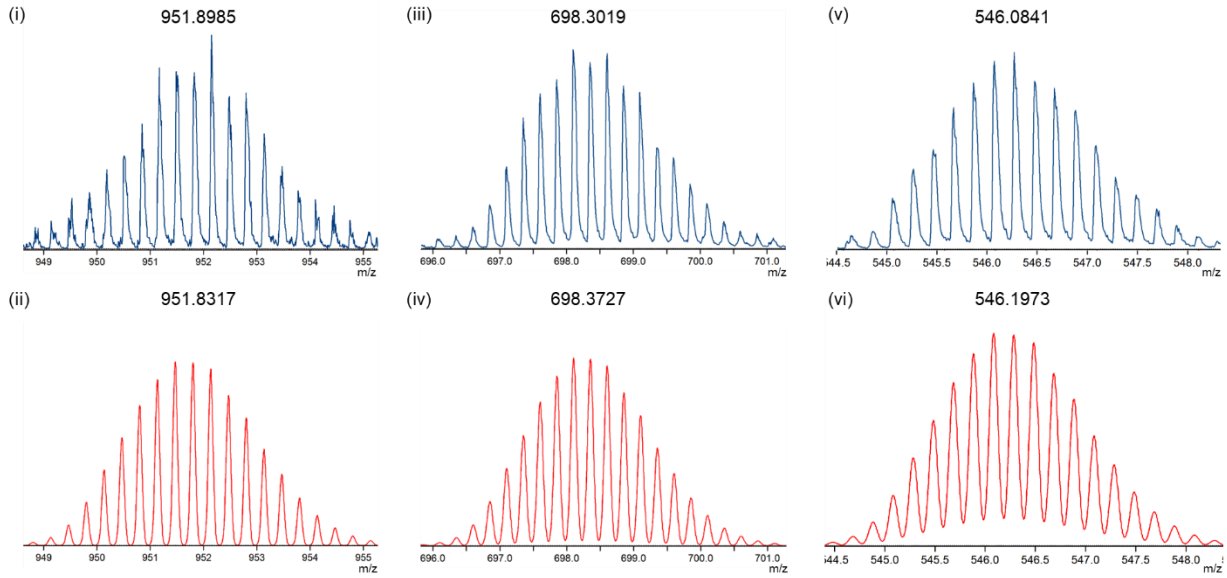

Figure S51a. Experimental (i), (iii), (v) and theoretical (ii), (iv), (vi) isotopic pattern for $[(PZDO)_1 \subset \mathbf{P}\text{-}3NO_3]^{3+}$, $[(PZDO)_1 \subset \mathbf{P}\text{-}4NO_3]^{4+}$ and $[(PZDO)_1 \subset \mathbf{P}\text{-}5NO_3]^{5+}$ respectively.

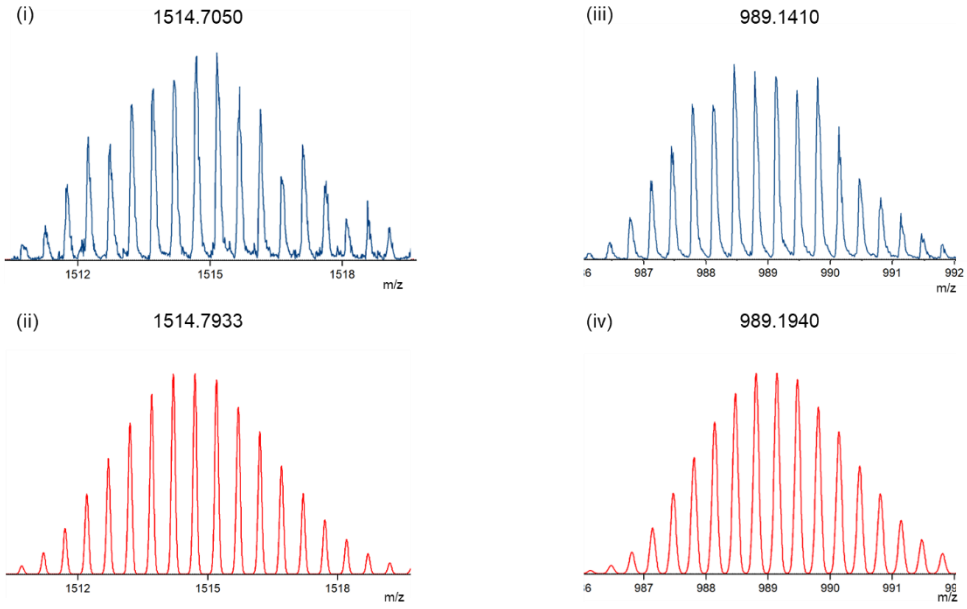

Figure S51b. Experimental (i), (iii) and theoretical (ii), (iv) isotopic pattern for $[(PZDO)_2 \subset \mathbf{P}\text{-}2NO_3]^{2+}$ and $[(PZDO)_2 \subset \mathbf{P}\text{-}3NO_3]^{3+}$ respectively.

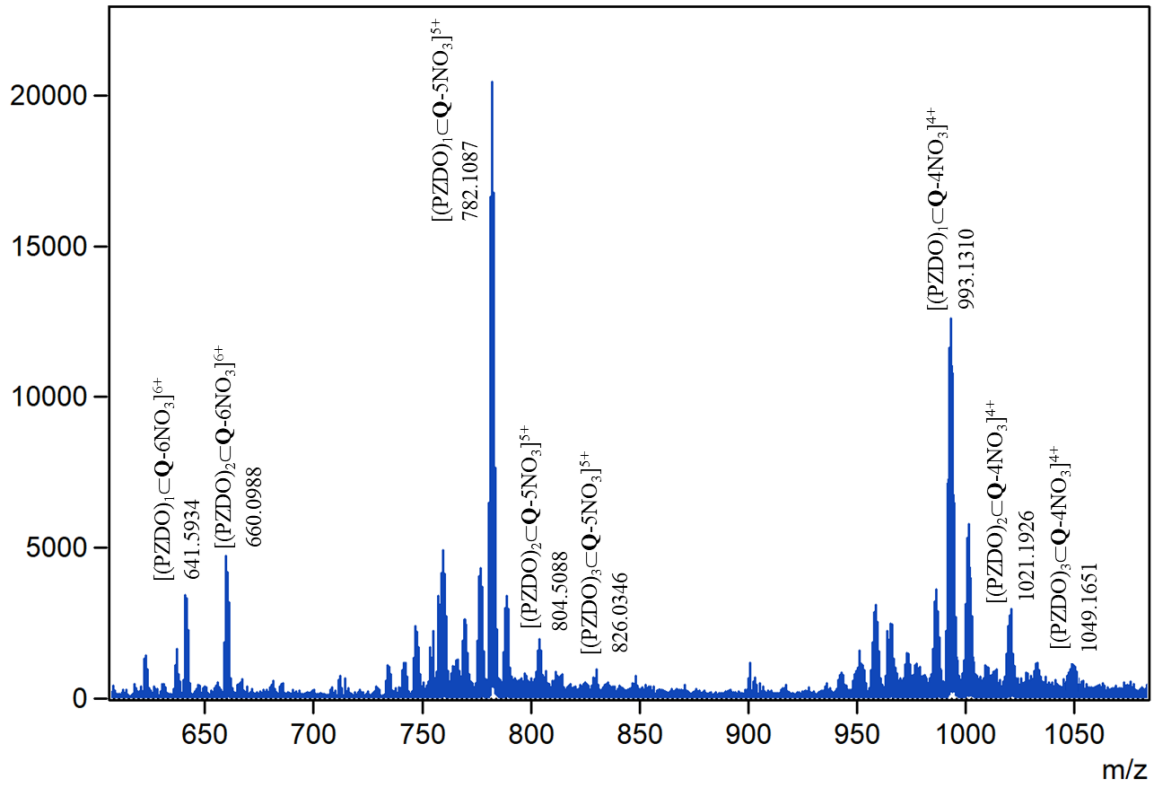

Figure S52. ESI mass spectral analysis for complex[$(PZDO)_n \subset$**Q**] (where **Q**=**3·8NO₃** and n = 1,2,3)

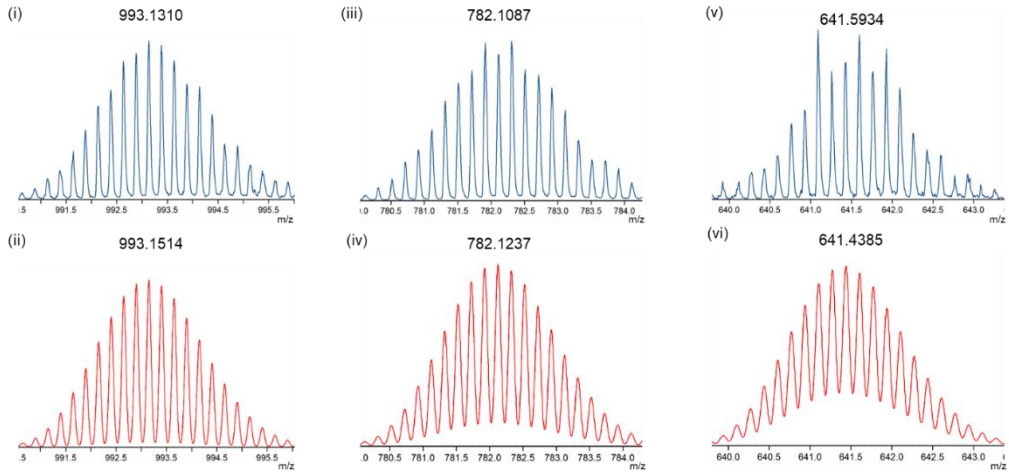

Figure S52a. Experimental (i), (iii), (v) and theoretical (ii), (iv), (vi) isotopic pattern for $[(PZDO)_1 \subset \mathbf{Q}\text{-}3NO_3]^{3+}$, $[(PZDO)_1 \subset \mathbf{Q}\text{-}5NO_3]^{5+}$ and $[(PZDO)_1 \subset \mathbf{Q}\text{-}6NO_3]^{6+}$ respectively.

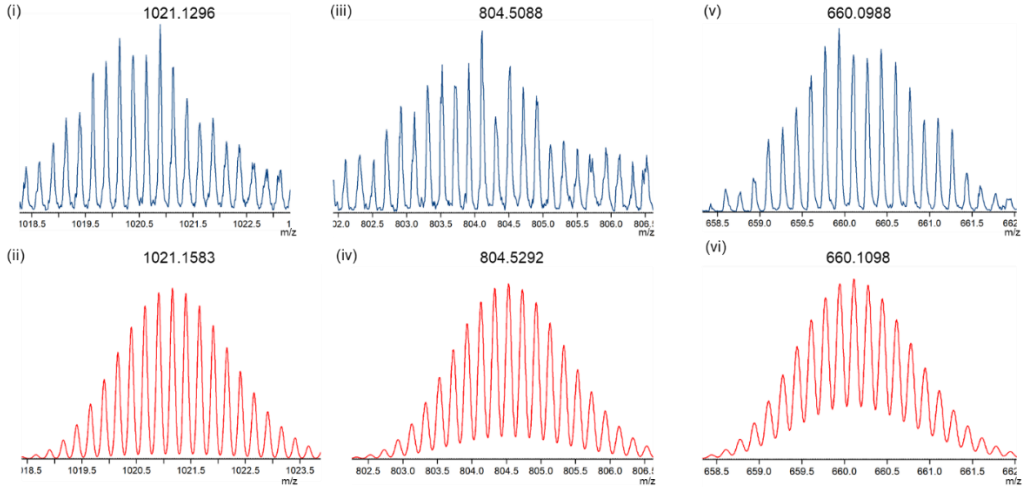

Figure S52b. Experimental (i), (iii), (v) and theoretical (ii), (iv), (vi) isotopic pattern for $[(PZDO)_2 \subset \mathbf{Q}\text{-}4NO_3]^{4+}$, $[(PZDO)_2 \subset \mathbf{Q}\text{-}5NO_3]^{5+}$ and $[(PZDO)_2 \subset \mathbf{Q}\text{-}6NO_3]^{6+}$ respectively.

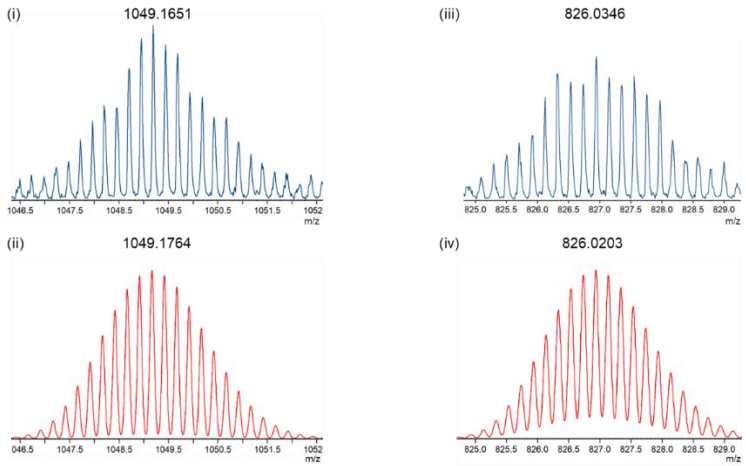

Figure S52c. Experimental (i), (iii) and theoretical (ii), (iv) isotopic pattern for $[(PZDO)_3 \subset \mathbf{Q}\text{-}4NO_3]^{4+}$and $[(PZDO)_3 \subset \mathbf{Q}\text{-}5NO_3]^{5+}$ respectively.

S6. DFT study

The metallosupramolecular structures were supported by geometry optimizations at B3LYP/LanL2DZ, 6-31G* level of theory by using the software Gaussian 16.[3-4]

Table S1. Calculated energy (in kJ/mol) of PZDO, empty hosts **[1]**$^{4+}$- **[4]**$^{10+}$ and guest encapsulated hosts $(G)_n$⊂host, G = PZDO, n= 1,2,3,4

Entry	**Host, and $(G)_n$⊂host, G=PZDO**	**Formula and short-hand symbol for hosts and host-guest entities**		**Energy (in kJ/mol)**	**Guest binding cooperativity as negative or positive cooperativity, along with magnitude in terms of energy**
		PZDO (G)	G	-1088634.8258	
1	[**1**]$^{4+}$	[**1**]$^{4+}$		-11835156.3391	
	$(G)_n$⊂[**1**]$^{4+}$	$(G)_1$⊂[**1**]$^{4+}$	G	-12923986.0294	
2	[**2**]$^{6+}$	[**2**]$^{6+}$	a.	-20730861.4898	
	$(G)_n$⊂[**2**]$^{6+}$	$(G)_1$⊂[**2**]$^{6+}$	b. G	-21819675.1882	
		$(G)_2$⊂[**2**]$^{6+}$	c. G G	-22908465.5723	**Negative** (23 kJ/mol) for steps b to c versus a to b
3	[**3**]$^{8+}$	[**3**]$^{8+}$	d.	-29626401.0870	
	$(G)_n$⊂[**3**]$^{8+}$	$(G)_1$⊂[**3**]$^{8+}$	e. G	-30715200.9832	
			f. G	-30715218.6003	
		$(G)_2$⊂[**3**]$^{8+}$	g. G G	-31803996.6497	**Negative** (5 kJ/mol) for steps e to g versus d to e **Negative** (30 kJ/mol) for steps f to g versus d to f
			h. G G	-31804037.9908	**Positive** (2 kJ/mol) for steps f to h versus d to f
		$(G)_3$⊂[**3**]$^{8+}$	i. G G G	-32892795.7530	**Positive** (4 kJ/mol) for steps g to i versus e/f to g **Negative** (61 kJ/mol) for steps h to i versus f to h
4	[**4**]$^{10+}$	[**4**]$^{10+}$	k.	-38521812.6805	
	$(G)_n$⊂[**4**]$^{10+}$	$(G)_1$⊂[**4**]$^{10+}$	l. G	-39610616.6253	
			m. G	-39610630.5089	
		$(G)_2$⊂[**4**]$^{10+}$	n. G G	-40699401.8265	**Negative** (19 kJ/mol) for steps l to n versus k to l
			o. G G	-40699413.3866	**Negative** (8 kJ/mol) for steps l to o versus k to l

					Negative (25 kJ/mol) for steps m to o versus k to m
			p. 	-40699436.4674	**Positive** (16 kJ/mol) for steps l to p versus k to l **Negative** (12 kJ/mol) for steps m to p versus k to m
			q. 	-40699448.2139	can be neglected (0.13 kJ/mol) for steps m to q versus k to m
		$(G)_3\subset[\mathbf{4}]^{10+}$	r.	-41788198.7559	**Positive** (12 kJ/mol) for steps n to r versus l to n **Negative** (11 kJ/mol) for steps o to r versus l/m to o **Negative** (44 kJ/mol) for steps p to r versus l/m to p
			s. 	-41788233.1500	**Positive** (23 kJ/mol) for steps o to s versus l/m to o **Negative** (10 kJ/mol) for steps p to s versus l/m to p **Negative** (32 kJ/mol) for steps q to s versus m to q
		$(G)_4\subset[\mathbf{4}]^{10+}$	t. 	-42876995.1025	**Positive** (15 kJ/mol) for steps r to t versus n/o to r **Negative** (38 kJ/mol) for steps s to t versus o/q to s

The energy differences between the empty host and the host-guest complexes for the catioinc cages $\mathbf{[1]}^{4+}$- $\mathbf{[4]}^{10+}$ were calculated. For the MCDCCs $\mathbf{[3]}^{8+}$ and $\mathbf{[4]}^{10+}$, there are multiple pathways available for calculating these energy differences, starting from the empty host and leading step-wise to the fully encapsulated host-guest complex. The following formula is used for the calculation

$$\Delta E = \Sigma \text{ products} - \Sigma \text{ reactants}$$

S6.1 Energy calculation for the formation of (PZDO)⊂$[\mathbf{1}]^{4+}$

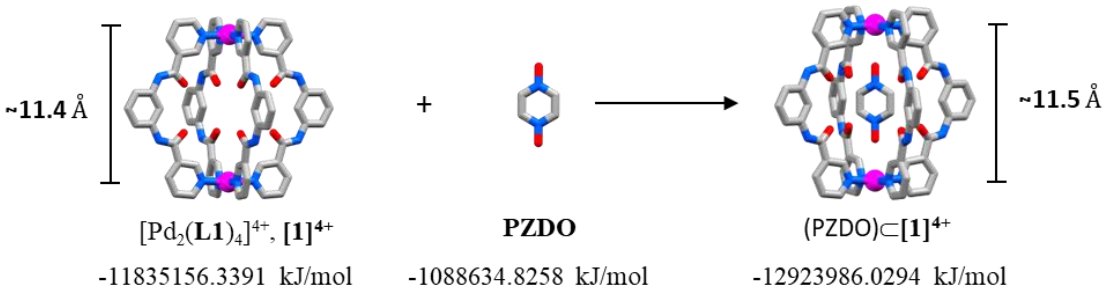

Figure S53. Energy optimized structures for the cationic part of complex $[Pd_2(\mathbf{L1})_4]^{4+}$, $\mathbf{[1]^{4+}}$; PZDO and guest encapsulated complex $(PZDO)_1\subset\mathbf{[1]^{4+}}$ (hydrogen atoms are not shown for clarity).

$\Delta E\ ((PZDO)\subset\mathbf{[1]^{4+}}) = \Sigma$ products - Σ reactants

$= ((PZDO)\subset[\mathbf{1}]^{4+}) - \{([\mathbf{1}]^{4+}) + (PZDO)_1\}$

$= (-12923986.0294) - \{(-11835156.3391) + (-1088634.8258)\}$

$= -194.8645$ kJ/mol

S6.2 Energy calculation for the formation of $(PZDO)_2\subset\mathbf{[2]^{6+}}$

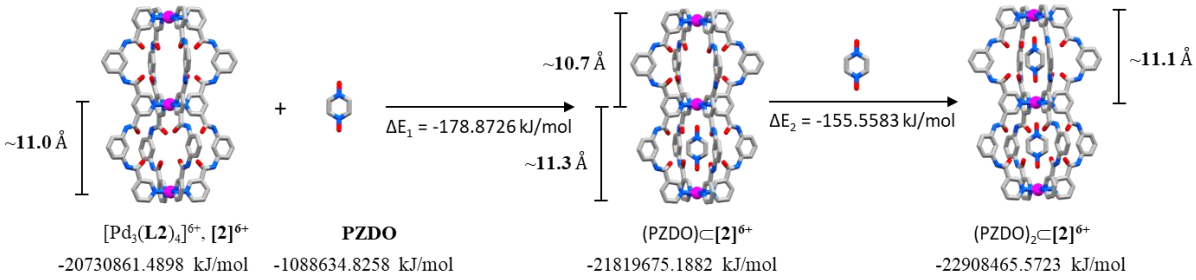

Figure S54. Energy optimized structures for the cationic part of complex $[Pd_3(\mathbf{L2})_4]^{6+}$, $\mathbf{[2]^{6+}}$; guest encapsulated complexes $(PZDO)\subset\mathbf{[2]^{6+}}$ and $(PZDO)_2\subset\mathbf{[2]^{6+}}$ (hydrogen atoms are not shown for clarity).

The formation of $(PZDO)_2\subset\mathbf{[2]^{6+}}$ follows a single path. From the calculation it can be seen that $\Delta E_1 < \Delta E_2$ which indicates, when one of the cavities is occupied by a guest molecule, the encapsulation of additional guest molecule becomes less favourable meaning negative cooperativity.

S6.3 Energy calculation for the formation of $(PZDO)_3\subset[\mathbf{3}]^{8+}$

The formation of $(PZDO)_3\subset\mathbf{[3]}^{6+}$ follows three different paths where calculated energy (in kJ/mol) of PZDO, $\mathbf{[3]}^{8+}$, host-guest complexes $(PZDO)_1\subset\mathbf{[3]}^{8+}$, $(PZDO)_2\subset\mathbf{[3]}^{8+}$ and $(PZDO)_3\subset\mathbf{[3]}^{8+}$ are shown.

S6.3.1 Path I and II

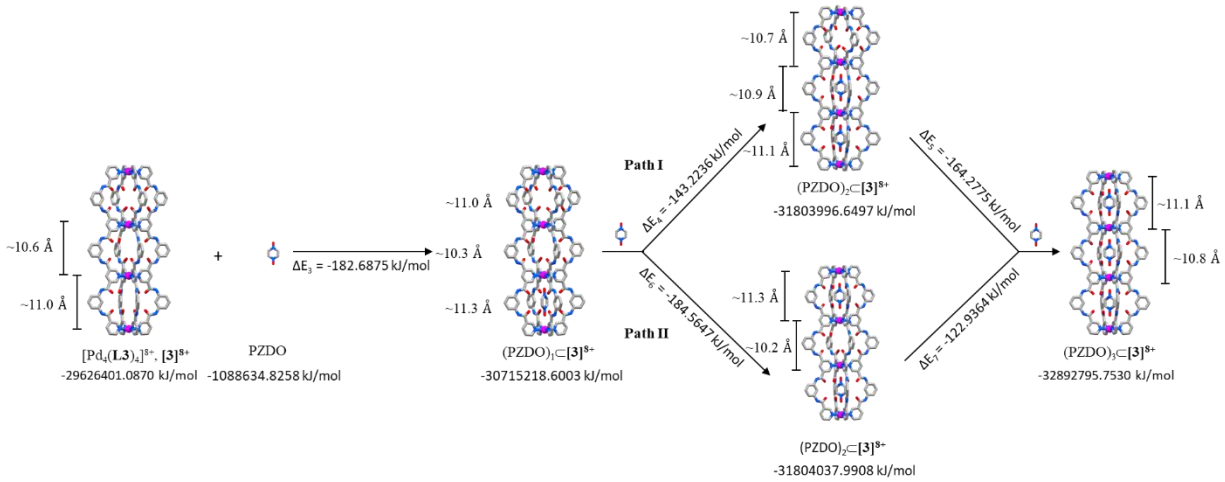

Figure S55. Energy optimized structures in gas phase for the cationic part of complex $[Pd_4(\mathbf{L3})_4]^{8+}$, $\mathbf{[3]}^{8+}$; guest encapsulated complexes $(PZDO)\subset\mathbf{[3]}^{8+}$, $(PZDO)_2\subset\mathbf{[3]}^{8+}$ and $(PZDO)_3\subset\mathbf{[3]}^{8+}$ (hydrogen atoms are not shown for clarity) following path I and II.

S6.3.2 Path III

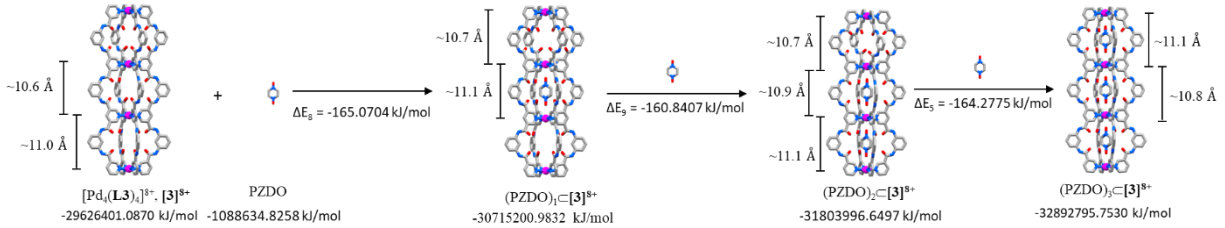

Figure S56. Energy optimized structures in gas phase for the cationic part of complex $[Pd_4(\mathbf{L3})_4]^{8+}$, $\mathbf{[3]}^{8+}$; guest encapsulated complexes $(PZDO)\subset\mathbf{[3]}^{8+}$, $(PZDO)_2\subset\mathbf{[3]}^{8+}$ and $(PZDO)_3\subset\mathbf{[3]}^{8+}$ (hydrogen atoms are not shown for clarity) following path III.

In the case of path I, the energy difference trend $\Delta E_3<\Delta E_4>\Delta E_5$ indicate that the second binding event is less favourable than first and the third binding event is more favourable than second. Conversely, in path II, the energy difference trend $\Delta E_3\approx\Delta E_6<\Delta E_7$ suggests that the third binding event is significantly less favourable. In the case of path III, the energy differences are of similar magnitudes, $\Delta E_8<\Delta E_9>\Delta E_{10}$ with only a small energy difference among them.

S6.4 Energy calculation for the formation of $(PZDO)_4\subset[4]^{10+}$

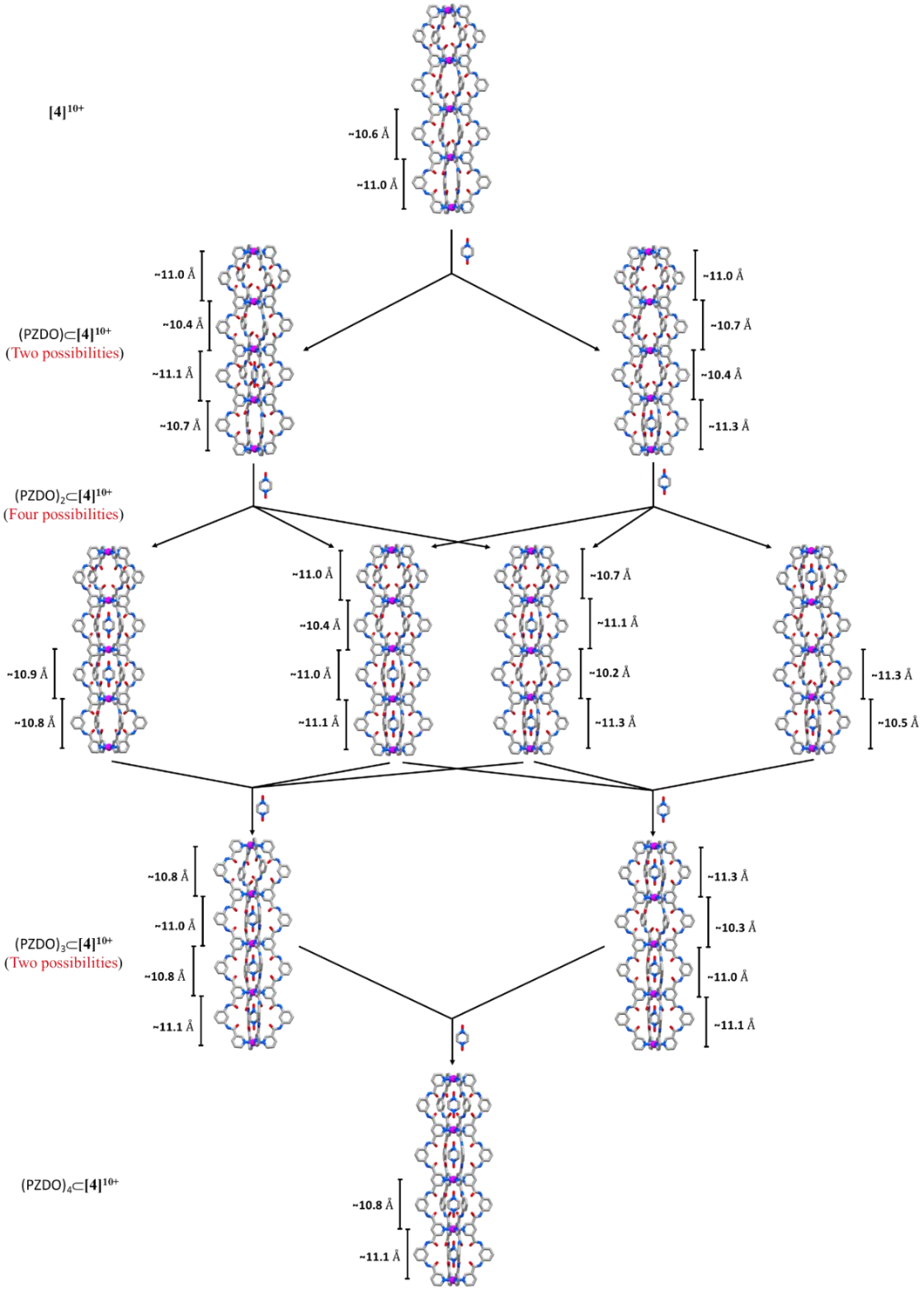

Figure S57. Energy optimized structure in gas phase for $[Pd_5(\mathbf{L4})_4]^{10+}$,$\mathbf{[4]^{10+}}$ and subsequent guest addition products $(PZDO)\subset\mathbf{[4]^{10+}}$, $(PZDO)_2\subset\mathbf{[4]^{10+}}$, $(PZDO)_3\subset\mathbf{[4]^{10+}}$, and $(PZDO)_4\subset\mathbf{[4]^{10+}}$.

The formation of $(PZDO)_4\subset$**[4]**$^{10+}$ follows ten different paths where the calculated energy (in kJ/mol) of PZDO, **[4]**$^{10+}$, host-guest complexes $(PZDO)_1\subset$**[4]**$^{10+}$**,** $(PZDO)_2\subset$**[4]**$^{10+}$, $(PZDO)_3\subset$**[4]**$^{10+}$ and $(PZDO)_4\subset$**[4]**$^{10+}$ are shown below

Path IV

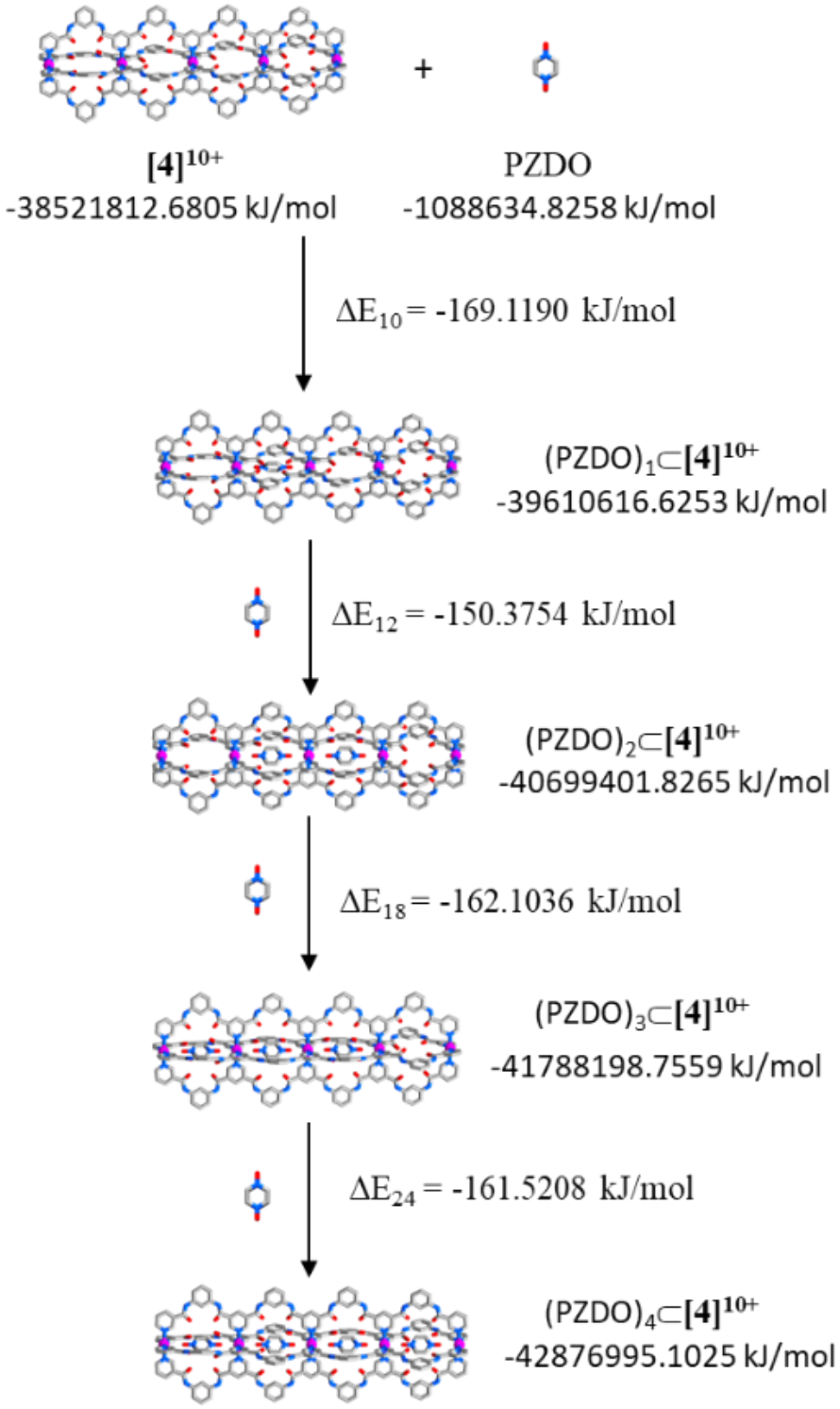

Path V

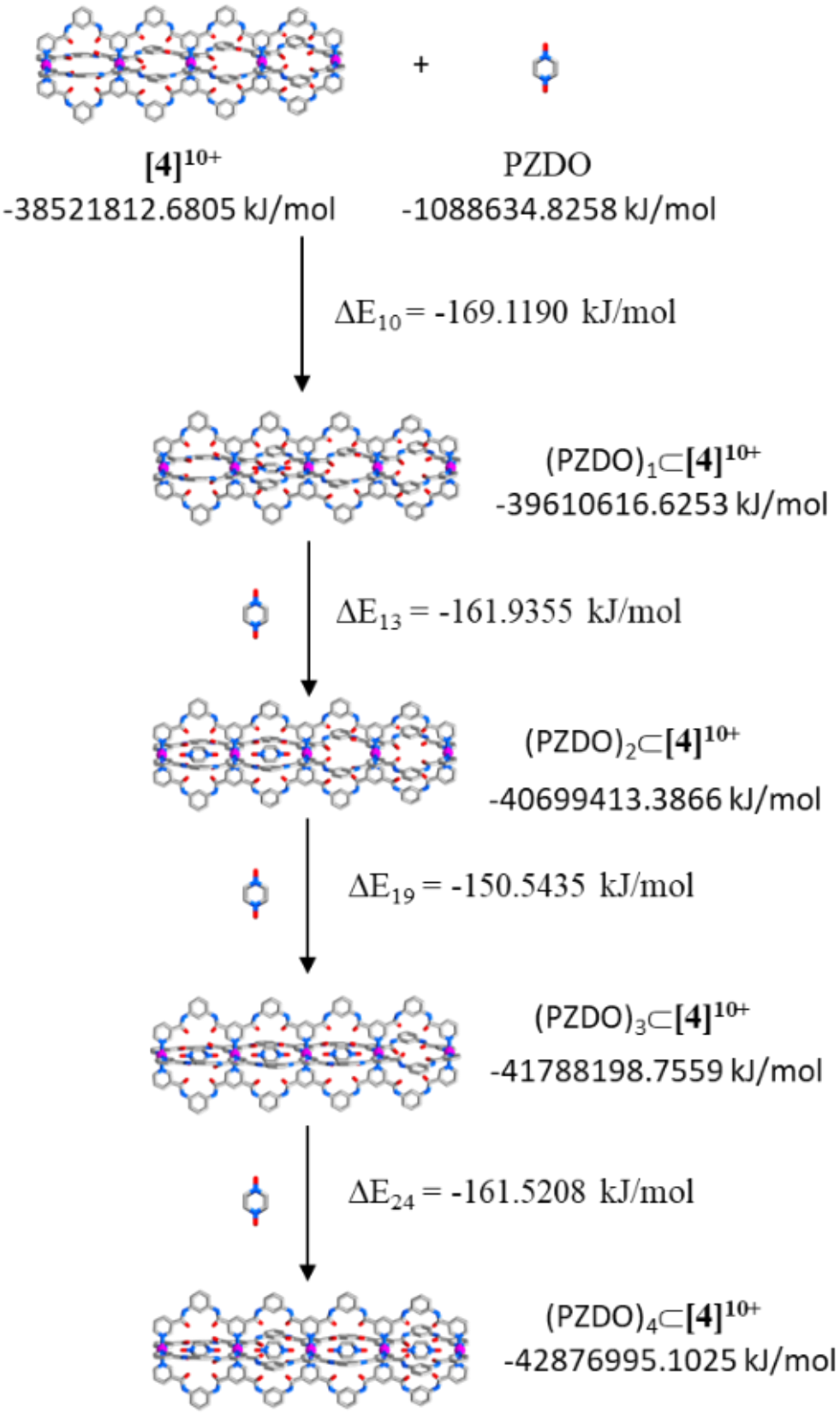
+
[4]10+
-38521812.6805 kJ/mol
PZDO
-1088634.8258 kJ/mol
ΔE10 = -169.1190 kJ/mol
(PZDO)1⊂[4]10+
-39610616.6253 kJ/mol
ΔE13 = -161.9355 kJ/mol
(PZDO)2⊂[4]10+
-40699413.3866 kJ/mol
ΔE19 = -150.5435 kJ/mol
(PZDO)3⊂[4]10+
-41788198.7559 kJ/mol
ΔE24 = -161.5208 kJ/mol
(PZDO)4⊂[4]10+
-42876995.1025 kJ/mol

Path VI

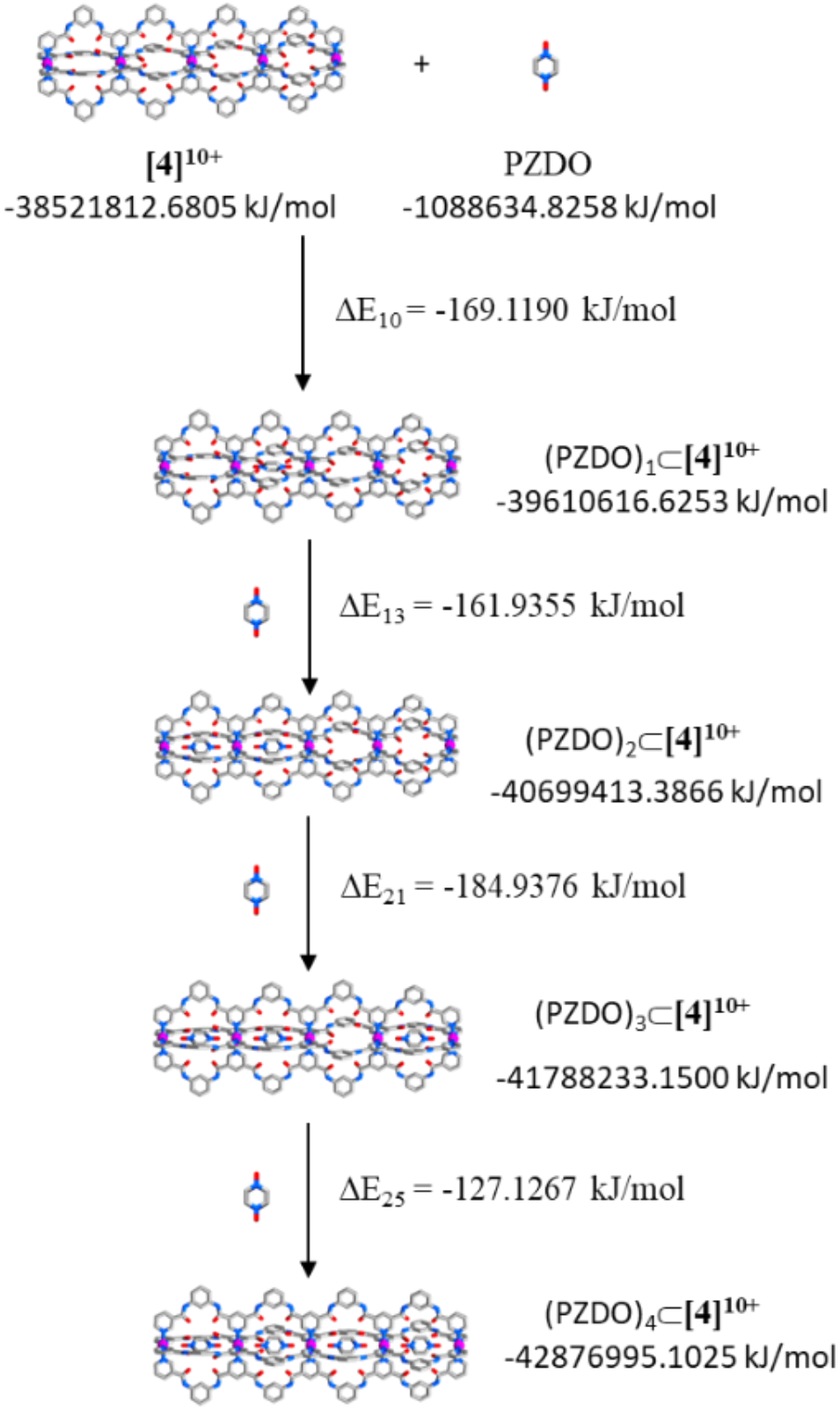
+
[4]10+
-38521812.6805 kJ/mol
PZDO
-1088634.8258 kJ/mol
ΔE10 = -169.1190 kJ/mol
(PZDO)1⊂[4]10+
-39610616.6253 kJ/mol
ΔE13 = -161.9355 kJ/mol
(PZDO)2⊂[4]10+
-40699413.3866 kJ/mol
ΔE21 = -184.9376 kJ/mol
(PZDO)3⊂[4]10+
-41788233.1500 kJ/mol
ΔE25 = -127.1267 kJ/mol
(PZDO)4⊂[4]10+
-42876995.1025 kJ/mol

Path VII

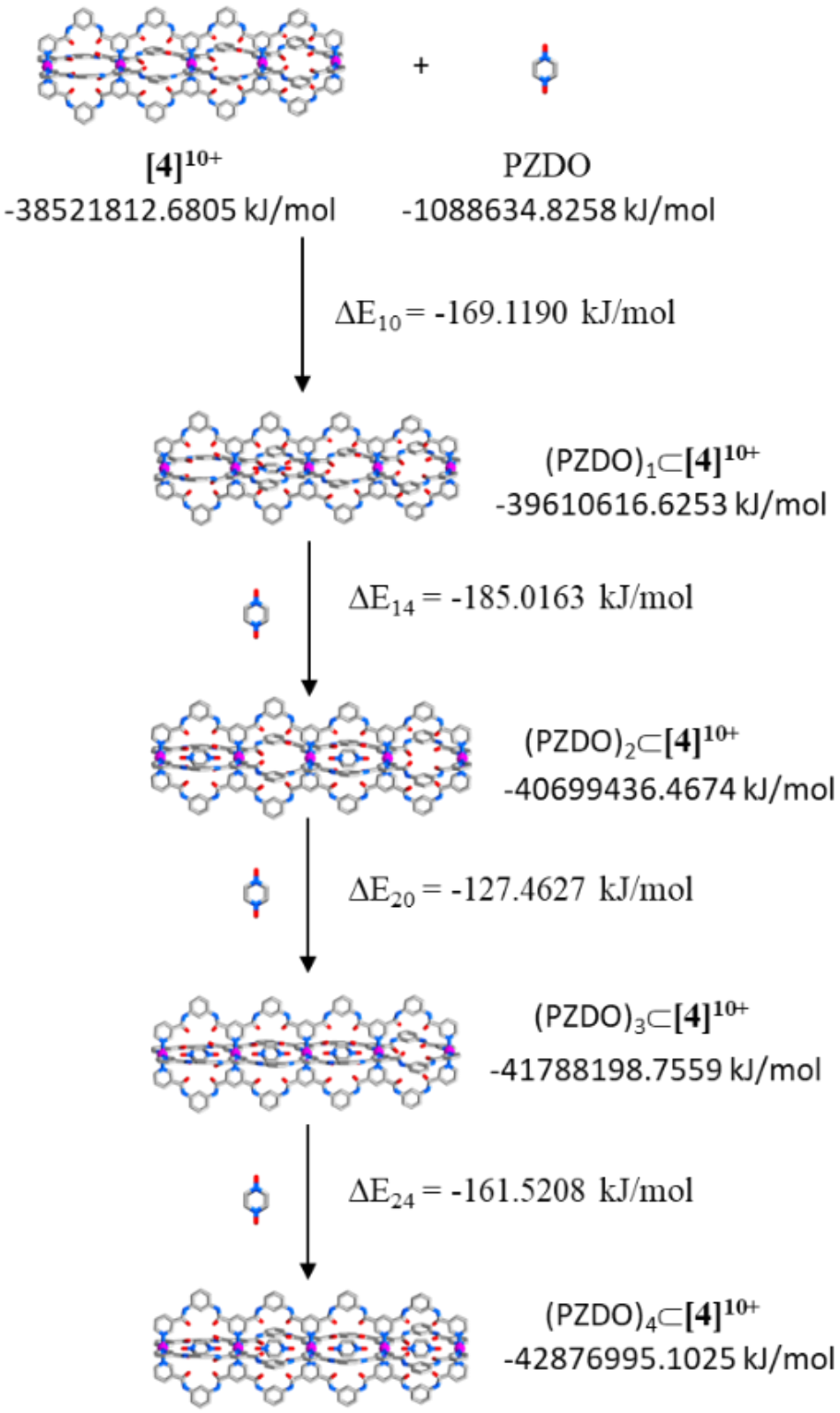
+
[4]10+
-38521812.6805 kJ/mol
PZDO
-1088634.8258 kJ/mol
ΔE10 = -169.1190 kJ/mol
(PZDO)1⊂[4]10+
-39610616.6253 kJ/mol
ΔE14 = -185.0163 kJ/mol
(PZDO)2⊂[4]10+
-40699436.4674 kJ/mol
ΔE20 = -127.4627 kJ/mol
(PZDO)3⊂[4]10+
-41788198.7559 kJ/mol
ΔE24 = -161.5208 kJ/mol
(PZDO)4⊂[4]10+
-42876995.1025 kJ/mol

Path VIII

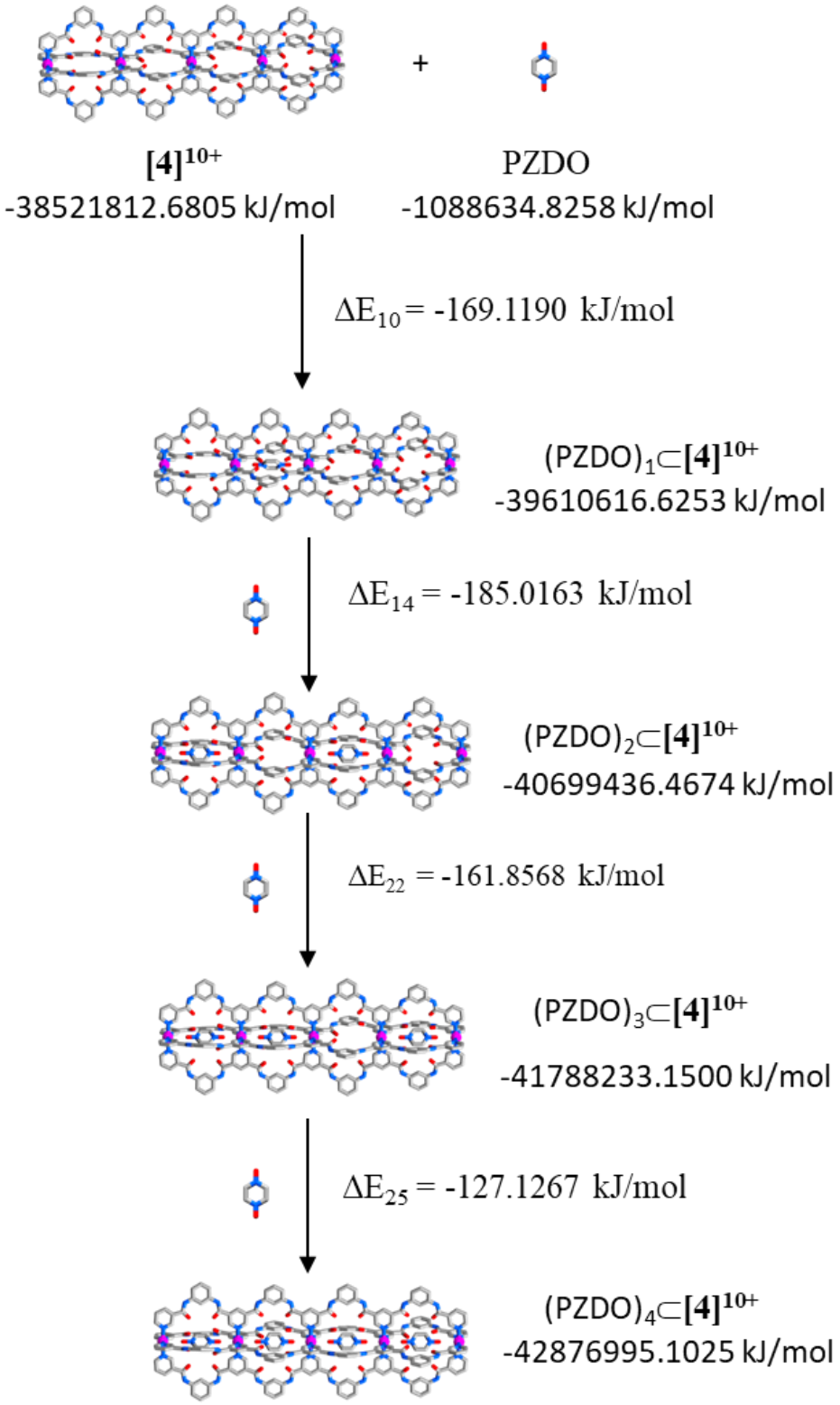
+
[4]10+
-38521812.6805 kJ/mol
PZDO
-1088634.8258 kJ/mol
ΔE10 = -169.1190 kJ/mol
(PZDO)1⊂[4]10+
-39610616.6253 kJ/mol
ΔE14 = -185.0163 kJ/mol
(PZDO)2⊂[4]10+
-40699436.4674 kJ/mol
ΔE22 = -161.8568 kJ/mol
(PZDO)3⊂[4]10+
-41788233.1500 kJ/mol
ΔE25 = -127.1267 kJ/mol
(PZDO)4⊂[4]10+
-42876995.1025 kJ/mol

Path IX

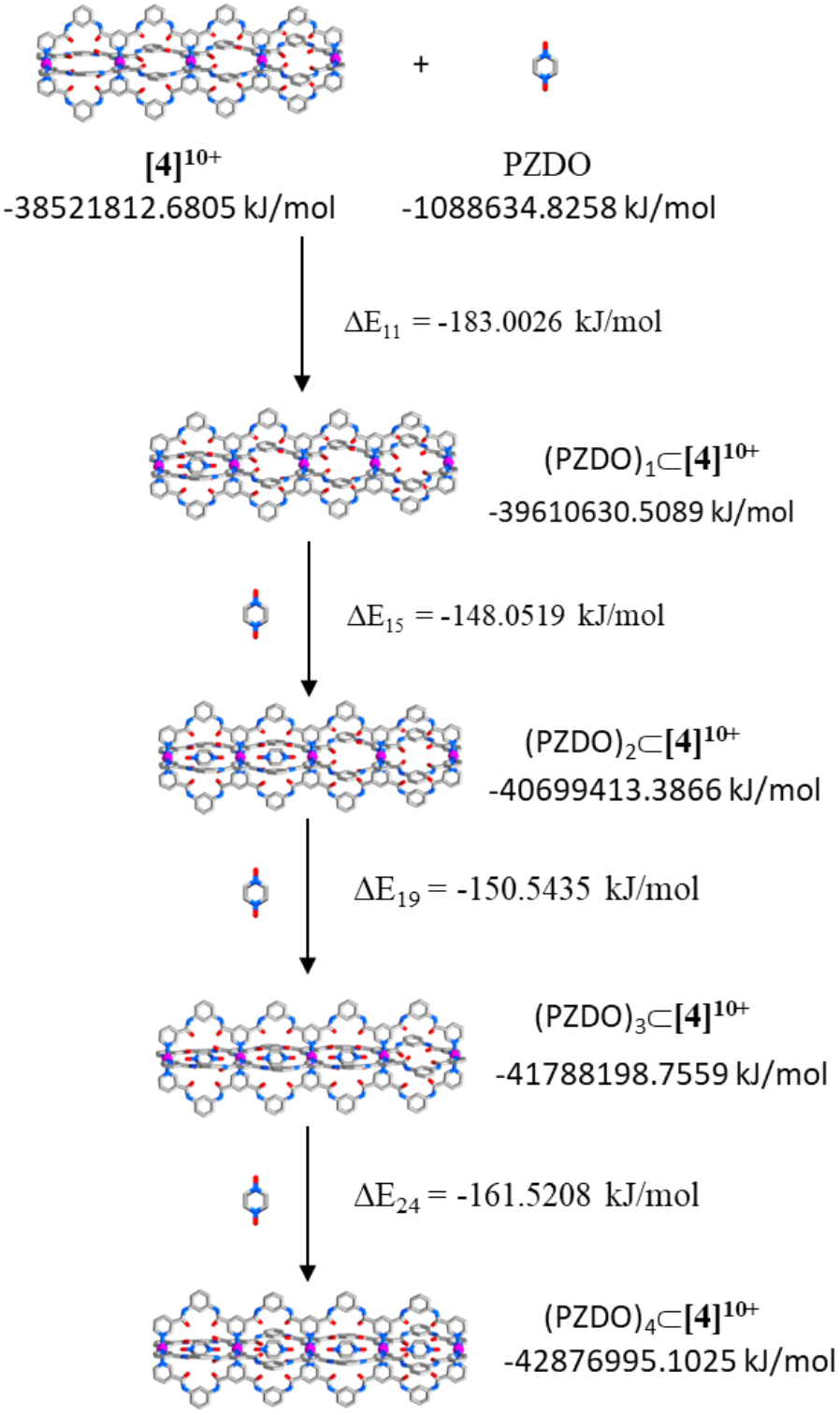
+
[4]10+
-38521812.6805 kJ/mol
PZDO
-1088634.8258 kJ/mol
ΔE11 = -183.0026 kJ/mol
(PZDO)1⊂[4]10+
-39610630.5089 kJ/mol
ΔE15 = -148.0519 kJ/mol
(PZDO)2⊂[4]10+
-40699413.3866 kJ/mol
ΔE19 = -150.5435 kJ/mol
(PZDO)3⊂[4]10+
-41788198.7559 kJ/mol
ΔE24 = -161.5208 kJ/mol
(PZDO)4⊂[4]10+
-42876995.1025 kJ/mol

Path X

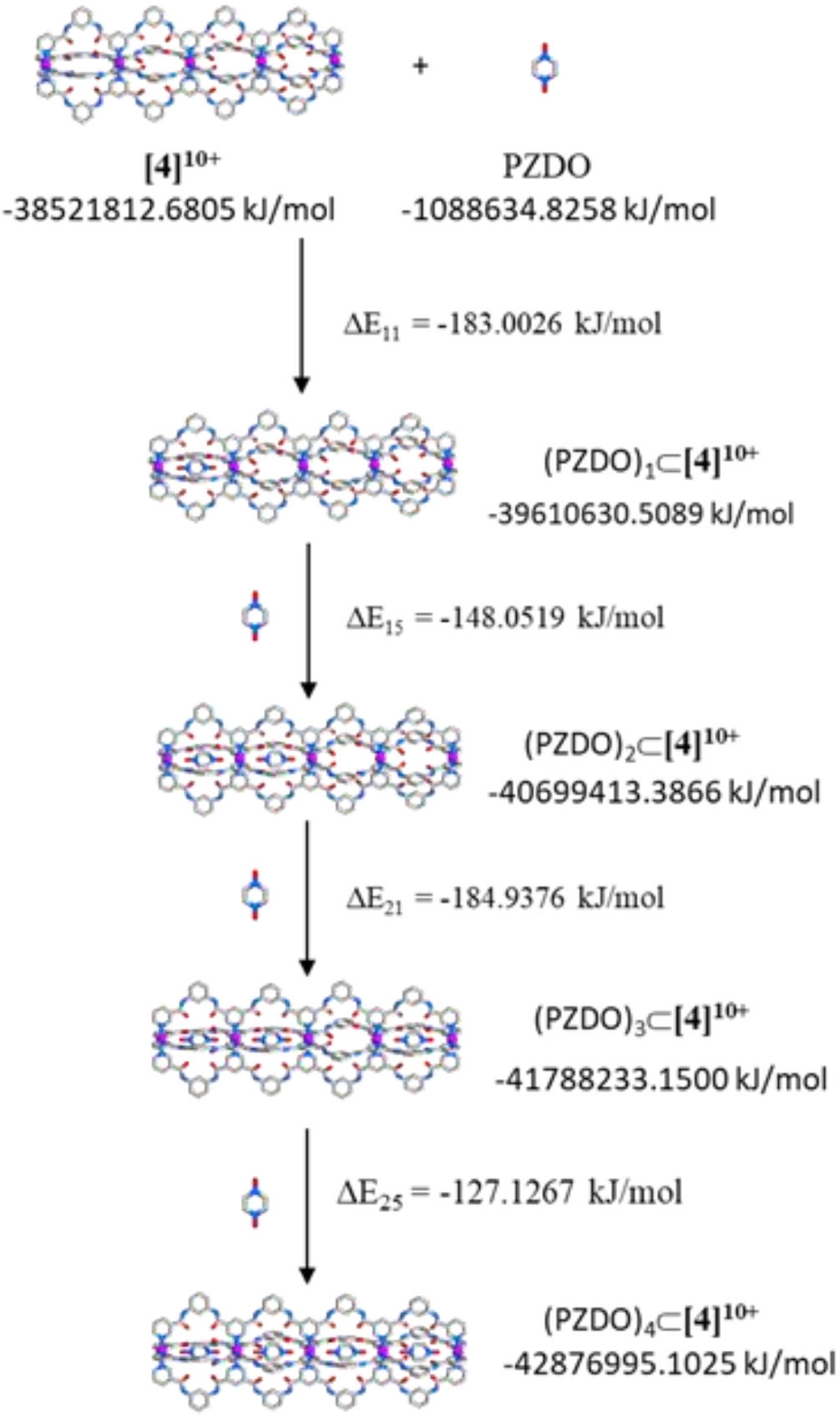
[4]10+
-38521812.6805 kJ/mol
PZDO
-1088634.8258 kJ/mol
ΔE11 = -183.0026 kJ/mol
(PZDO)1⊂[4]10+
-39610630.5089 kJ/mol
ΔE15 = -148.0519 kJ/mol
(PZDO)2⊂[4]10+
-40699413.3866 kJ/mol
ΔE21 = -184.9376 kJ/mol
(PZDO)3⊂[4]10+
-41788233.1500 kJ/mol
ΔE25 = -127.1267 kJ/mol
(PZDO)4⊂[4]10+
-42876995.1025 kJ/mol

Path XI

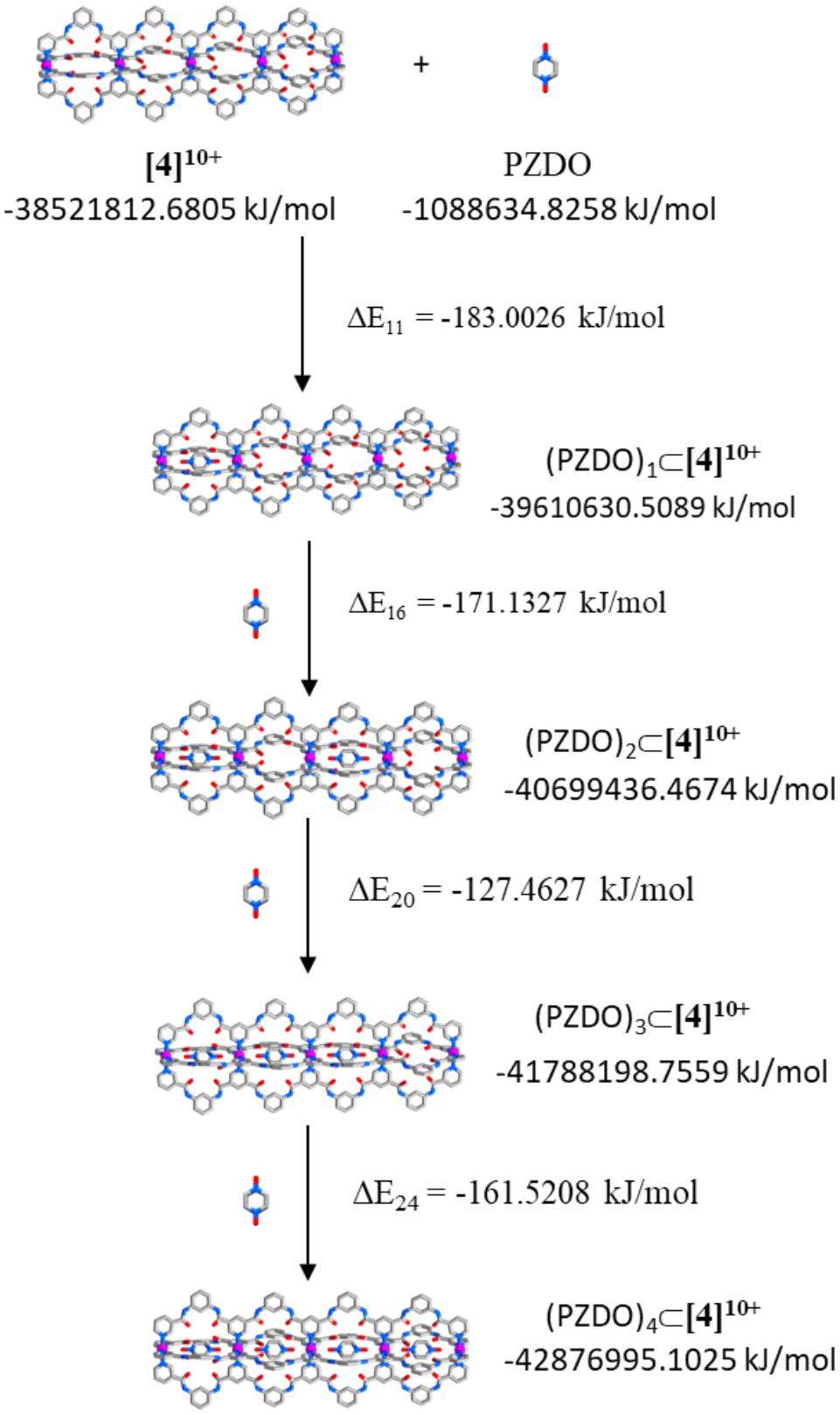
+
[4]10+
-38521812.6805 kJ/mol
PZDO
-1088634.8258 kJ/mol
ΔE11 = -183.0026 kJ/mol
(PZDO)1⊂[4]10+
-39610630.5089 kJ/mol
ΔE16 = -171.1327 kJ/mol
(PZDO)2⊂[4]10+
-40699436.4674 kJ/mol
ΔE20 = -127.4627 kJ/mol
(PZDO)3⊂[4]10+
-41788198.7559 kJ/mol
ΔE24 = -161.5208 kJ/mol
(PZDO)4⊂[4]10+
-42876995.1025 kJ/mol

Path XII

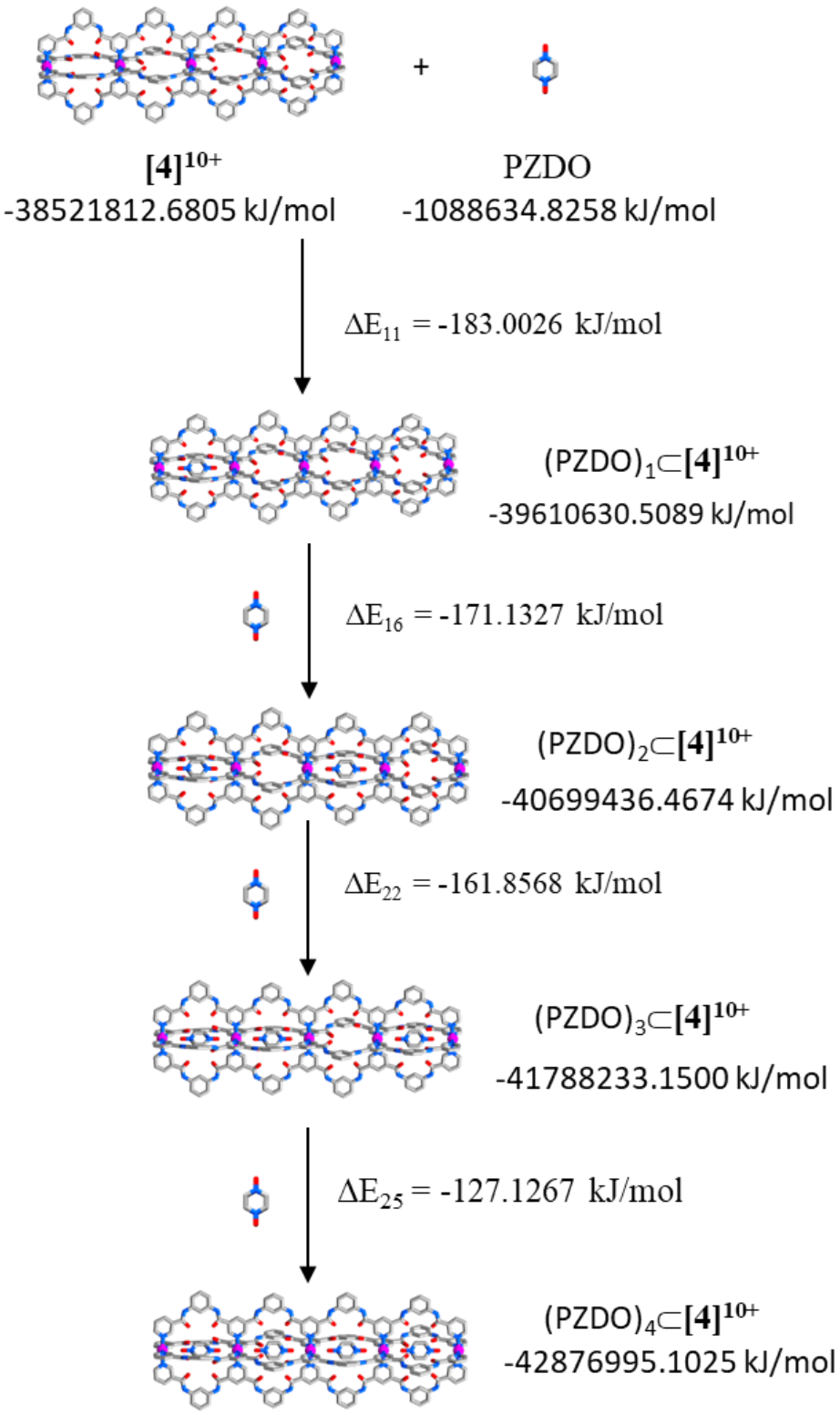
+
[4]10+
-38521812.6805 kJ/mol
PZDO
-1088634.8258 kJ/mol
ΔE11 = -183.0026 kJ/mol
(PZDO)1⊂[4]10+
-39610630.5089 kJ/mol
ΔE16 = -171.1327 kJ/mol
(PZDO)2⊂[4]10+
-40699436.4674 kJ/mol
ΔE22 = -161.8568 kJ/mol
(PZDO)3⊂[4]10+
-41788233.1500 kJ/mol
ΔE25 = -127.1267 kJ/mol
(PZDO)4⊂[4]10+
-42876995.1025 kJ/mol

Path XIII

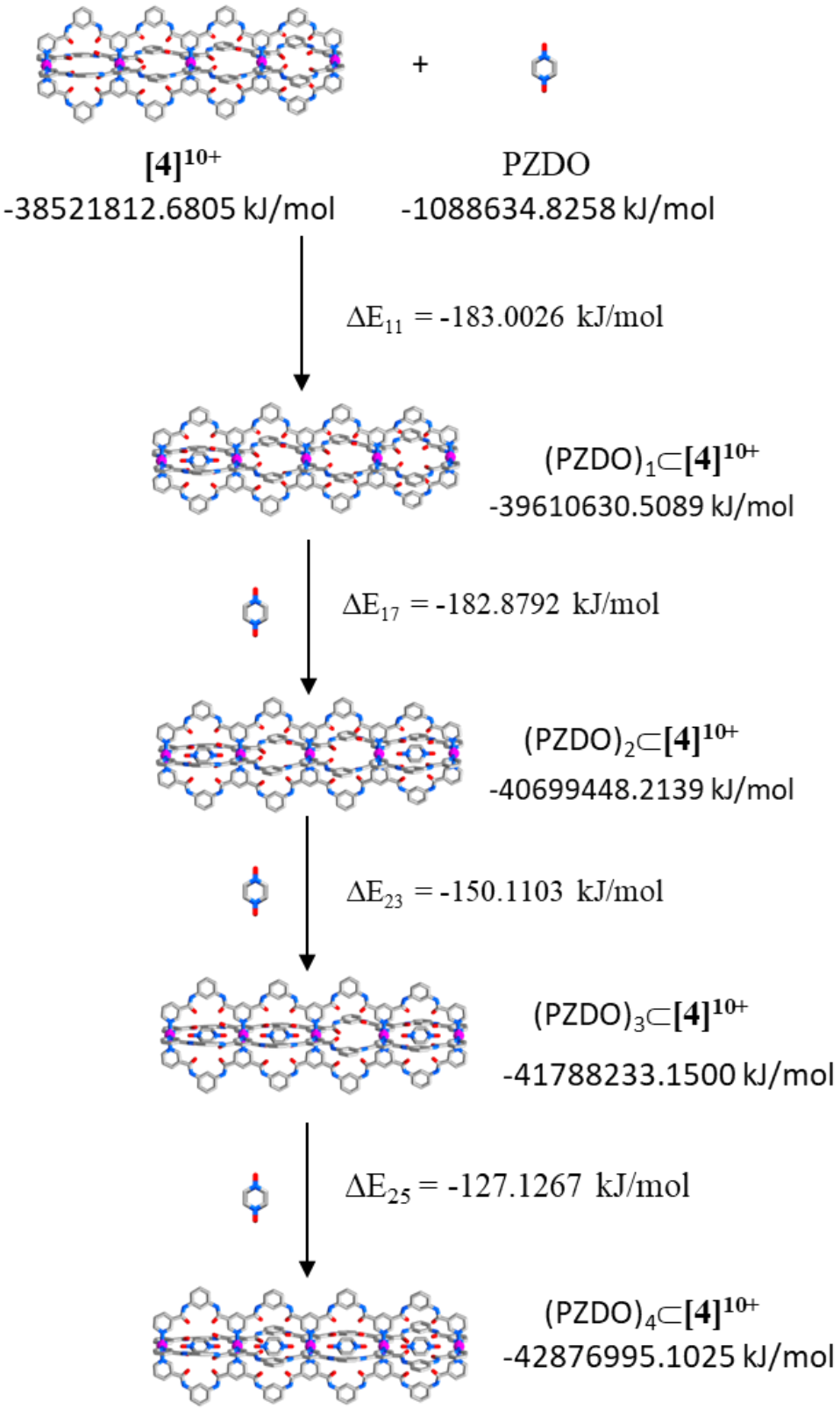

Figure S58. Energy optimized structure in gas phase showing all ten possible paths(paths III to path XIII) for the formation of (PZDO)$_4$⊂**[4]**$^{10+}$ from [Pd$_5$(**L4**)$_4$]$^{10+}$,**[4]**$^{10+}$.

Table S2. Calculated energy difference trends in the formation of cage $(PZDO)_3\subset$**[3]**$^{8+}$ following three distinct paths.

Paths	Energy difference trend
I	$\Delta E_3 < \Delta E_4 > \Delta E_5$
II	$\Delta E_3 \approx \Delta E_6 < \Delta E_7$
III	$\Delta E_8 < \Delta E_9 > \Delta E_5$

Table S3. Calculated energy difference trends in the formation of cage $(PZDO)_4\subset$**[4]**$^{10+}$ following ten distinct paths.

Paths	Energy difference trend
IV	$\Delta E_{10} < \Delta E_{12} > \Delta E_{18} \approx \Delta E_{24}$
V	$\Delta E_{10} < \Delta E_{13} < \Delta E_{19} > \Delta E_{24}$
VI	$\Delta E_{10} < \Delta E_{13} > \Delta E_{21} \ll \Delta E_{25}$
VII	$\Delta E_{10} > \Delta E_{14} \ll \Delta E_{20} \gg \Delta E_{24}$
VIII	$\Delta E_{10} > \Delta E_{14} < \Delta E_{22} \gg \Delta E_{25}$
IX	$\Delta E_{11} < \Delta E_{15} \approx \Delta E_{19} > \Delta E_{24}$
X	$\Delta E_{11} < \Delta E_{15} > \Delta E_{21} \ll \Delta E_{25}$
XI	$\Delta E_{11} < \Delta E_{16} \ll \Delta E_{20} \gg \Delta E_{24}$
XII	$\Delta E_{11} < \Delta E_{16} < \Delta E_{22} \gg \Delta E_{25}$
XIII	$\Delta E_{11} \approx \Delta E_{17} < \Delta E_{23} < \Delta E_{25}$

From Table S3, it is clear that all possible pathways for the formation of $(PZDO)_4\subset$**[4]**$^{10+}$, involve both energetically more and less favourable steps. However, only in the case of path X, there is a consistent incline in ΔE values, indicating that the subsequent addition of guest molecules becomes less favourable. In contrast, none of the other nine paths exhibit a gradual trend of increase or decrease, which suggests a lack of cooperativity.

According to DFT-calculated energy difference trends for both empty cages and host-guest cages of MCDCCs, the complex **[2]**$^{6+}$ shows a gradual increase in energy difference values ($\Delta E_1 < \Delta E_2$). This trend results in decreasing energy gaps, making the formation of a fully guest-encapsulated cage less favourable. In contrast, the cages **[3]**$^{8+}$ and **[4]**$^{10+}$ contain multiple pathways that include both energetically more and less favourable steps. This indicates that the cavities do not interact cooperatively for guest encapsulation. As a result, calculating energy differences in a stepwise manner didn't allow us to conclude whether the MCDCCs **[3]**$^{8+}$ and **[4]**$^{10+}$ exhibit positive or negative cooperativity.

Since the stepwise energy difference calculations were not yielding conclusive results regarding the cage's behaviour, we decided to calculate the average energy difference when a single guest molecule occupies one of the cavities, compared to the energy when all the cavities are filled.

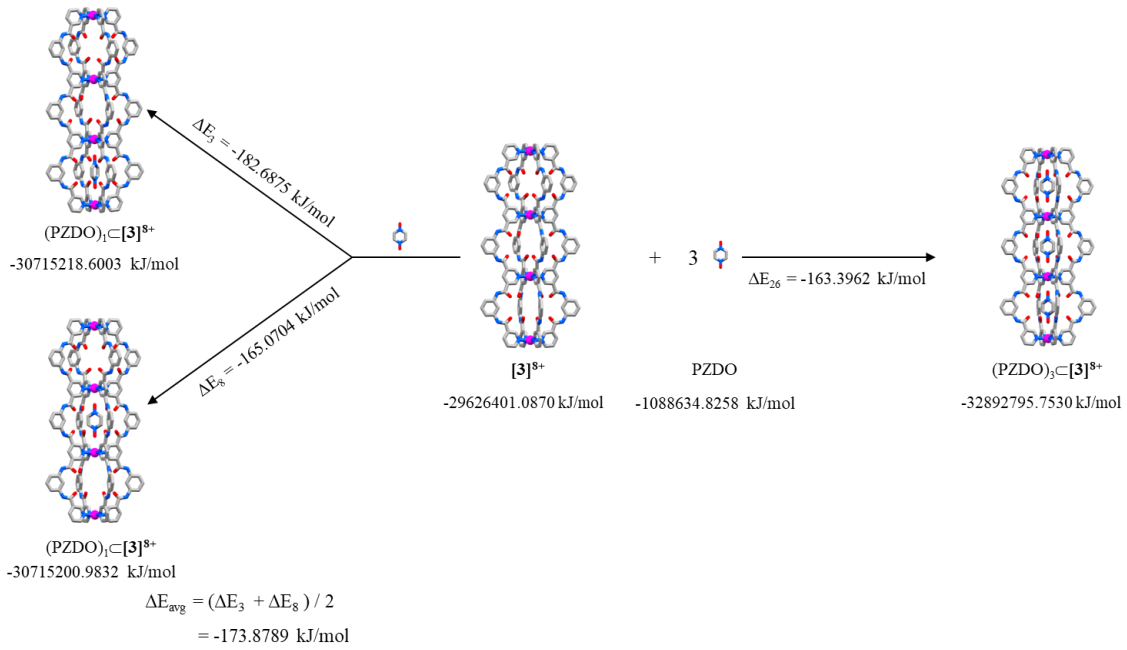

Figure S59. Calculated stabilization energy (in kJ/mol) of PZDO, **[3]**$^{8+}$, host-guest complexes $(PZDO)_1 \subset$**[3]**$^{8+}$ with their average energy difference and $(PZDO)_3 \subset$**[3]**$^{8+}$.

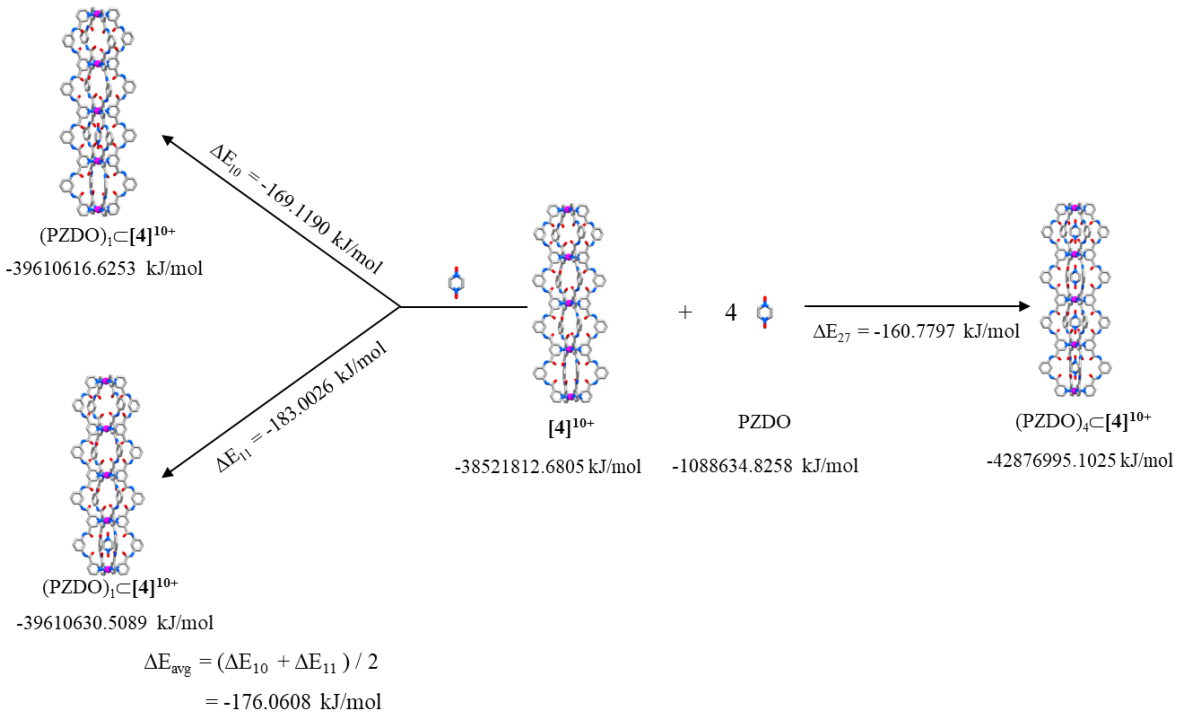

Figure S60. Calculated stabilization energy (in kJ/mol) of PZDO, **[4]**$^{10+}$, host-guest complexes (PZDO)$_1$⊂**[4]**$^{10+}$ with their average energy difference and (PZDO)$_4$⊂**[4]**$^{10+}$.

From the response Fig. S60 and S61, it can be seen that in both the cases ΔE_{avg} is more than ΔE of the fully encapsulated cages. It indicates when one of the cavities encapsulates one guest molecule, the average energy difference is higher than that of the fully encapsulated host-guest cage. Thus, the cases where all the cavities are occupied with guest molecules are less favourable.

Table S4. Calculated average stabilization energy difference in the MCDCCs **[2]**$^{6+}$- **[4]**$^{10+}$.

Cages	Average stabilization energy for guest encapsulation in one of the cavities (E_{avg1})	Average stabilization energy for guest encapsulation in all of the cavities (E_{avg2})	Difference between averaged energy (E_{avg2}- E_{avg1})	Guest binding cooperativity
Double-cavity cage, **[2]**$^{6+}$	-178.8726 kJ/mol	-155.5583 kJ/mol	23 kJ/mol	Negative
Triple-cavity cage, **[3]**$^{8+}$	-173.8789 kJ/mol	-163.3962 kJ/mol	10 kJ/mol	Negative
Quadruple-cavity cage, **[4]**$^{10+}$	-176.0608 kJ/mol	-160.7797 kJ/mol	16 kJ/mol	Negative

In stepwise energy difference calculations of MCDCCs, we observed that many of the steps involved indicate less favourable product formation (Table S1). However, this data does not provide a definite conclusion regarding the cage's cooperative behaviour. In contrast average energy calculation, revealed probable evidences of negative cooperativity (Table S4). Hence, taking the computational study into account we are proposing negative cooperative behaviour of the MCDCCs **[2]$^{6+}$- [4]$^{10+}$** for guest encapsulation.

S7. Single crystal X-ray diffraction

Single-crystal X-ray measurements were recorded for the crystal of $(PZDO)_2\subset$**2·6BF$_4$** on a Bruker D8 VENTURE dual source diffractometer with a PHOTON II detector using Mo-Kα radiation. A single crystal was mounted using a fiber loop and optically centered. The automatic cell determination routine was employed to collect reflections (at different orientations of the detector) and the APEX4 suite[5] was used for determining the unit cell parameters and data integration. Semiempirical absorption correction (multi-scan) based on symmetry-equivalent reflections was applied using the SADABS program.[6] The structures were solved by intrinsic phasing and refined by full matrix least-squares, based on F^2 using SHELXT[7] and SHELXL-2019[8] in the program WinGX.[9] Molecular and packing diagrams were generated using Mercury.[10] Geometrical calculations were performed using PLATON.[11] ORTEPs were prepared using ORTEP-3.[9] The crystallographic data are summarized in Table S4.

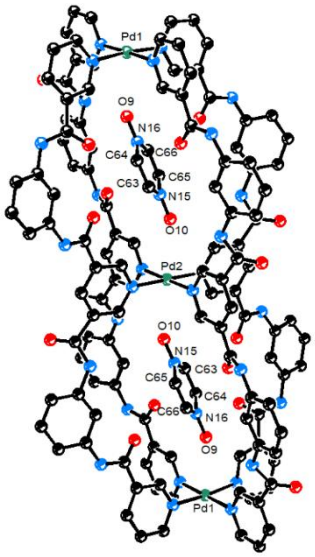

Figure S61. ORTEP of the molecule in crystals of $(PZDO)_2\subset$**2·6BF$_4$**. Thermal ellipsoids are drawn at 50% probability and solvent molecules and anions present outside the cavity of the Pd_3L_4 cage and hydrogen atoms have been omitted for clarity.

Table S5. Summary of crystallographic data for crystal of **(**PZDO)$_2$⊂**2·6BF$_4$**.

	(PZDO)$_2$⊂**2·6BF$_4$**
Chemical Formula	$C_{168}H_{200}B_6F_{24}N_{32}O_{38}$ Pd_3S_{14}
Formula weight	4564.49
Temp. (K)	220(2)
Crystal system	Monoclinic
Space group	$P2_1/c$
Crystal size (mm)	0.150 × 0.130 × 0.100
a (Å)	16.149(3)
b (Å)	26.246(5)
c (Å)	30.520(6)
α (°)	90
β (°)	93.016(7)
γ (°)	90
V (Å^3)	12918(4)
Z D_{calc} (g cm^{-3})	2 1.173
μ(mm^{-1}) *F(000)*	0.398 4688
T_{min} T_{max}	0.6677 0.7457
h, k, l (min,max)	(-21,21), (-35,34), (-40,40)
Reflns collected	583151
Unique reflns	32619
Observed reflns R_{int}	21058 0.1596
No. of parameters	1285
GoF	1.047
$R_1[I > 2\sigma(I)]$	0.0943
$WR_2[I > 2\sigma(I)]$	0.2517
R_1_all data	0.1400
Wr_2_all data	0.2909
$\Delta\rho_{max}$, $\Delta\rho_{min}$ (e Å^{-3})	2.08, -1.15
CCDC No.	2422961

X-ray diffraction-quality single crystals of **(**PZDO)$_2$⊂**2·6BF$_4$** were obtained by the slow diffusion of 1,4-dioxane vapor into a solution of the cage and oligomeric product (containing PZDO) in DMSO. The asymmetric unit in crystals of (PZDO)$_2$⊂**2·6BF$_4$** (monoclinic, $P2_1/c$) contains a half molecule of the trinuclear palladium(II) complex, three BF4− anions, seven

DMSO molecules and a dioxane molecule along with a molecule of PZDO which is present in the cavity of the cage. The electron density corresponding to other disordered solvent molecules was squeezed.[11] Appropriate DFIX instructions were applied during the least-squares refinement to achieve sensible molecular geometry and bond length for the DMSO molecules. RIGU and SIMU restraints were used to maintain reasonable ADPs for the bonded atoms of the anions and solvent molecules. SADI instructions were used for preserving reasonable bond length in portions of the ligand. All hydrogen atoms were placed in geometrically idealized positions (C-H = 0.94 Å for pyridine and aromatic H atoms, C-H = 0.98 Å for methylene H atoms, C-H = 0.97 Å for methyl H atoms and N-H = 0.87 Å for the amide hydrogen atom) and refined isotropically.

Table S6.

Bond length corresponding to various non-covalent interactions inferred from the crystal structures of $(PZDO)_2 \subset \mathbf{2 \cdot 6BF_4}$ (Intermolecular interactions in the complexes)

S.No.	D-H···A	D-H (Å)	H···A (Å)	D···A (Å)	D-H···A / α (°)	Symmetry code
1	C5-H5...O9	0.94	2.56	3.377(6)	145.4	*x,y,z*
2	C27-H27...O9	0.94	2.52	3.360(7)	148.4	*-x+1,-y+1,-z+1*
3	C36-H36...O9	0.94	2.30	3.153(7)	150.1	*x,y,z*
4	C58-H58...O9	0.94	2.42	3.261(7)	148.7	*-x+1,-y+1,-z+1*
5	C64-H64...O5	0.94	2.33	3.179(7)	150.3	*x,y,z*
6	C14-H14...O10	0.94	2.36	3.210(6)	149.7	*x,y,z*
7	C18-H18...O10	0.94	2.58	3.357(6)	140.3	*-x+1,-y+1,-z+1*
8	C45-H45...O10	0.94	2.54	3.363(6)	146.6	*x,y,z*
9	C49-H49...O10	0.94	2.41	3.217(6)	143.3	*-x+1,-y+1,-z+1*
10	Pd1…O9			3.137(4)		*x,y,z*
11	Pd2…O10			3.014(4)		*x,y,z*

S8. Reference

S1. Piepenbrock, M.-O. M.; Clarke, N.; Steed, J. W. Rheology and Silver Nanoparticle Templating in a bis(urea) Silver Metallogel. *Soft Matter*. **2011**, *7*, 2412– 2418.

S2. Li, J. J.; Hamann, L. G.; Dayton, Z. R; Cooper, C. B.; Wu, S. C.; Simpkins, L. M.; Wang, H.; Nayeem, A.; Krystek, S. R. Inhibitors Of 11β Hydroxysteroid Dehydrogenase Type I. US 2006/0235028 Al, October 19, **2006**.

S3. Dennington, R.; Keith, T. A.; Millam, J. M. GaussView 6.0.16, Semichem Inc., Shawnee Mission KS USA, 2016.

S4. Frisch, M. J.; Trucks, G. W.; Schlegel, H. B.; G. E. Scuseria,; Robb, M. A.; Cheeseman, J. R.; Scalmani, G.; Barone, V.; Petersson, G. A.; Nakatsuji, H.; Li, X.; Caricato, M.; Marenich, A. V.; Bloino, J.; Janesko, B. G.; Gomperts, R.; Mennucci, B.; Hratchian, H. P.; Ortiz, J. V.; Izmaylov, A. F.; Sonnenberg, J. L.; Williams-Young, D.; Ding, F.; Lipparini, F.; Egidi, F.; Goings, J.; Peng, B.; Petrone, A.; Henderson, T.; Ranasinghe, D.; Zakrzewski, V. G.; Gao, J.; Rega, N.; Zheng, G.; Liang, W.; M, Hada.; M Ehara,.; Toyota, K.; R, Fukuda.; Hasegawa, J.; Ishida, M.; Nakajima, T.; Honda, Y.; Kitao, O.; Nakai, H.; Vreven, T.; Throssell, K.; Montgomery, J. A.; Peralta, J. E.; Ogliaro, F.; Bearpark, M. J.; Heyd, J. J.; Brothers, E.; Kudin, K. N.; Staroverov, V. N.; Keith, T. A.; Kobayashi, R.; Normand, J.; Raghavachari, K.; Rendell, A. P.; Burant, J. C.; Iyengar, S. S.; Tomasi, J.; M. Cossi,; Millam, J. M.; Klene, M.; Adamo, C.; Cammi, R.; Ochterski, J. W.; Martin, R. L.; Morokuma, K.; Farkas, O.; Foresman, J. B.; Fox, D. J. Gaussian 16, Revision A.03, Gaussian, Inc, Wallingford CT, 2016.

S5. Bruker (2021) Apex4 suite – APEX4, SAINT and SADABS. Bruker AXS Inc., Madison, Wisconsin, USA.

S6. Krause, L.; Herbst-Irmer, R.; Sheldrick G.M.; Stalke D. Comparison of silver and molybdenum microfocus X-ray sources for single-crystal structure determination. *J. Appl. Cryst*. **2015**, *48*, 3-10.

S7. Sheldrick, G. M. SHELXT - Integrated Space-Group and Crystal-Structure Determination. *Acta Crystallogr., Sect. A* **2015**, *71*, 3-8.

S8. Sheldrick, G. M. Crystal Structure Refinement with SHELXL. *Acta Crystallogr., Sect. C* **2015**, *C71*, 3−8.

S9. Farrugia, L. J. WinGX and ORTEP for Windows: An Update. *J. Appl. Crystallogr.* **2012**, *45*, 849−854.

S10. Macrae, C. F.; Sovago, I.; Cottrell, S. J.; Galek, P. T. A.; McCabe, P.; Pidcock, E.; Platings, M.; Shields, G. P.; Stevens, J. S.; Towler M.; Wood, P. A. *J. Appl. Cryst.*, **2020**, *53*, 226-235.

S11. Spek, A. L. Structure Validation in Chemical Crystallography. *Acta Crystallogr., Sect. D* **2009**, *65*, 148−155.